City Research Online

City St George's, University of London

Citation: Scott, J. C. (1978). Pulse length dependence of optical damage in ADP and KD P. (Unpublished Doctoral thesis, The City University, London)

PULSE LENGTH DEPENDENCE
OF
OPTICAL DAMAGE
IN
ADP AND KD^*P

J. C. SCOTT

THESIS PRESENTED FOR THE DEGREE OF
DOCTOR OF PHILOSOPHY
IN
ELECTRICAL ENGINEERING
AT THE CITY UNIVERSITY

FEBRUARY 1978

Abstract

This thesis is concerned with the development of an ultra-fast pockels cell and electrical switch which are used to generate short optical pulses. These picosecond pulses are then used to investigate the pulse length dependence of inclusion damage in amonium dihydrogen phosphate (ADP) and potassium dideutrium phosphate (KD*P).

An electrical switch in the form of a laser triggered spark gap (LTSG) has been developed which generates two identical voltage steps of 180ps risetime into two separate 50ohm cables with immeasurable jitter. The optimization of the pressure voltage characteristics of the spark gap has been achieved to give the minimum possible risetime.

An ultra-fast pockels cell with 74ps electrical risetime has been developed which when used in conjuction with the LTSG produces optical pulses of 250ps half width.

Using pulse lengths ranging from 20ns to 300ps the pulse length dependence of inclusion damage threshold has been found for ADP and KD*P. These tendencies have been used together with the extension of an existing theory to determine the possible composition of inclusions responsible for damage.

A technique of analysis has been developed to determine the volume density of inclusions responsible for damage at a particular pulse length.

CONTENTS

SECTION 1

INTRODUCTION

1.1 General Introduction.

The use of the XDP materials as components in high power optical systems necessitates a complete investigation of their optical breakdown characteristics. Previous workers have measured the absolute power threshold levels for inclusion damage in these materials at pulse lengths of several nanoseconds, the object of this work is to determine the pulse length dependence of the power threshold levels for inclusion damage in ADP and KD*P.

If the power threshold levels of inclusion damage are to be increased so that these materials can be used at higher optical power densities, a knowledge of the composition of inclusions likely to cause damage is necessary. Previous authors have attempted this task by direct observation of the inclusion itself. These investigations have been hindered by the extremly small physical size of the inclusions.

The samples of amonium dihydrogen phosphate(ADP) and potassium dideutrium phosphate(XD*P) were supplied by Electro-Optic Developments Ltd. of Basildon UK. Apart from several specially selected samples they were considered typical of good quality materials used in the manufacture of pockels cells, low voltage light modulators and harmonic generators.

One method of producing variable length laser pulses is to generate a high power pulse of several nanoseconds length by Q-switching, and use an optical switch to gate through a small section of the Q-switched pulse. Using this technique optical pulses with lengths limited only by the risetime of the optical switch can be obtained.

This thesis describes a novel method of controling an ultra-fast pockels cell to generate optical pulses covering a two decade range from an initial 20ns Q-switched pulse.

1.2 Thesis Construction.

The identification of the source of damage in an optical component must be undertaken before a detailed analysis of its charasteristics can be made and linked to a suitable theory.

Section 2 deals with the possible sources of damage in the XDP materials, placing particular emphasis on those identifying characteristics which are easily measured and often visible to the naked eye.

The description of several systems of laser control is given in section 3. The convenience and simplicity of the krytron arrangement is described, and this is compared with the laser triggered spark gap for producing subnanosecond electrical risetimes. Finally an optical amplifier is described which produces optical pulses compatible with the power requirements needed for short pulse length damage.

In section 4 an investigation of the use of strip line technology for the construction of an ultrafast KD*P pockels cell is undertaken. The performance of the final design is compared with that of commercially available pockels cells.

The parameters of the laser and its control system are very important when the measurement of power density is to be carried out. In section 5 criteria by which damage is detected and the experimental technique used to obtain discrete values of damage threshold are described. In this section the pulse to pulse stability of the laser is discussed together with power and pulse length measurement techniques. Finally the accuracy of the figures quoted for the threshold of damage is considered.

In section 6 the experimental results of the power density threshold variations with pulse length are quoted together with results of the analysis revealing the volume density of inclusions responsible for damage. This is followed by an investigation into the composition of the inclusion.

In section 7 the theory of Hopper and Uhlman is extended so that calculations of inclusion temperature can be carried out in the XDP materials. This leads to predicted power threshold variations with pulse length which in section 8 are compared with the previously measured tendencies. These comparisons lead to several conclusions which are given together with conclusions derived from the overall laser system.

The natural follow up to this work is given in section 9 as suggestions for further work.

SECTION

2

DAMAGE MECHANISMS

Introduction.

The problem of determining the type of breakdown in an optical component after it has been subject to exposure by high power radiation must be solved before any attempt at increasing the materials resistance to optical damage can be made.

Many optical materials experience variations in damage threshold for different conditions of exposure. These variations can be due to different damage mechanisms causing damage. The following review presents a survey of published work to date which will illustrate the relative effects of the different types of damage, so that in a practical situation an estimate of the particular form of damage can be made.

Together with these results a review of current theories that have been proposed to explain the different mechanisms will be given, with an attempt to predict, from these theories, the variation of damage threshold with pulse length for the main damage mechanisms.

2.1 Intrinsic Breakdown (Avalanche)

When a light beam is focused with a converging lens and a sample of optical material free from impurities is placed at the lens focus, a distribution of power density ranging from a low value at the entrance surface to a maximum in the bulk and a low value again at the exit face will be produced. If the input power is high enough damage will occur.

The resulting damage can appear in different characteristic forms, one of these is typically a micron sized star shaped crack which can have different characteristics in different materials. This small dislocation always falls at the geometric focus of the lens system which is the region of maximum power density.

Bass and Barret(1972) carried out detailed measurements observing damage of this type. They made sufficient observations to treat the results statistically.

By subjecting the material to a number of pulses of fixed power from a laser emitting energy at 1.06 microns they were able to determine the probability that damage would occur at a given power level.

They applied this technique to ten different materials including potassium dihydrogen phosphate(KDP) and ADP. The common result was that when the natural log of this probability(P) was plotted against the square root of the power density a straight line resulted. This can be written as

$$P(E) \alpha \exp(-K/E) \qquad 2.1$$

where E is the rms value of the optical field and K is a constant. This result is shown graphically in figure 2.1 for ADP and KDP. Bass and Barrett considered surface damage only, as the power density at the surface can be specified accurately.

A bulk study was carried out by Fradin, Yablonovitch and Bass(1973). They defined damage threshold as the value of incident power necessary to produce intrinsic damage in a single shot for 50% of the positions irradiated. Again they considered only the cases where the damage fell at the geometric focus of the lens system, which consisted of a very short focal length lens so that the volume of high power density was very small. This decreases the probability that an inclusion will be present within the high power density region.

Fradin et al made a point of varifying that self focusing was not present, since this is the topic of the next section of this work only a brief summery of the tests carried out will be discussed here. The field strength threshold for damage using three different lenses was measured and found to be independent of the lens focal length. If self focusing had been present the field strength damage threshold would have scaled with the inverse of the lens focal length. The second test revealed that the measured values were well below the theoretical values of the critical power for self focusing.

In confirming that their breakdown was due to avalanche mechanisms Fradin et al considered several factors derived from their results and compared these with existing avalanche breakdown theories.

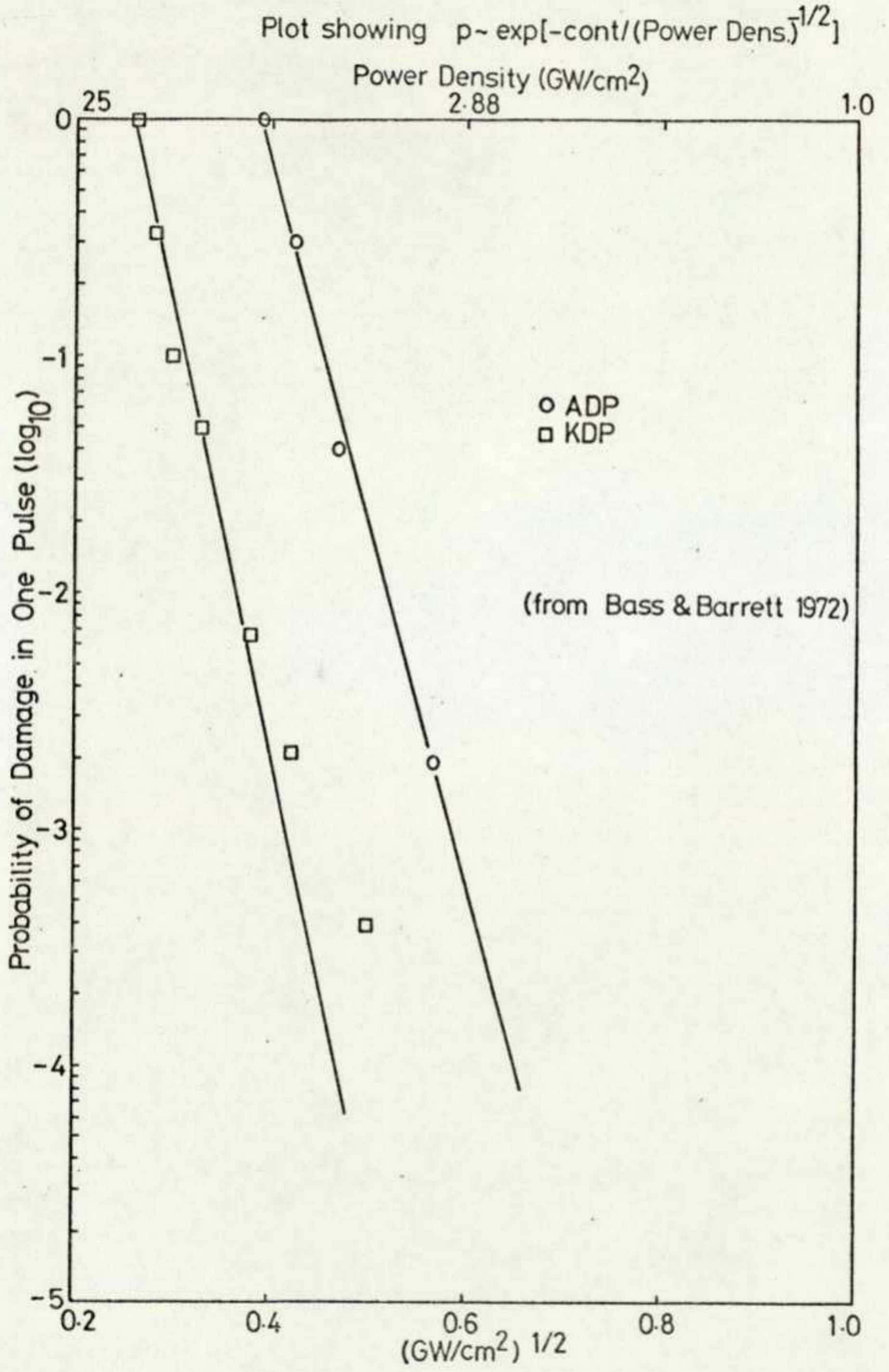

Fig 2·1

2.2 Theories.

Several theories of avalanche breakdown will now be described to show that there is a high probability that the breakdown discussed previously is due to avalanche ionization. The fact that no theory for avalanche ionization has been proposed that fits all the observed data makes it impossible to show conclusively that the damage is due to avalanche ionization.

Previous workers including Wasserman(1967), Zverev(1968) and Hellworth considered so called free electrons in solid materials. If these electrons were actually free they would oscillate 90° out of phase with the applied field producing no net energy absorption. Because of the interaction between the electrons and phonons energy is absorbed producing a dampening effect. Wasserman considered the equilibrium condition that can be obtained as a result of the average energy absorption and dampening. He also predicts a critical energy that the electron will possess so that the average absorption will be greater than the energy loss due to collisions with phonons. Wassermans consideration of the electron-optical phonon interaction predicted breakdown fields an order of magnetude higher than those observed.

A different approach was taken by Shockley(1961) who determined that the average electron taken by Wasserman did not represent the electron which was responsible for initial ionization in a DC field, since this is produced mainly by an electron which was accelerated to its ionization energy without undergoing a single collision. The probability that an electron will travel a distance x without experiencing a collision is

$$(p) = \exp(-x/l) \qquad 2.2$$

where l is the mean free path. For the electron to reach an ionization energy ϵ it must travel a distance

$$x = \epsilon/(eE)$$

where e is the electron charge and E the applied field. This gives the probability that an electron will be ionized (ionization coefficient) as

$$\alpha(E) = \exp(-\epsilon/eE) \qquad 2.3$$

Assuming a mean free path of 100Å (typical for a solid) this equation is in good agreement with experimental results obtained by Chynoweth(1959).

Later Baraff(1962) determined that Shockleys relationship held for field strengths of up to 10^6 V/m. The approach presented by Shockley for DC fields could be used to explain the alternating field case. Instead of an electron travelling a given distance without undergoing a collision, this lucky electron could vibrate in such a manner that it is in phase with the applied field.

Bass and Barret obtained practical results in terms of the probability of damage occuring within a pulse period. To justify the claim that the damage was caused by avalanche ionization they showed that a simple linear relationship could exist between the ionization coefficient $\alpha(E)$ in equation 2.3 and the probability of damage P(E) in equation 2.1. They then examined the regularities between the information given in figure 2.1 and the avalanche breakdown theory.

Fradin et al used experiments with DC fields in alkali-halides to plot ionization coefficient $\alpha(E)$ against electric field. They used this curve to explain qualitativly the time dependent observations made with high frequency optical fields. Again the agreement of the observed breakdown strengths with 1.06 micron radiation and the breakdown strengths with DC electric fields indicate a strong belief that the damage produced by the high frequency field is caused by avalanche ionization.

A recent theory by Sparks(1975) involves new mechanisms for generating starting electrons and for initiating and sustaining an avalanche. The theory is based on a photon-electron phonon reaction process that was considered by Hølstein in 1954 for acoustical phonons in studies of metals. The basis of the Holstein process is that the phonon interaction allows the electron to absorb the entire energy of the photon. The report by Sparks contains only a qualitative account of the theory but gives several graphs to illustrate the accuracy of this theory to some practical results. The graph shown in figure 2.2 gives a comparison of the Holstein theory, Holway Fradin theory and experimental results for pulse width verses breakdown field.

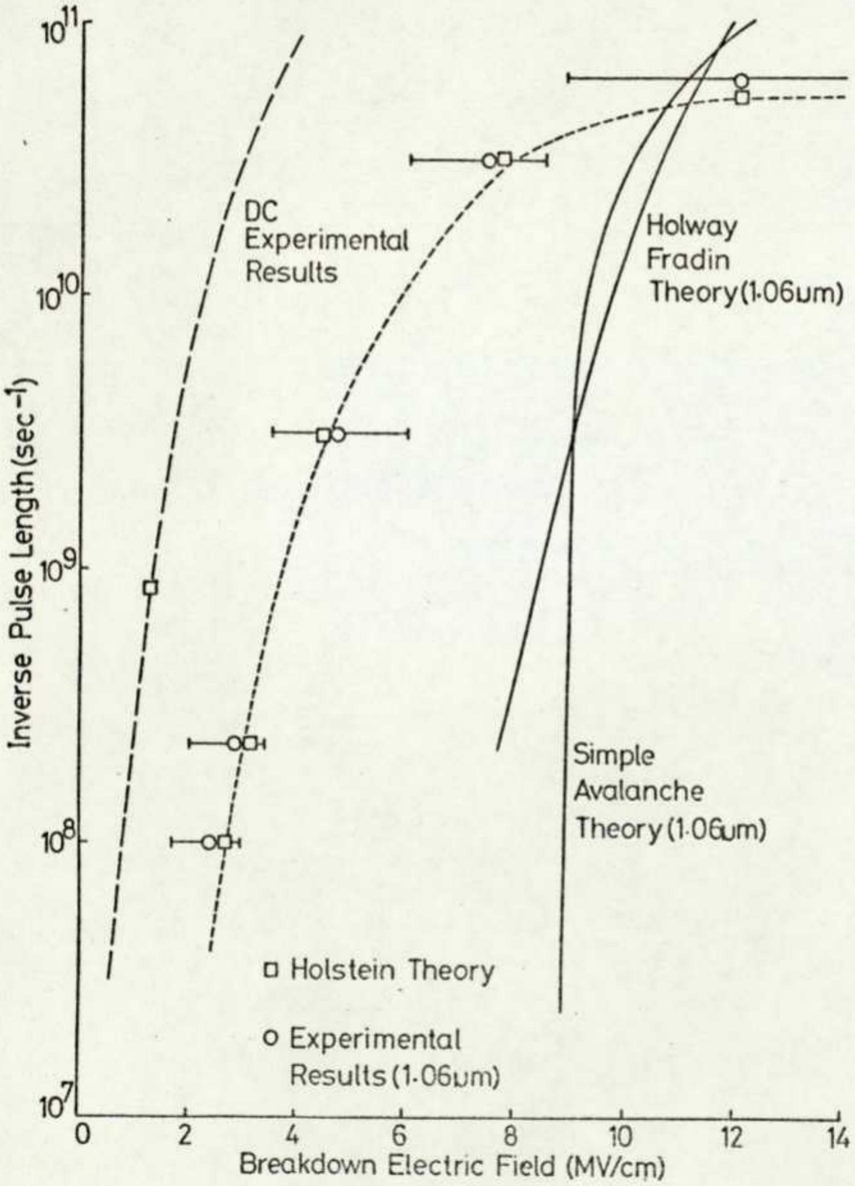

Comparison of Holstein Theory
with Previous Theories and Experimental Results (Sparks)

Fig 2·2

2.3 Identification.

The basic assumption made here is that if the breakdown repeatedly occurs at the geometric focus and the threshold for breakdown is in order of magnetude agreement with the DC avalanche breakdown threshold in the same material, then the breakdown is assumed to be avalanche or intrinsic breakdown.

2.4 Self focusing.

A second form of damage is characterised by a long very thin track of damage, usually ranging from the geometric focus of the imaging system several centimeters towards the lens, and sometimes away from the lens, but always coaxial with the incident beam. The width of the damage track is usually in the order of one or two microns in diameter, a typical example is shown in figure 2.3, inclusion damage is visible, in this photograph, along the self focusing filiment (mag: ×100)

An explanation of this form of damage involves considering the effect of power density on the dielectric constant of the material. Certain materials have the property that when an increase in electric field is experienced a corresponding increase in dielectric constant is produced, this has the effect of increasing the refractive index at the point of exposure. In most materials this effect does not become evident until very high power densities are reached.

The effect of the change in refractive index is to cause the centre section of the beam where the field is greatest, to travel slower than the edge of the beam, this is due to the higher refractive index at the centre. The beam will then undergo continuous focusing which in turn increases the electric field again. This process continues at a very fast rate until the width of the beam is limited by diffraction effects. The natural diffraction will tend to have a greater effect as the beam radius reduces in size. The limiting case is reached when the divergence due to diffraction is equal to the non-linear scattering and avalanche breakdown. The onset of these damage mechanisms is determined by the threshold for self focusing or critical power.

2.5 Non-linear refractive index and critical power.

Self focusing damage was first reported by Hercher(1964), and soon after Chiao et al(1964) derived a value for the critical power needed before self focusing can proceed. They realized that the critical power was achieved when diffraction effects were overcome by focusing effects at a given beam diameter. The refractive index of a non-linear material can be expressed in terms of the applied field

$$n = n_0 + n_2 E^2 + \ldots\ldots \qquad 2.4$$

where E is the applied field. The beam will diverge with an angle of θ where

$$\theta = 1.22\lambda/n_0 D$$

due to diffraction, where D is the diameter of the beam and λ is the radiation wavelength. If the n_2E^2 term of equation 2.4 is so high that it causes the critical angle for total internal reflection to be greater than θ then trapping will occur. The requirement for this is

$$P_C = \frac{\pi D^2}{4}\frac{n_0 E_C}{8\pi} \geqslant \frac{(1.22\lambda)^2 c}{64 n_2} \qquad 2.5$$

if $\theta \ll 1$ (cgs units).

Once the light is trapped in the filament it might travel for several centimeters or approximately 10^{-10} seconds before the filament collapses.

2.6 The mechanism responsible for the coefficient n_2.

There are three potentially important effects which can lead to an introduction of the coefficient n_2 in equation 2.4. These are the Kerr effect, thermal absorption and electrostriction.

The Kerr effect has been studied in detail for many materials, a value of n_2 for ADP has been measured as 3×10^{-23} $m^2 V^{-2}$, Perfilova(1968).

Thermal absorption produces a complex effect as the heating produces several competing mechanisms. In the initial stages a constant volume process occurs which is instantaneous. A second process due to thermal expansion requires time to build up and decay. The sum of these two is usually measured, so it can be seen that there will be a large pulse width dependence of n_2 due to thermal absorption. Thermal heating has been treated in detail by Quelle(1969). Christmas(1973) calculated the value of n_2 for ADP and KD*P as 4.4×10^{-24} and 9.0×10^{-24} $m^2 V^{-2}$ respectively.

Electrostriction is produced by the electrostrictive force on the material which tends to draw the material into the region of high electric field. This causes an acoustic wave to propigate normal to the direction of the radiation, and produces a corresponding change in refractive index. Christmas calculated values of n_2 for electrostriction in ADP and KD*P as 2.4×10^{-22} and 1.6×10^{-22} $m^2 V^{-2}$ respectively.

It is evident from the above that electrostrictive effects produce a value of n_2 larger than the other competing factors. This value also agrees with the value of n_2 obtained by Christmas by measuring the critical power for self focusing and using equation 2.5 to calculate n_2. Kerr(1971) gives a comprehensive account of the role played by electrostriction in self focusing.

2.7 Self focusing identification.

There are several simple tests that can be performed to determine whether damage occuring is due to self focusing. Firstly the damage usually appears as a streamer with the length to diameter ratio very high and appearing coaxial with the incident beam. A quantitative test involves focusing the beam with lenses of different focal lengths and recording the power threshold of damage in each case. Using the spot area and assuming a gaussian beam profile the power density is measured for damage threshold. If this power density threshold is constant for different lens focal lengths then the damage is not due to self focusing, since the critical power could not have been reached. If the critical power had been reached the density for threshold would have varied inversely with the lens focal lengths. This is because the focal point diameter reduces as the focal length is reduced. Hence the diffraction effect becomes greater, resulting in a larger incident power needed to overcome the increased diffraction divergence.

A final consideration that should be made is a comparison of the breakdown threshold as calculated using equation 2.5 and the value obtained experimentally This is very useful as the power density is usually much greater for self focusing threshold than for avalanche or inclusion breakdown using pulse lengths in the nanosecond region.

2.8 Extrinsic breakdown(Inclusion).

The third and most important form of damage from a practical point of view in the XDP materials is that characterised by a random distribution of small star like damage regions both along and in the vicinity of the axis of the beam. The extent of the deviation of the spatial distribution of damage areas is determined by the focusing arrangement. A typical example is shown in figure 2.4 in ADP (mag: 200). The reason for the importance of this damage mechanism is that in the XDP materials studied the lowest damage threshold was usually present in this form, under normal practical irradiating conditions.

The geometry of this damage and the magnitude of its threshold power density suggest that randomly occuring particles could be the cause. This implies that a study of the heat formation caused by the presence of inclusions should be made.

Inclusion Damage in ADP
Fig 2.4

Although this damage is termed inclusion damage it can result from effects other than the presence of discrete inclusions, a discontinuity in the crystal lattice formation or an area of refractive index change can produce similar effects and therefore should be considered as a possible cause of inclusion damage.

An inclusion may absorb a certain amount of energy from the incident radiation and as a result increase in temperature. If this temperature increase is high enough localised damage can result from the very high thermal stresses produced. A second method of damage production can result from the diffraction focusing effect around an inclusion. A region of power density higher than that incident on the inclusion can be produced in a region distant from the inclusion. If the power density is high enough avalanche breakdown or self focusing could occur, but if a second inclusion is in the region it can cause damage by absorption as described above.

Several authors have treated the particle with classical thermodynamics, Hopper and Uhlman(1973) derived expressions for the catastrophic failure of platinum particles in a glass host material. Their solution to the heat conduction equation was only valid for host materials having physical properties which fall into a specific range. They also used the physical size of the inclusion for energy absorption calculations without takeing into account the wavelength dependence of the absorption crossectional area. This will be discussed in detail in section 7.

Hopper and Uhlman found that for very small particles the resulting temperature is low due to the high heat loss to the surrounding glass. For large particles, again the resulting temperature is low because of its thermal mass. Between these two limits is a particle size which will reach a maximum temperature determined by the physical properties of the glass and inclusion as well as the pulse length and energy of the incident radiation.

The first step in solving this classical problem as performed by Hopper and Uhlman was to solve the heat diffusion equation with time dependent boundry conditions for temperature, as a function of time and radial distance. Several assumptions were made in the handling of the heat diffusion equation. Firstly the inclusion is assumed to be perfectly conducting, secondly heat loss to the host material was assumed to be purely by conduction, and finally the particle host boundry resistance to heat conduction is assumed to be zero. These assumptions are discussed in detail in section 7. Hopper and Uhlman also treat an inclusion with finite thermal conductivity to determine the temperature profile existing inside the inclusion.

Sparks and Duthler(1973) also examined inclusion absorption, since they were dealing with long wavelength incident radiation,the errors introduced by using the physical crossectional area instead of the effective crossectional area become large. They considered several discrete time regions, obtaining expressions for the temperature in these regions and extrapolating the results into the adjoining areas.

Bennett(1971) treated the inclusions in the same manner as Hopper and Uhlman, obtaining virtually the same temperature verses inclusion radius relationship, but he concluded by suggesting that the particles might be detected before damage by observing the optical path length change (by phase techniques) and optical birefringence parameters both produced during exposure, these effects would appear visually much larger than the inclusion itself and hence would be easy to detect. Bennett proposed to maximize these effects by using microsecond pulse lengths for irradiation. The power requirement of such a pulse is very severe, it would have to be high enough to cause the optical path change and stress birefringence effects but not high enough to cause permanent damage. This could be a very critical practical procedure.

Most of the work to date has dealt with inclusions of platinum in one of the popular laser glasses or window materials such as aluminium oxide, neodinium doped glass, zinc selinide and cadmium telluride. In the production of the XDP materials it is very unlikly that platinum would be found as the production process is typically low temperature compared to the production of laser glasses. In section 6 techniques are described which present several possibilities for the inclusion composition.

2.9 Extrinsic breakdown identification.

The characteristic appearance of inclusion breakdown is seen as the spatial distribution of the discrete damage points. This appears as a randomly distributed set of small damage areas filling the entire volume exposed. A varifying test is the low value of threshold for breakdown.

2.10 Other damage mechanisms.

Brilloin in 1922 considered the scattering of light by thermally excited acoustic waves. Later Chiao et al(1964) discovered that Brilloins theory could be applied to an optical beam when it was scattered by the acoustic wave it had itself produced, this is called stimulated brilloin scattering.

When an optical beam and a coherent acoustic wave interact a second beam is produced by Bragg diffraction at the region of intersection. The frequency of the second optical beam is determined by the frequency of the original beam and the acoustic frequency and magnetude of the acoustic wave, the diffracted or scattered wave is increased at the expense of the input beam. Since an overall gain of acoustic and diffracted energy exists, when positive feedback is applied and losses are overcome, simultaneous oscillation of both the waves can occur. As the acoustic wave increases in magnetude the stresses produced in the crystal can cause permanent damage. The threshold for initiation of stimulated brilloin scattering is discussed in detail by Chiao et al(1964).

For XDP materials the damage threshold due to stimulated brilloin scattering at nanosecond pulse lengths is usually very high, in most cases higher than that needed for the onset of self focusing, so the observation of this type of damage alone is very difficult.

2.11 Pulse length dependence of damage mechanisms.

Bliss(1975) has examined the theories of all the damage mechanisms mentioned in this section. He produced pulse length dependence curves for the damage threshold for each of the four types of damage, and compared these with measured values for various laser glasses.

The results will give an indication of the tendences that should exist in the XDP family although the absolute values of the thresholds will be different.

Figure 2.5a shows the pulse length dependence of avalanche breakdown in aluminium oxide(ruby). The long

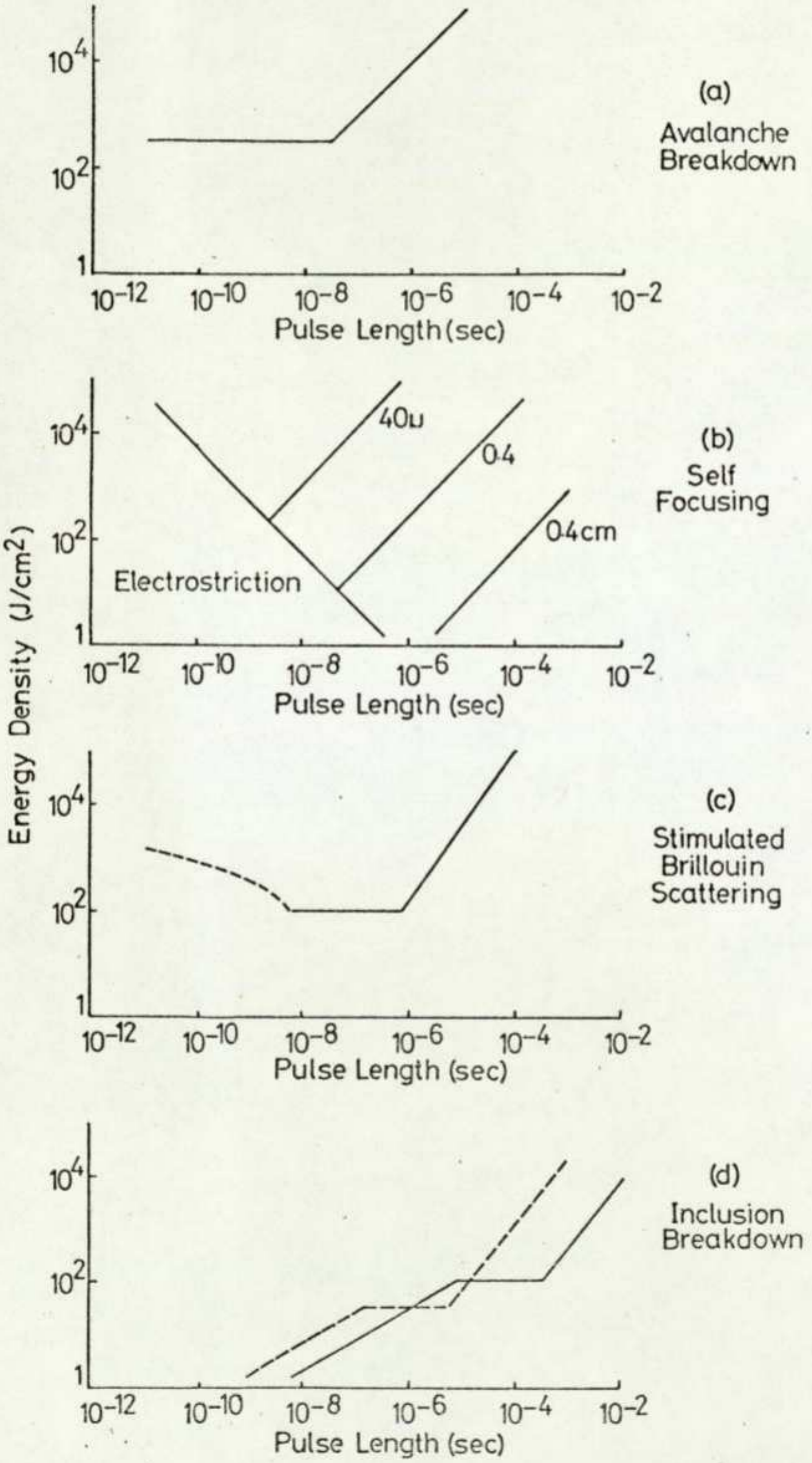

Pulse Length Dependence of Damage Types

Fig 2.5

pulse variation is a constant power process and the short pulse length variation is a constant energy process, see Bliss(1975) p108.

Figure 2.5b shows the pulse length dependence of self focusing threshold in an unspecified laser glass. The values shown are for electrostriction which was previously shown to have the lowest thresholds in the XDP materials.

Figure 2.5c shows the pulse length dependence of stimulated brilloin scattering in quartz. The dashed line is dependant on the material properties and the wavelength.

Figure 2.5d shows the long pulse length dependence of inclusion damage threshold of a glass with platinium inclusions. The dashed and full lines are fitted to two different sets of measured results. The slope in the region less than 10ns does not include the effective crossectional area compensation.

SECTION

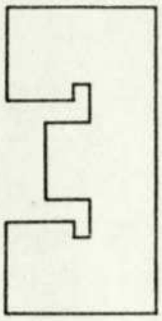

LASER CONTROL

Introduction.

The laser system used by Christmas(1973) in his damage measurements at approximately 20ns pulse length is the basis of the system used by the author for the damage measurements at varying pulse lengths. Apart from the precisely definable power density and temporal purity which was a requirement of the previous system, a fully controlable pulse width adjustment is necessary. Preliminary measurements on KD*P indicated the need for greater power as the pulse length was reduced. It was estimated that a five fold increase in power would be sufficient to cause damage at the shortest pulse lengths. An optical amplifier was considered necessary to perform this task.

In this chapter the best system for optical pulse control is considered and compared with other techniques. An optical switch is discussed together with possible arrangements that could be used for the production of single optical pulses. Arrangements for electrically driving this optical switch are also considered and a design for a fast electrical switch in the form of a laser triggered spark gap is given.

Lastly the design of a laser amplifier which produced a power gain of four with minimum pulse shape distortion is described. This amplifier was capable of considerably higher power gains.

3.1 Picosecond pulse production.

Two techniques are commonly used for producing picosecond length optical pulses. The first produces a train of mode locked pulses, from which a single pulse is extracted using a pockels cell as an optical switch. The second technique produces a so called Q-switched pulse and uses a pockels cell to switch a section out of the continuous Q-switched pulse.

A third technique involves the transmission mode of operating a laser. This can give short high power pulses but has the disadvantage that if a timing error is made on the internal switching elements extremely high uncontrollable power densities can occur within the laser cavity. A description of this mode of operation is given by Christmas(1973)

Several authors have described systems using the Q-switch chopping technique, Michon et al(1968) reported the production of one nanosecond pulses with a 450ps risetime using a 10ohm system with an externally triggered spark gap driving a neodynium glass laser Q-switch as well as the external chopping switch. The system had the disadvantage that a fixed delay between the Q-switch initiation and the peak optical output is required, which in practise does not occur. A second passive spark gap was inserted just before the external switching pockels cell. This would account for the relatively good risetimes of this system, but again introduces more jitter leading to non-repetitive power output. A mention is also made in this reference of the use of a laser triggered spark gap producing the same results as those given above.

Alcock and Richardson(1970) describe the production of a 700ps pulse with 270ps risetime. The system consisted of a laser triggered spark gap driven by a Q-switched ruby laser, the spark gap switched a 'small low capacitance' pockels cell with a 2mm aperture. The pulse length was measured using two techniques, the first an oscilloscope vacuum photo diode combination with an overall response of 470ps and the second a spectral broardening observation using a Fabry-Pérot interferometer. The former giving 700ps and the latter 800ps for the pulse length obtained. A risetime of 270ps is claimed measured with the oscilloscope photodiode combination. This appears to be questionable since the measuring system response is 450ps as mentioned previously, and a shorter pulse could have been produced if the actual risetime had been this short.

Alcock and Richardson do not elaborate on the structure of their pockels cell, except to say that the aperture was 2mm. This very small aperture should lead to a much better design of pockels cell but is not very practical. Assuming the power density limit of the crystal, coatings etc was 100MW/cm^2 (typical value for KD*P with dielectric coatings) then the peak power the system could operate with is approximately 4MW for nanosecond pulse lengths.

Ireland(1975) described a spark gap pockels cell arrangement giving approximately 400ps risetime and pulse lengths of 470ps. Ireland modified two commercially available pockels cells, one a KD*P type and the other an ADP type, by applying strip electrodes. He determined that the ADP cell did not degrade the signal from the spark gap, but the KD*P cell did,(due to the fact that ϵ_{ADP} is less than ϵ_{KD^*P}).

Ireland measured the risetime of the laser triggered spark gap to be less than 300ps using a Tektronix 519 oscilloscope and current probe combination. The laser triggered spark gap operated as a 10ohm system with five 50ohm cables connected in parallel (creating an obvious mismatch). The result of the KD*P pockels cell measurements indicated that this cell had an electrical risetime which could not have been less than 300ps, so the minimum pulse length obtainable with this cell would be worse than the pulse of 450ps obtained with the ADP cell.

To gate a single pulse from a mode locked train is relatively simple and does not require ultra-fast pockels cell switching. The pockels cell must be able to switch in the time between mode locked pulses, typically in the order of 10ns, and the electrical driver for the pockels cell must have jitter less than the difference between the mode locked pulse separation and the pockels cell risetime, which is typically a few nanoseconds. Von der Linde(1970) produced single pulses of tens of picoseconds in length using this technique.

The specifications of a system needed to produce pulses suitable for the damage investigation are basically a pulse length variation of approximately two decades and a peak power transmission of at least 20MW with definable power density distribution normal to the beam.

A discussion of the two types of pulse production will now follow to asses the suitability and scope for modification of each of the systems.

3.2 The mode locked laser.

If all but the on axis modes of a laser cavity are suppressed by ensuring symmetry of excitation and adequate physical restraints a single transverse mode of the simplest form (TEM_{00}) can be obtained. This leads to a distribution in the transverse plane being the same for all axial modes. These axial modes differ in that the position of their centre frequency is shifted from mode to mode. It can be shown that this change in frequency is given by

$$\Delta\nu = \frac{c}{2L'} \qquad 3.1$$

where c is the velocity of light and L' is the optical length of the cavity. The number of discrete axial modes that can oscillate at any time is determined by the atomic (or molecular) line width and the extent of the excitation.

If these axial modes of fixed frequency separation can be superimposed onto oneanother in time, the laser is said to be mode locked or phase locked. To determine the resulting amplitude and time structure of the pulse the expression for the oscillatory mode must be considered.

The normalized amplitude of a single mode is described by

$$\exp(i\omega t) \qquad 3.2$$

where $\omega = \omega_0 + k\Delta\omega$, $\Delta\omega = 2\pi\Delta\nu$ and ω_0 is the centre frequency, Adding 2n+1 of these waves having equal magnetude the result is

$$\sum \exp i(\omega_0 + k\Delta\omega)t \qquad 3.3$$

This function is composed of the product of $\exp(i\omega_0 t)$ and

F(t) where

$$F(t) = \frac{\sin(n+\frac{1}{2})\ \Delta\omega t}{\sin(\frac{1}{2}\ \Delta\omega\, t)} \qquad 3.4$$

This represents an amplitude modulated signal of frequency ω_0 with intensity variation given by $(F(t))^2$. A typical mode locked train of pulses is shown in figure 3.1.

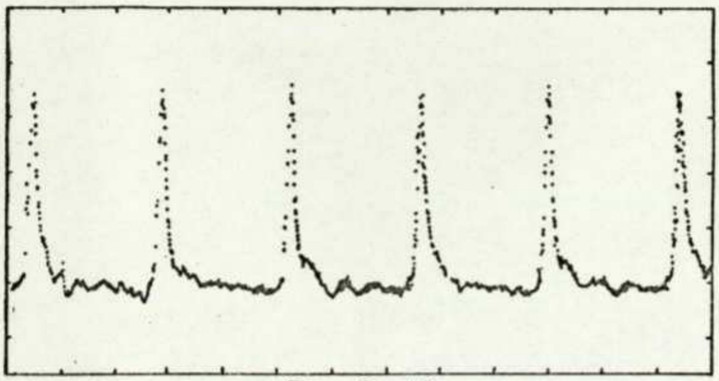

Typical Mode Locked Train of Pulses

Fig 3.1

In the region of the zero order maxima t is very small so the intensity variation is approximated by

$$\left[\frac{(n+\frac{1}{2})\ \Delta\omega t}{\frac{1}{2}\Delta\omega}\right]^2 = (2n+1)^2 \qquad 3.5$$

This means the peak intensity is $(2n+1)^2$ times the individual mode height and the approximate pulse length is

$$T/(2n+1) \qquad 3.6$$

where $T=2\pi/\Delta\omega$. The ruby laser used for the damage measurements had an optical length of approximately one meter., assuming 50 adjacent modes oscillating in phase, pulses in the order of 10^4 times the individual mode height with widths of approximately 140ps separated by 7ns would be produced.

It is obvious that to separate one of these pulses a switch with a risetime of the order of 3ns with jitter less than 4ns would suffice.

As will be shown later this specification is well within that of commercial pockels cells, and the technique does produce very good short pulses of high power.

One of the requirements for undertaking a damage investigation is the presence of an accurately specified and consistant pulse amplitude and spatial distribution. The necessity for a variable pulse length adds to this requirement. The only way of varying the pulse length of the mode locked pulse is by varying the cavity length or the number of longitudinal modes oscillating, see equation 3.6. Both these actions involve changing the cavity conditions which inevitably change to a certain extent the spatial distribution of the output beam. A second technique must be considered and this involves the Q-switched laser.

3.3 The Q-switched laser.

Any oscillating system has a quality factor Q defined as the ratio of the energy stored per cycle to the energy lost per cycle. A laser can be operated in a situation where an initial build up of population inversion occurs with the cavity operating in a high loss mode or at low Q, if at the appropriate time the Q is changed to a high value or low loss, then an output pulse will be generated which is many times larger than the cavity would produce in its conventional mode of operation. The laser is said to be Q-switched.

Several authors, Steel(1968), Ross(1969) and Lengel(1974) have discussed the derivation of the theory needed to predict the results of the Q-switched pulse length, power output and delay times. Some results of this work will be quoted here to determine the control available with this type of laser operation.

By approximating a three level laser such as the ruby laser to a simple two level system, rate equations to describe the photon density and electron density can be derived. These reduce to

$$\frac{d\eta}{dt} = \omega_p(1-\eta) - \omega_s(1+\eta) - \omega_i\varphi\eta \qquad 3.7$$

$$\frac{d\varphi}{dt} = -\varphi(\gamma_s + \gamma_o(t)) + \omega_s'(1+\eta) + \omega_i\varphi\eta \qquad 3.8$$

where η is the inversion fraction, that is the number of electrons in the higher energy level divided by the total number of electrons. φ is the photon density, ω_p and ω_s are the probability pump rate and probability spontaneous emission rate respectively, ω_s' is the latter incident along the axis of the optical aystem. ω_i is the probability stimulated emission rate. γ_s is the loss rate from absorption in mirrors, unexcited active material and diffraction losses. γ_o is the output loss rate determined by the element used to Q-switch the laser.

Consider an infinitely fast Q change within the cavity, which means γ_o changes from some value w_1 to a lower value w_2 in zero time initiated at t = 0 Then

$$\gamma_o(t<0) = w_1$$

$$\gamma_o(t>0) = w_2$$

Assuming that in the initial stages of development of the giant pulse the two probability rates ω_p and ω_s are small compared to the stimulated emission probability rate, the rate equations 3.7 and 3.8 become

$$\frac{d\eta}{dt} = -\omega_i\varphi\eta \qquad 3.9$$

$$\frac{d\varphi}{dt} = -\varphi(\gamma_s + w_2) + \omega_i\varphi\eta \qquad 3.10$$

A threshold value of inversion fraction (η_t) will exist at the point where $\frac{d\varphi}{dt} = 0$ when $t > 0$.

Using equation 3.10

$$\frac{d\varphi}{dt} = 0 = -\varphi(\gamma_s + w_2) + \omega_i \varphi(\eta_t)$$

$$(\eta_t) = \frac{\gamma_s + w_2}{\omega_i}$$

If the lifetime of a photon in the cavity is defined as

$$\tau = \frac{1}{\gamma_s + w_2}$$

then $\eta_t = \frac{1}{\omega_i \tau}$

the rate equations then become

$$\frac{d\varphi}{dt} = \left(\frac{\eta}{\eta_t} - 1\right)\frac{\varphi}{\tau} \qquad 3.11$$

$$\frac{d\eta}{dt} = \left(\frac{1}{\eta_t \tau}\right)\varphi\eta \qquad 3.12$$

Kay and Walderman(1965) consider the case of a switch having a finite transition time t_1. By taking $\gamma_0(t > 0)$ as

$$w_1 + w_2\left(1 - \frac{t}{t_1}\right)$$

which is a ramp of length t_1 and height w_2, and using the rate equations 3.7 and 3.8 they show that the change in photon density from $t = 0$ to $t = t_1$ is very small so that the simplified rate equations 3.11 and 3.12 can be used with the addition of a delay time determined by t_1. They solve equations 3.11 and 3.12 for given initial conditions of inversion fraction and a value of 5ns for t_1. Two solutions, one for $\eta_0 = 0.4$ and another for $\eta_0 = 0.3$ are shown in figure 3.2b. They assume the delay is the time taken for φ to reach 5×10^{-4}.

These results indicate that the initial pumping level determining the initial inversion fraction and the switch rate will effect the delay, pulse shape and power output.

Using this technique a pulse of several nanoseconds

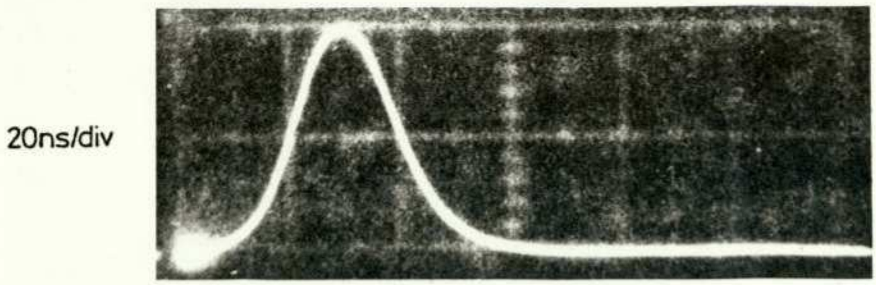

Oscillator Q switch Pulse

(a)

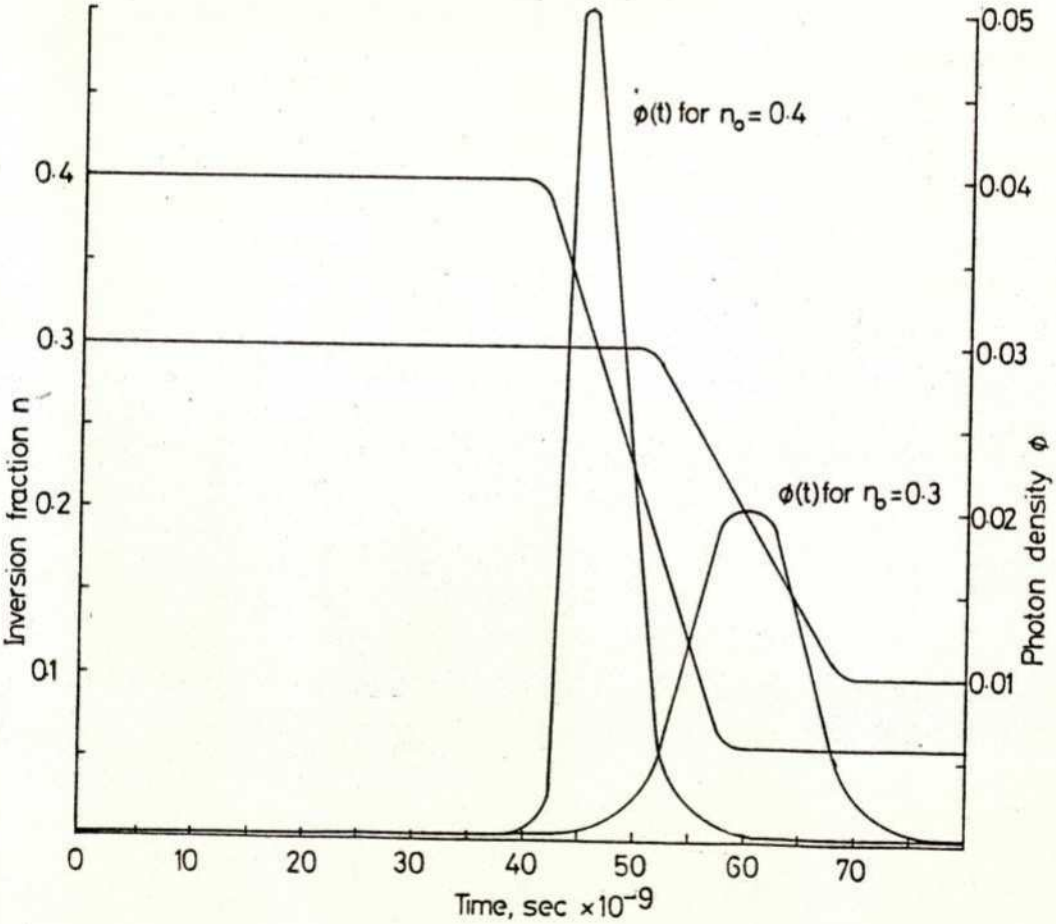

Laser Q switching (Kay et al)

(b)

Fig 3.2

can be generated with very high power output, figure 3.2a shows the Q-switch pulse obtained with the ruby laser system used in the damage measurements. A Q-switch rate of 1 nanosecond was used and the overall delay from Q-switch initiation to the peak power output was approximately 40ns. This delay was dependent on the pumping level especially in the region just above lasing threshold.

If this pulse is chopped using a fast optical switch a pulse of very high power with minimum length determined by the switches optical risetime can be produced.

The advantage of this arrangement is that the pulse length can be varied simply by altering the driving circuitry of the optical switch, with no adjustment to the optical cavity being necessary.

3.4 The pockels cell.

Each of the previous techniques requires a fast optical switch as an active element. An acousto-optic modulator can be used as a switch but is inherently slow in response time. Transverse electro-optic modulators have the advantage of having a low operating voltage but again their risetime is slow. Longitudinal electro-optic modulators of the pockels cell type are very fast and are physically suited to being matched into very fast electrical circuitry, they have the disadvantage that several kilovolts are required to drive them, but their superiority in speed of response makes their use ideal for ultra-fast switching. A description of the theory of operation of the pockels cell is given by Yariv(1967). The crystal orientation for optimum electro-optic effect is discussed as well as the assesment of different materials for use in a pockels cell.

A description of the practical aspects of pockels cell use is needed to show where the risetime limitations lie.

The physical problems associated with the design of an ideal pockels cell are that of applying the voltage to the crystal in the shortest possible time, but maintaining an even voltage gradient within the crystal during this period. These are two separate problems, leading to the incremental spatial risetime limitation in the former case, and spatially even extinction ratio in the latter case.

Most commercial pockels cells sold today consist of a cylindrical crystal with ring electrodes (Steinmetz (1973)), applied to each end. The two terminal pockels cell consists of the input and output terminals connected to one end of the crystal and the other end earthed. A four terminal pockels cell consists of an input and output terminal connected to one end of the crystal and a second pair of input and output terminals connected to the other end.

A survey of the use of these two types of pockels cells will now be considered showing the comparative results of some common and a novel configuration for short pulse generation.

Section 4 deals with the design of a pockels cell which gives a shorter risetime than has been obtained with a coaxial system to date.

The physical arrangement used to generate a single variable length pulse using a pockels cell can effect the dynamic response of the pockels cell. Two common methods of converting a fast voltage risetime into a voltage pulse of variable length are shown in figure 3.3 a)and b), a) relying on the time taken for a pulse to undergo the round trip to and from a short circuit, and b) using the time it takes for a pulse to travel from one end of the element to the other end of the element through an external line. Figure 3.3 c) and d) show an alternative method of obtaining the voltage pulse which was developed during the course of this work, it uses the time difference between two separate pulses reaching the element ends through two separate lines. The pockels cell in a) is a two terminal type and the pockels cells in b) and c) are four terminal types. The four terminal pockels cell can

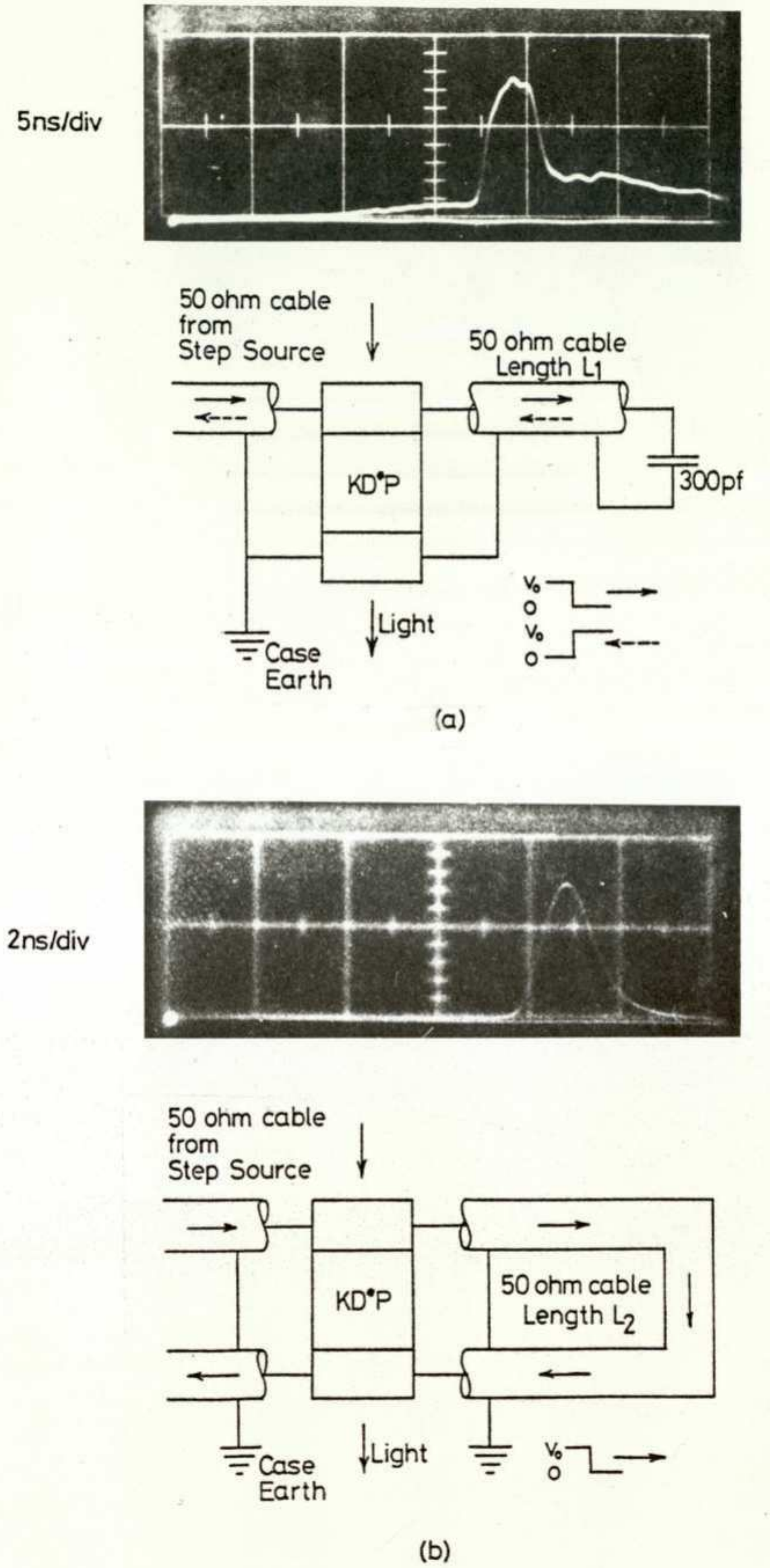
5ns/div
50 ohm cable
from
Step Source
50 ohm cable
Length L_1
KD*P
300pf
Light
Case
Earth
V_o
0
V_o
0
(a)
2ns/div
50 ohm cable
from
Step Source
KD*P
50 ohm cable
Length L_2
Case
Earth
Light
V_o
0
(b)

Fig 3.3

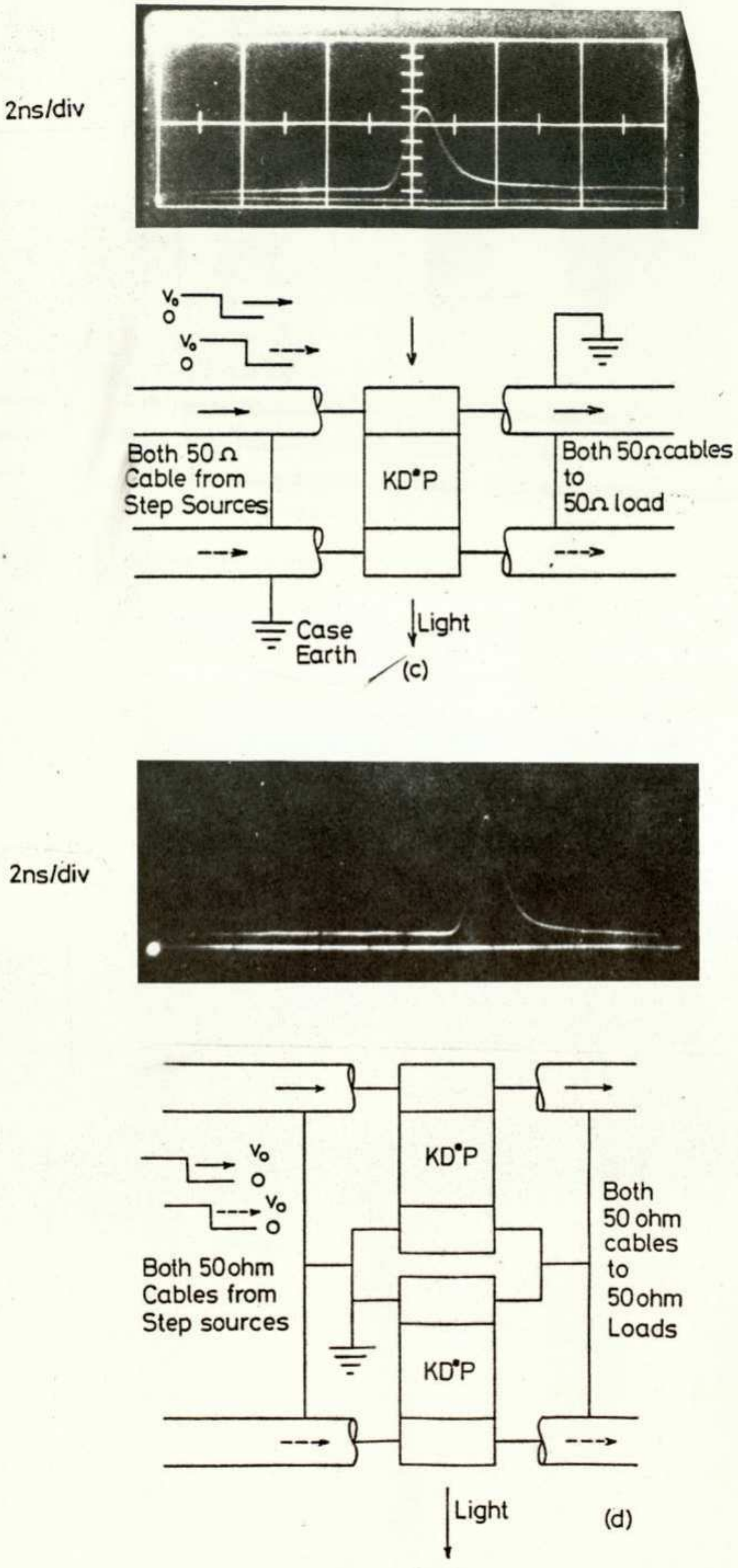
2ns/div
V_0
0
V_0
0
Both 50 Ω Cable from Step Sources
KD*P
Both 50Ω cables to 50Ω load
Case Earth
Light
(c)
2ns/div
KD*P
V_0
0
V_0
0
Both 50ohm Cables from Step sources
KD*P
Both 50 ohm cables to 50ohm Loads
Light
(d)

Fig 3.3

be made up of two separate two terminal pockels cells as in figure 3.3 d).

The optical pulses obtained in each case are shown directly above each of the physical layouts in figure 3.3. The pulse in a) has a fall time which is slower than the risetime, this is due to both the degredation that occurs after the first trip over the element (due to the impedance mismatch) and the inductance of the capacitor used to terminate the line. The residual light that is transmitted after the pulse results from the inherent series resistance in the capacitor and connecting leads. If the switching arrangement could be altered so that the capacitor was not necessary (the voltage was switched from zero up,instead of being shorted out) and the pockels cell could be arranged to have a minimum mismatch, this technique could produce very good results. The pulse in b) shows a very good risetime and extinction ratio both before and after the pulse but again the falltime is greater than the risetime. The result for c) is similar to that for b) the fall time degradation is due to a problem inherent with the four terminal pockels cell design. This problem arises where there is a mismatch of the crystal and the connecting line, the mismatch being capacitive creates a high frequency short circuit across the external line, this induces a small pre-pulse in the line opposite to the initiating line and thus reduces the risetime of the voltage across the crystal element. Figure 3.4 shows the response of the Electro-Optic Developments PC105 four terminal pockels cell, the small pre-pulse is the induced voltage from one line to the other, its amplitude is approximately 25% of the peak voltage and its half width is 300ps with a 180ps applied pulse risetime. This would present a severe limitation on the minimum risetime achievable using this pockels cell.

Figure 3.3 d) shows a pulse with good rise and fall times produced by two separate pockels cells driven from two separate lines. This appears to be the best arrangement for producing reliable short symetrical pulses.

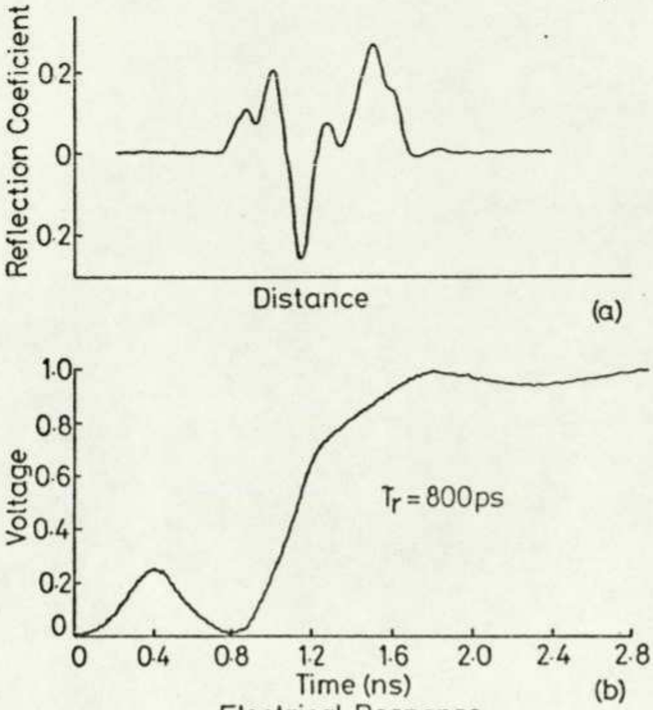

Electrical Response
of E.O.D. PC105 Pockels Cell

Fig 3.4

Figure 4.11 shows the final arrangement used to investigate the damage thresholds, the spark gap used for generating the separate pulses is an integral part of the complete system.

3.5 Full wave switching.

A technique which theoretically appears to produce the shortest pulse length with a given pockels cell is called full wave switching and is illustrated in figure 3.5. The pulse length produced should be approximately half the risetime of the voltage applied to the pockels cell. This is half as long as the minimum pulse length obtainable with the same electrical risetimes and arrangements in figure 3.3. A distinct disadvantage is that the voltage applied to the pockels cell has to have a uniform voltage slew rate to produce falltimes equal to the risetime. In practice this voltage pulse is usually far from ideal as will be seen in later sections on the krytron and laser triggered spark gap. This characteristic shape shown in figure 3.5 a) was originally reported by Fletcher(1949), figure 3.5 b) shows a typical optical pulse using a laser triggered spark gap as a voltage source. The risetime is very fast but the falltime is poor, this technique should only be considered if the risetime only is of prime importance.

Several unsuccessful investigations were undertaken to try and improve the voltage pulse obtained from the laser triggered spark gap. These involved the use of gases other than nitrogen as well as liquids in the gap. This varified that the best material of those tried was nitrogen.

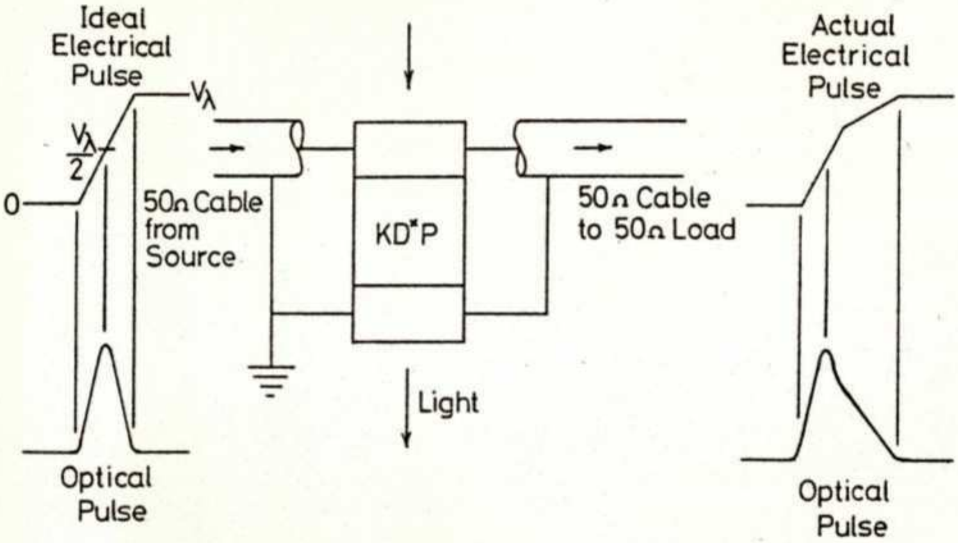

Full Wave Switching

(a)

(b)

Fig 3.5

3.6 Krytron switch.

An electron tube device manufactured by EG&G(USA) can switch 5kV at 100amps with a risetime of 1 nanosecond. This device is a KN22 krytron and is the heart of many commercial systems developed for driving pockels cells. The principle of the krytron with its avalanche transistor driver is described by Christmas(1972). In the application considered here two such switching systems were required, one to initiate the Q-switch operation and a second unit triggered a fixed time after the first to drive the pulse shaping pockels cell. A block diagram of such a system is shown in figure 3.6.

EG&G KN-22B Krytron	
Max. Voltage	5 kV
Max. Current	100 A
Risetime	1·0 ns
Falltime	1·0 ns
Jitter	4 ns
Delay	40 ns

Krytron Specification
Table 3·1

A timer is initiated at the instant the laser flash tubes are fired. After the required time corresponding to the peak of the optical flash cycle, the Q-switch krytron and the pulse chopping krytron are fired simultaneously. The short delay necessary for the chopping pulse to reach the chopping pockels cell at the appropriate instant, corresponding to the peak of the Q-switch optical output, is derived by using the correct cable length between the krytron switch and the pockels cell ($L_2 - L_1$ in figure 3.6)

Limitations of this type of step voltage generator become evident when the krytron specifications are studied,

Table 3.1 shows the specifications from EG&G data sheet No. KN22 for their KN22 krytron.

The basic limitation determining the minimum pulse length obtainable is given by the rise and fall times. It can be seen from the data that a pulse length shorter than 1.5ns is not possible.

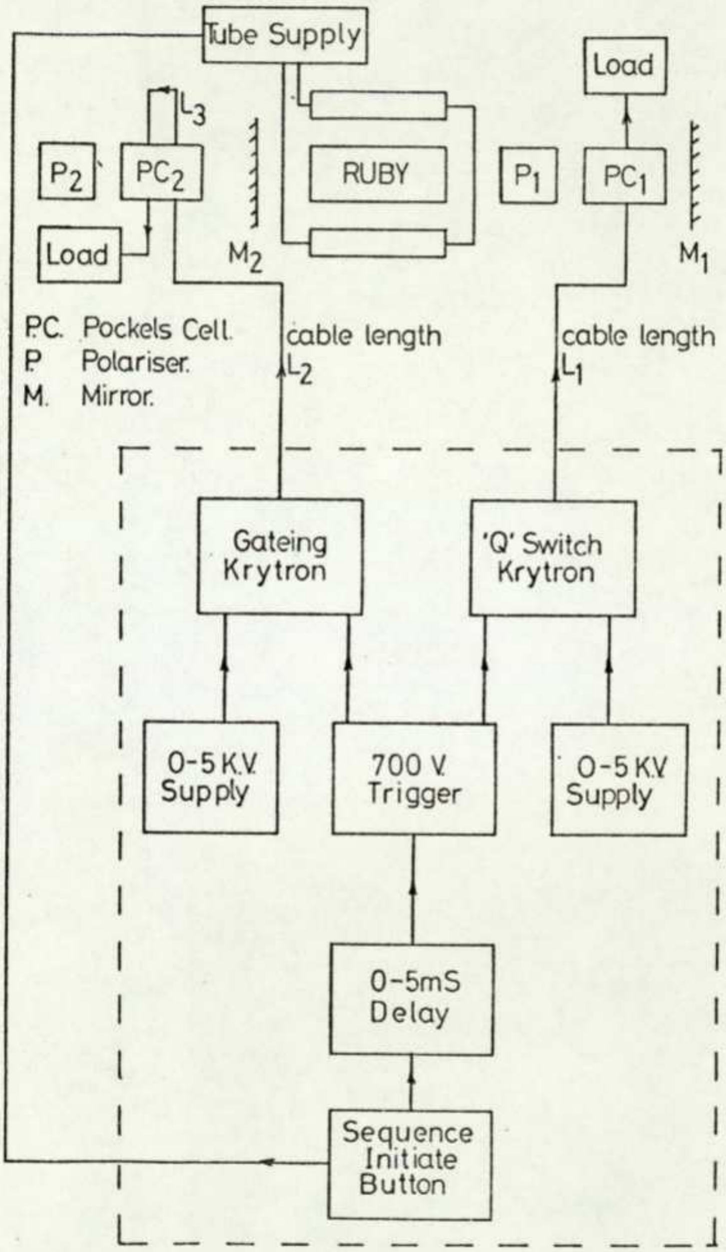

Block Diagram of Krytron Pockels Cell Drivers. and Laser System.

Fig 3.6

Fig 3.7 Krytron Performance

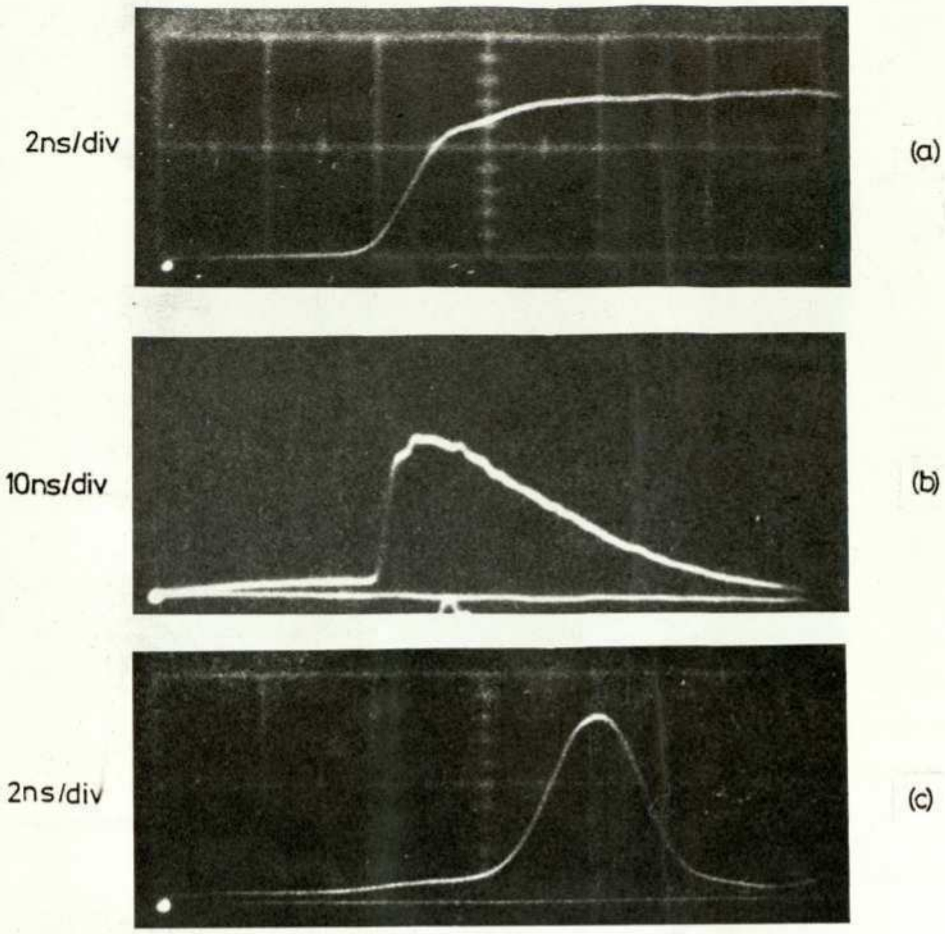

Fig 3.8 Pulse Length Limitation

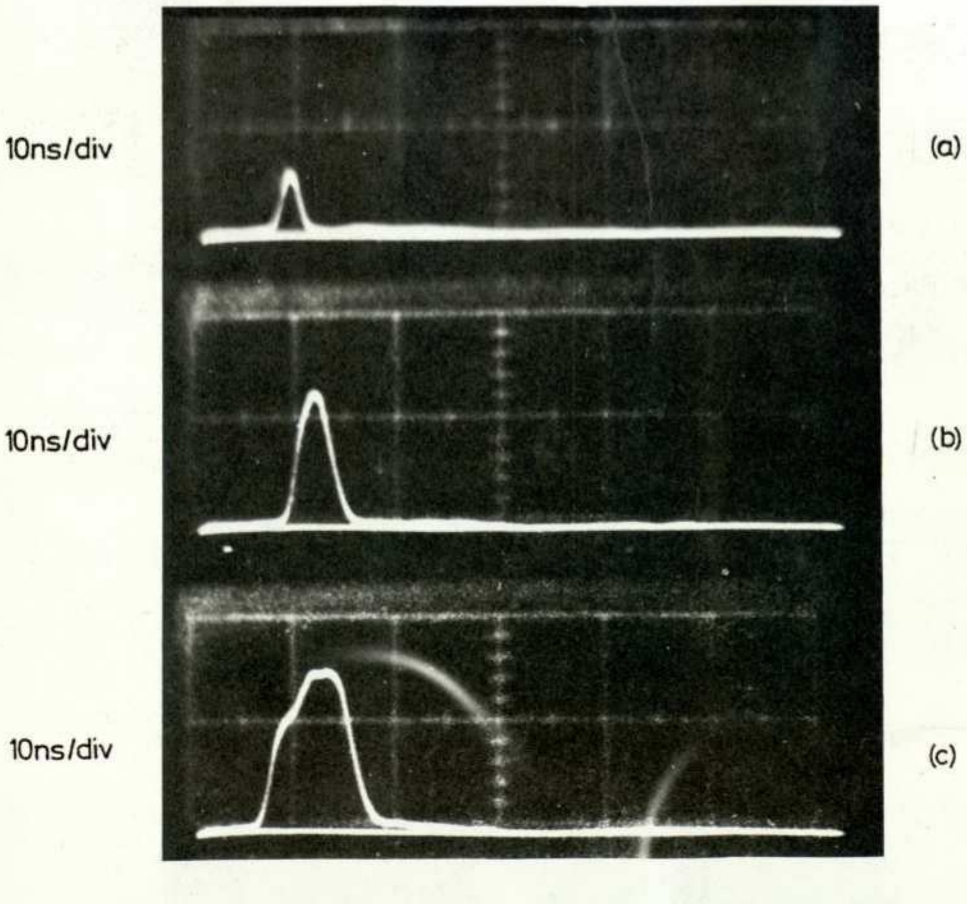

A further limitation occurs as a result of the 4ns jitter on the switching time. If the pulse to be chopped is 20ns long and a jitter of 4ns exists on the switch, an amplitude jitter of up to 10% can result assuming the initial pulse shape to be gaussian.

Appendix2 contains the circuit diagrams of the unit constructed to provide optical pulses ranging from 20ns to 2ns in length. Figure 3.7 a) shows a typical current pulse produced in a 50ohm coaxial cable using the unit described in appendix2. The linear portion of the risetime is approximately 1 nanosecond long, the two stage risetime discussed previously is also evident.

Figure 3.7 b) shows the optical output when the circuit in appendix2 drives a two terminal pockels cell, Electro-Optic Developments type PC105. Figure 3.7 c) shows the minimum optical pulse output using a four terminal pockels cell, Electro-Optic Developments type PC105-4 utilizing an 8cm loop of coaxial cable (L_3 in figure 3.6). Both these optical pulses were produced by switchimg the 20ns pulse from the Q-switched ruby laser. The length of the pulse in figure 3.7 c) is approximately 2ns, the pulse that should be produced by an 8cm loop of cable is 0.4ns, this means the pulse length is being limited by the response time of the system. This can be seen more clearly in figure 3.8. a) shows an 8ns pulse produced with a loop of approximately 150cm length, b) shows a 3ns pulse produced with a 60cm length of cable and c) shows a 2ns pulse produced with a 20cm length of cable. The 20cm loop should produce a 1ns pulse, however shortening the loop beyond the response time of the system results in a decrease in pulse amplitude only, the length being limited to 2ns.

The switching efficiency of the chopping system can be seen in figure 3.9, a) shows the resulting pulse switched out and b) shows what remains of the original Q-switch pulse. It can be seen that approximately 95%

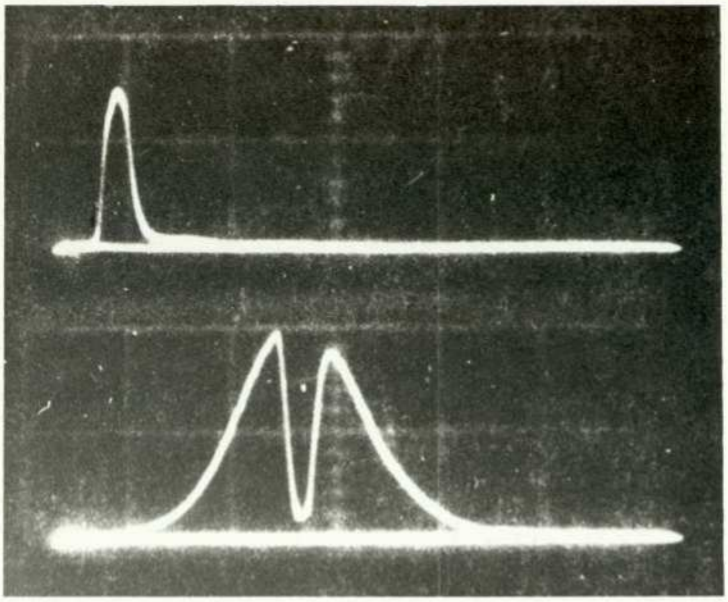

Fig 3.9 Switching Efficiency

of the power is transferred to the switched pulse, the actual value could be higher than this as optical interference from one detector to the other proved to be appreciable.

A configuration of two four terminal pockels cells driven by the krytron circuit producing two pulses of programable length and separation is described in a publication in appendix 5.

3.7 The laser triggered spark gap (LTSG).

Since Guenther and Griffin demonstrated the first LTSG in 1963 wide use has been made of the device mainly for operating electro-optic shutters used in high power laser systems. Michon et al (1968) describe a 10ohm LTSG which was used to drive an over voltage sharpening spark gap situated just before the pockels cell, pulses of

1ns were derived with this system. Since Michon, Alcock et al(1970), Von der Linde et al(1970) and Ireland(1975) have shown slight improvements in both LTSG and pockels cell design, producing pulses today of slightly less than 0.5ns. Although it is expected that the pockels cell is the limiting factor at these pulse lengths, since LTSGs have produced measured risetimes of less than 300ps, it is puzzling that a commercial pockels cell* of 90ps electrical risetime is available yet the literature indicates the absolute minimum pulse length achieved (Ireland) is approximately 0.47ns. The absence of a system capable of producing pulses less than this value prompted the investigation undertaken in this and section 4.

The LTSG has been used for its inherently fast risetime, low jitter, and high voltage switching capacity, even though to this date no practical optimization has been published.

The first step in the optimization procedure is to develop a theoretical expression for the risetime as a function of the controllable physical conditions under which the LTSG operates. The breakdown of a spark gap consists of two definate time regions, the first termed the statistical delay time. This delay has been discussed by many authors, and two basic theories describing the breakdown predominate. The Townsend theory, Townsend(1910), describes an exponential increase of electrons initiated by one which ionizes several others as it travels from one electrode to the other, each generated electron initiating the same ionization process. The second theory is the streamer theory of breakdown, Raether(1939), which accepts the Townsend exponential increase of electrons up to a certain level where due to electric field distortion and photo-ionization the rate of development increases above the exponential level creating a spark channel connecting the anode to the cathode.

*Lasermetrics inc. model 1080 pockels cell.

The second time region, that is the formative time region, is the period when the resistance of the gap changes, starting from a very high value and ending in a very low value, producing a subsequent increase in current.

Hess(1975) has considered, from a purely theoretical view, the electrical power and its half width for a spark gap. His resulting expression for the risetime is

$$T = \Delta t = \frac{3.5\ P}{E^2 a} \qquad 3.11$$

where P is the pressure in the gap in torr, E is the electric field in V/m and a is a constant dependant only on the gas used, for nitrogen Hess determined that $a = 418$ torr $cm^2\ V^{-2} s^{-1}$.

The results using Hess's theory will now be compared with results derived from emperical equations developed by Sorensen and Ristic(1977) from their experimental results.

Sorensen and Ristic describe a method of investigating the time varying spark resistance R(t). By using their experimental results they derive an equation to describe the observed values of R(t) and hence an expression for the current risetime.

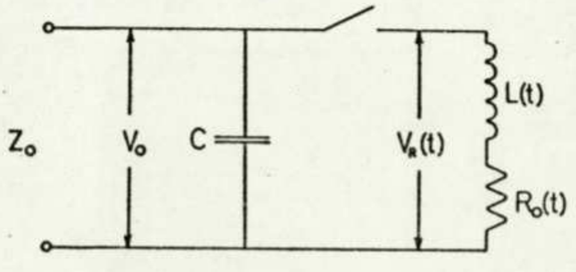

Equivalent Circuit of LTSG

Fig 3.10

The equivalent circuit of the spark gap used as a shorting element at the end of a coaxial line is shown in figure 3.10. The discharge starts as a very narrow arc and grows in diameter with time, Rees(1973). This is effectively a time varying inductance L(t). The growth rate has been shown, Rogowski(1928), to be approximately 10^7 m/s for the first nanosecond. The inductance in the very early stages of the discharge will be high. If the inductance is considered for the period after 100ps it will be approaching zero as the plasma widens to become comparable with the electrode dimensions. The worst case will occur when L(t) is a maximum which will be at the 100ps time. The time constant L(t)/Zo must be less than 100ps if it is to have little effect after this time. The inductance per unit length of a coaxial cable is

$$L = 0.0046 \log_{10} \frac{b}{a} \quad \mu H/cm$$

where b is the inside diameter of the outer conductor and a is the outside diameter of the inner conductor in this case the discharge diameter, the dielectric is assumed to be a gas with $\epsilon = 1$. The total inductance of a gap of length ι is

$$L = \iota \times 0.0046 \log_{10} \frac{b}{a} \times 10^{-6} \quad H$$

the condition for the gap to be uneffected by the inductance is

$$L/Z_o < 10^{-10} \text{ s}$$

that is $$\iota \times 0.0046 \log_{10} \frac{b}{a} \times 10^{-6} < 10^{-10} Z_o$$

After 100ps the plasma diameter a will be approximately 0.01mm. A typical inner diameter of the outer conductor of a LTSG is b = 20mm. The condition for ι becomes

$$\iota < Z_o \ 0.0062 \text{ cm} \quad \text{———} \quad 3.12$$

for a 50ohm system

$$\iota < 3\text{mm}$$

The gap length has to be less than 3mm if the time varying inductance L(t) is to be neglected. This is the case for voltages of approximately 5kV and pressurized nitrogen gas.

The analysis of the equilavent circuit of the LTSG now becomes simpler. The time varying voltage can be described by equation 3.13 when basic circuit theory is applied to the circuit in figure 3.10.

$$V_o + V_\sigma(t) + V_\iota(t) + CR_o(t)\frac{d(V_o+V_\sigma(t)+V_\iota(t))}{dt} = R_o(t)(V_\iota(t)-V_\sigma(t)/Z_o \qquad 3.13$$

$V_\iota(t)$ is the incident voltage from the charging end of the line $V_\sigma(t)$ is the voltage reflected from the gap after it has closed. $V_o, C, R_o(t)$ and Z_o are shown on figure 3.10. $V_\iota(t)$ can be neglected since the charging time is much longer than the discharge time. Equation 3.13 can be rearranged to give $R_o(t)$

$$V_o + V_\sigma(t) + CR_o(t)\frac{d(V_o+V_\sigma(t))}{dt} = \frac{-R_o(t)\ V_\sigma(t)}{Z_o}$$

$$\frac{R_o(t)}{Z_o}(V_\sigma(t) + CZ_o\frac{d(V_\sigma(t)}{dt}) = -(V_o + V_\sigma(t))$$

$$\frac{R_o(t)}{Z_o} = \frac{-(V_o + V_\sigma(t))}{V_\sigma(t)+CZ_o\frac{d}{dt}V_\sigma(t)} \qquad 3.14$$

The measurements by Sorensen and Ristic involve using a conducting loop inbedded in the dielectric of their coaxial cable, which measures the rate of change of current in the cable. The measuring system suggested by the author uses a current probe described by Wildey(1973) and produces a voltage proportional to the actual current. The analysis of this arrangement follows.

If $v(t)$ is the voltage from the current probe of restance r then

$$\begin{aligned} v(t) &= rI(t) \\ &= KrV(t) \end{aligned}$$

where $V(t)$ is the voltage at the position of the probe, and $K = 1/Z_o$. Differentiating with respect to time,

$$\frac{dv(t)}{dt} = Kr\,\frac{dV(t)}{dt}$$

substituting into equation 3.14

$$\frac{R_o(t)}{Z_o} = \frac{-(V_o + \frac{v(t)}{Kr})}{(\frac{v(t)}{Kr} + CZ_o\,\frac{1}{Kr}\frac{dv(t)}{dt})}$$

$$= (KrV_o + v(t))(v(t) + CZ_o\,\frac{dv(t)}{dt})^{-1} \qquad 3.15$$

This results in the normalized spark gap resistance $R(t) = \frac{R_o(t)}{Z_o}$ being a function of the measurable quantities $v(t)$ and $\frac{dv(t)}{dt}$ Sorensen and Ristic obtain a value of $R(t)$ as a function of $v(t)$ and $\int v(t)$ the latter being harder to determine than $\frac{dv(t)}{dt}$.

Sorensen and Ristic plot their experimentally deduced values of $R(t)$ verses time for various impedance cables. The result is shown in figure 3.11 by the heavy points. They show that the curves that best fit these results are given by the emperical equation,

$$R(t) = 2(P^{\frac{1}{2}}/EZo^{\frac{1}{3}}t)^{3} \times 10^{4} \qquad 3.16$$

The risetime can be derived from $R(t)$ by defining it as the time required for the current to change from 10% to 90% of its final value. The current in the cable will be

$$I(t) = \frac{V_o}{Z_o + R(t)}$$

let $R(t) = \frac{R_o(t)}{Z_o} = Mt^{-3}$ from equation 3.16

for the 10% level $\qquad 0.1\,I_o(t) = \frac{I_oZ_o}{Z_o + Z_oMt_1^{-3}}$

that is $\qquad t_1 = (\frac{1}{0.1M} - \frac{1}{M})^{\frac{1}{3}}$

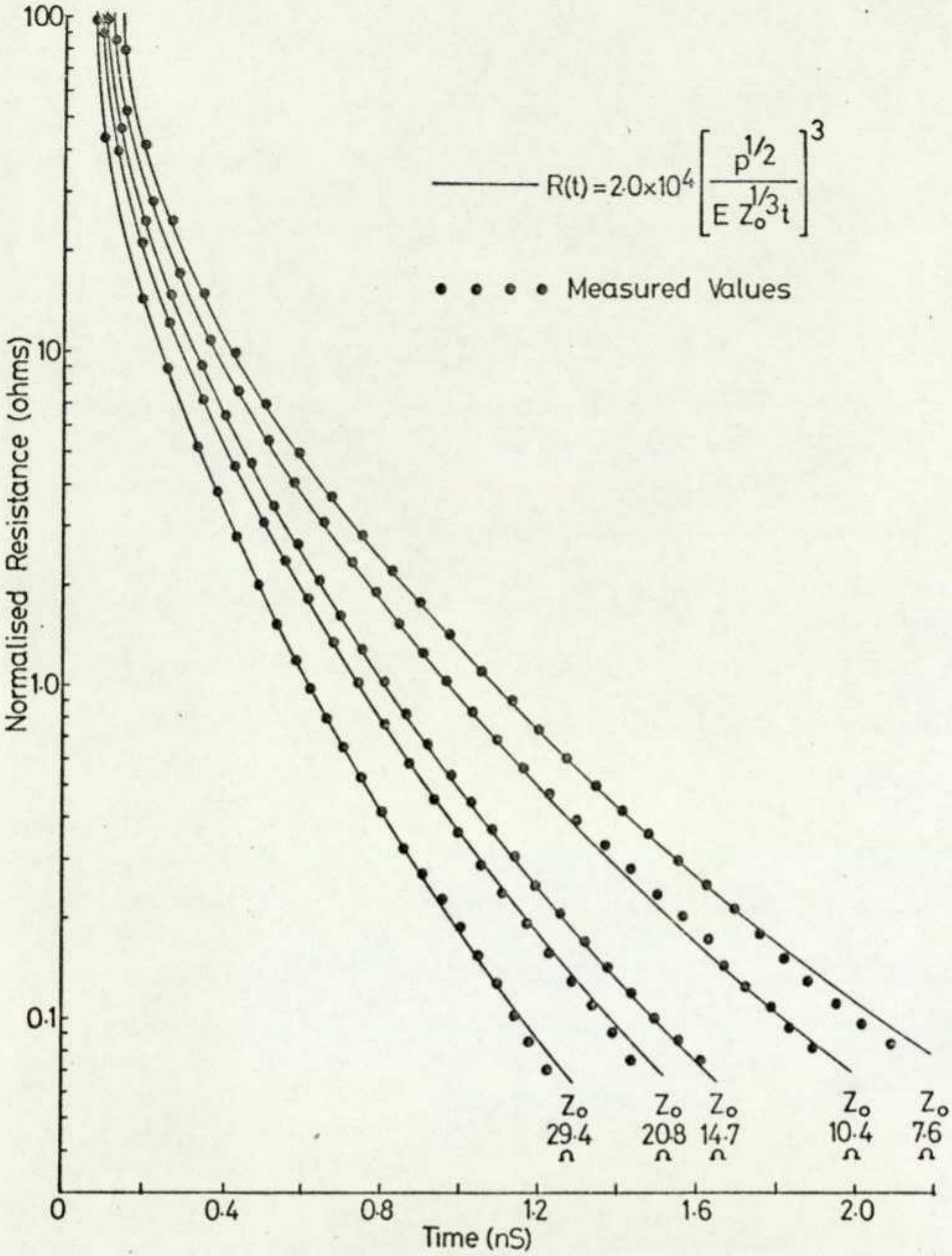

Spark-gap Resistance (Sorensen)

Fig 3.11

similarly for the 90% level

$$t_2 = \left(\frac{1}{0.9M} - \frac{1}{M}\right)^{\frac{1}{3}}$$

subtracting,

$$t_1 - t_2 = T_r = M^{\frac{1}{3}}(2.08 - 0.48)$$

$$= 43.5\ P^{\frac{1}{2}}(EZ_o^{\frac{1}{3}})^{-1} \qquad 3.17$$

P is in atmospheres, E is in 10kV/cm, Z_o is in ohms and t is time in nanoseconds.

Two LTSG's were built by the author, the first shown in figure 3.12 a) is a single terminal 50ohm system designed to operate up to 8kV and 200 psi pressure. The second is shown in figure 3.12 b) and is a two terminal unit consisting of two 50ohm lines connected in parallel giving an effective impedance of 25ohms and operates up to 10kV at 250psi with a variable gap that can be set to an accuracy of 10microns from zero to 2cm. Workshop drawings of the two spark gaps are given in appendix 3.

There are two methods of applying the laser radiation to generate the overvoltage field at the gap. The radiation can ionize a volume of gas between the electrodes or the radiation can be incident on one electrode ionizing a volume of the electrode material. The latter method produces discharges at lower radiation levels(partly due to the higher absorption of a metal compared to a gas at 0.69 microns wavelength), this was the method used by the author.

When considering the optimum physical arrangement for the LTSG it is noted in equations 3.17 and 3.11 that both expressions for risetime reduce in magnetude as E increases and P decreases.

The gap is operated as close to selfbreakdown as possible with

$$V/V_S \simeq 0.95$$

where V is the applied voltage and V_S is the DC selfbreakdown voltage. Paschens law predicts a fixed relationship between V_S and P. If this is taken into account then P can be represented as a function of V. In practice deviations from Paschens law occur and there is a limiting value of V regardless of pressure (Von Hipple(1954)).

After a conditioning time of at least 1000 discharges a plot of V_S against pressure revealed the result in figure 3.13, for the three gap settings shown.

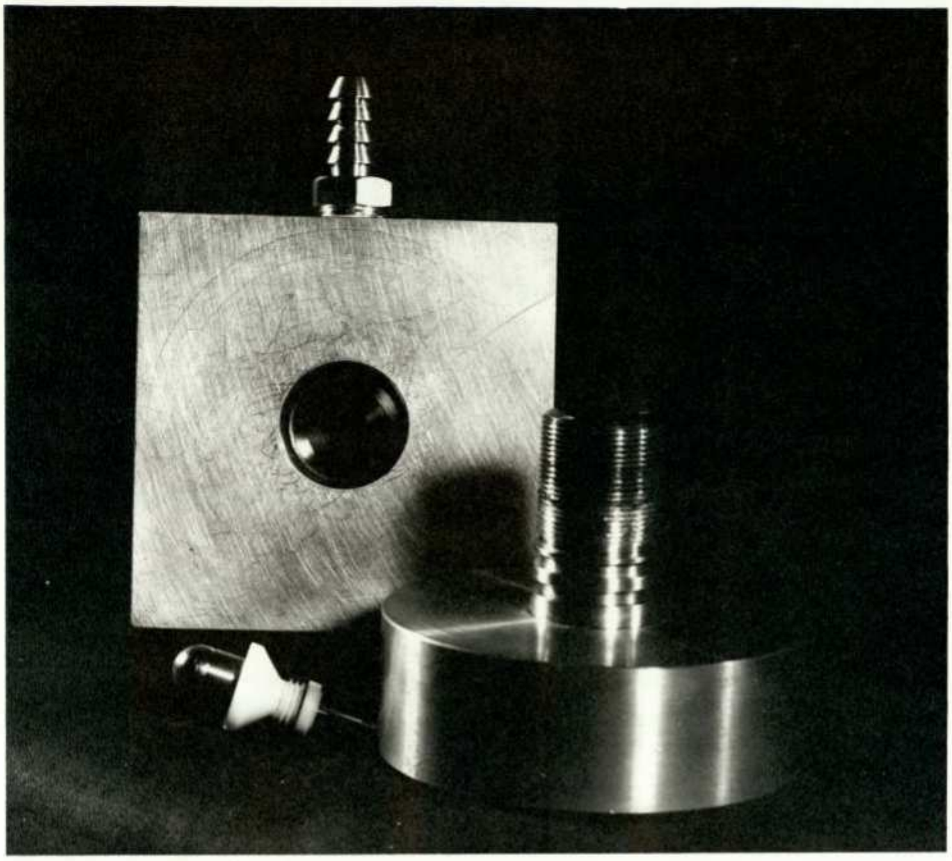

Fig 3.12(a) Single Terminal LTSG

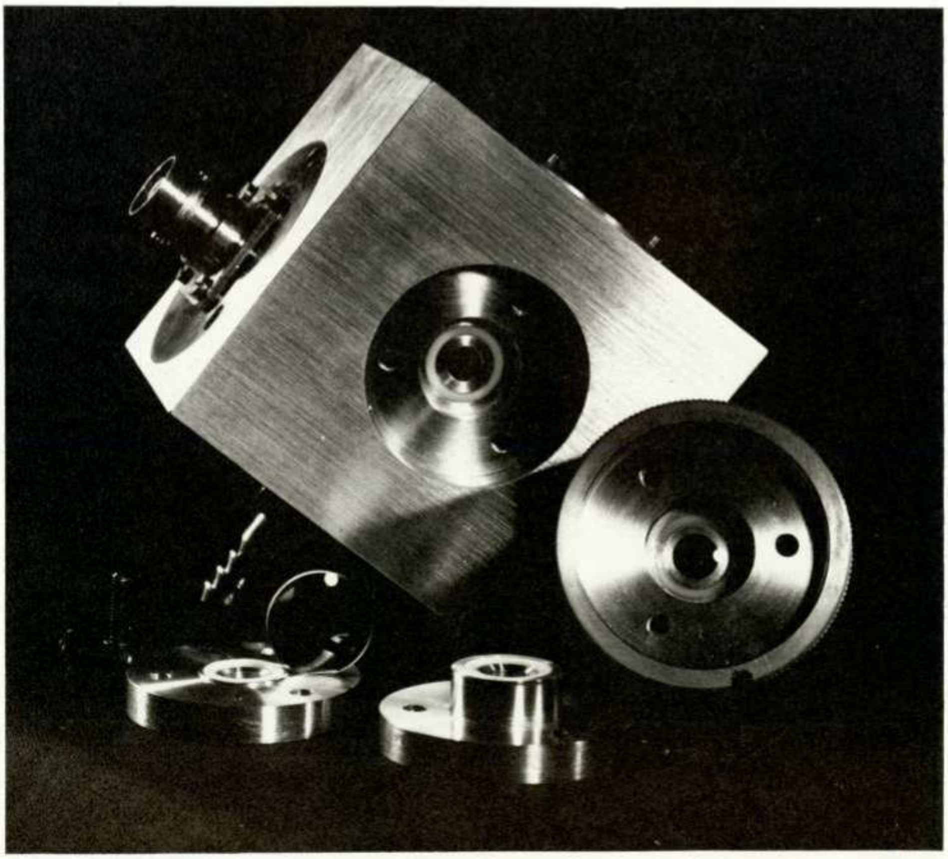

Fig 3.12(b) Two Terminal LTSG

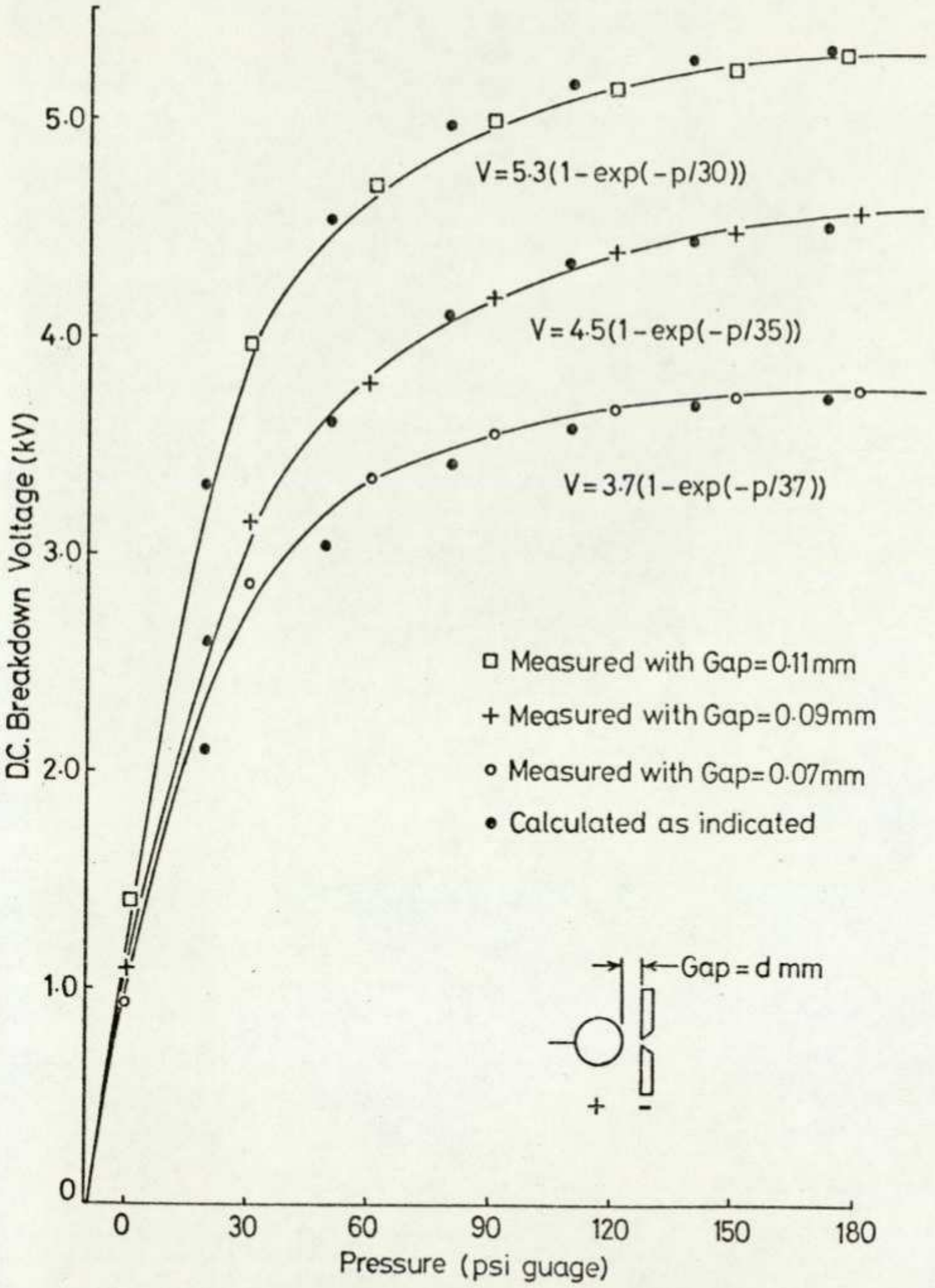

Fig 3.13

Since no unique value of V_s occurs a definition of this voltage is required. Figure 3.13 was plotted by taking V_s as the highest voltage that would produce a discharge less than once every 10 seconds.

It is evident from this graph that a minimum of T_r will occur since in the initial region where $P \alpha E$, T_r will decrease but in the latter region where E is approximately constant T_r will increase.

When the relationship between P and E as shown in figure 3.13 is substituted into equation 3.11 and 3.17 the results of the risetime verses pressure curve produce a minimum, this is shown in figure 3.14 corresponding to a gap width of 0.11mm. Hess's results give slopes which are the square of those given by Sorensen and Ristic. Measured values of risetime for the 50ohm LTSG built by the author are given as the error bands in figure 3.14.

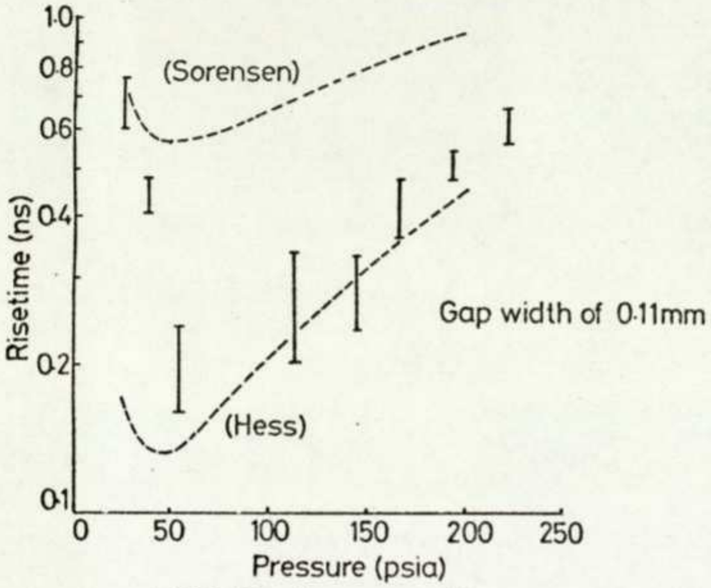

LTSG Risetime verses Pressure

Fig 3.14

The risetimes were measured with a current probe oscilloscope combination, the risetime of which was not accurately known. Later measurements of optical risetime of a pockels cell driven from this LTSG allowed an estimate of the actual risetime to be made. Using the known nonlinear response of the pockels cell, the electrical risetime of the pockels cell and the optical risetime of the complete system (measured with a streak camera), the minimum risetime was calculated to be 180ps. When this is used together with the actual measured risetimes the measuring system risetime can be found. This was approximately 325ps for the current probe oscilloscope combination.

This figure was used to calculate the actual risetimes in figure 3.14. These risetimes are seen to fit Hess's relationship around the minimum point, but approach Sorensens results for pressures outside this range. It appears as though the constant value in Sorensens equation 3.17 is dependent on his experimental arrangement or measuring system.

By combining the relationship in figure 3.13 with equation 3.11 an expression for the risetime T_r in a practical LTSG is determined as

$$T_r \ \alpha \ P(a(1-\exp(-P/P_1))^2)^{-1}$$

where P_1 is a constant of the gap and gas, valid for the range of measurements taken.

For a given situation of voltage required and V_s verses P known, a LTSG can be operated at its most efficient point producing the fastest risetime. For the spark gap used to give the results in figure 3.13 operating at the half wave voltage of KD*P of 3.6kV the optimum pressure was approximately 50 psi. The current risetime obtained is shown in figure 3.19 on page 62.

The result of the V_s verses P plot for a LTSG is the factor which determines the minimum risetime and the pressure at which it occurs. The point where the curve deviates appreciably from the linear region is dependent on the electrodes that make up the gap for a given gas. Several authors have considered the effect of electrode material, shape and conditioning. These important results are summerized below.

From both equations for risetime it is clear that the ratio of pressure to the field squared determines the value of risetime (or square of the risetime). This means the steeper the slope of the V_s verses pressure curve and the higher the voltage reached for a given gap width the better will be the gap for use as a fast switch. Appendix 5 contains a publication reporting the above findings.

Electrode material.

The work by Trump et al(1950) shows that using nitrogen gas the material giving the best shaped curve of breakdown voltage verses pressure was stainless steel with aluminium giving considerably lower limiting values of V_s. Figure 3.15 gives their results for various gases including nitrogen. These results indicate that air, CO_2 and CO_2+N_2 mixture have better curves, but these cannot be used as a fast switch due to the electro-negative effect of the oxygen atom.

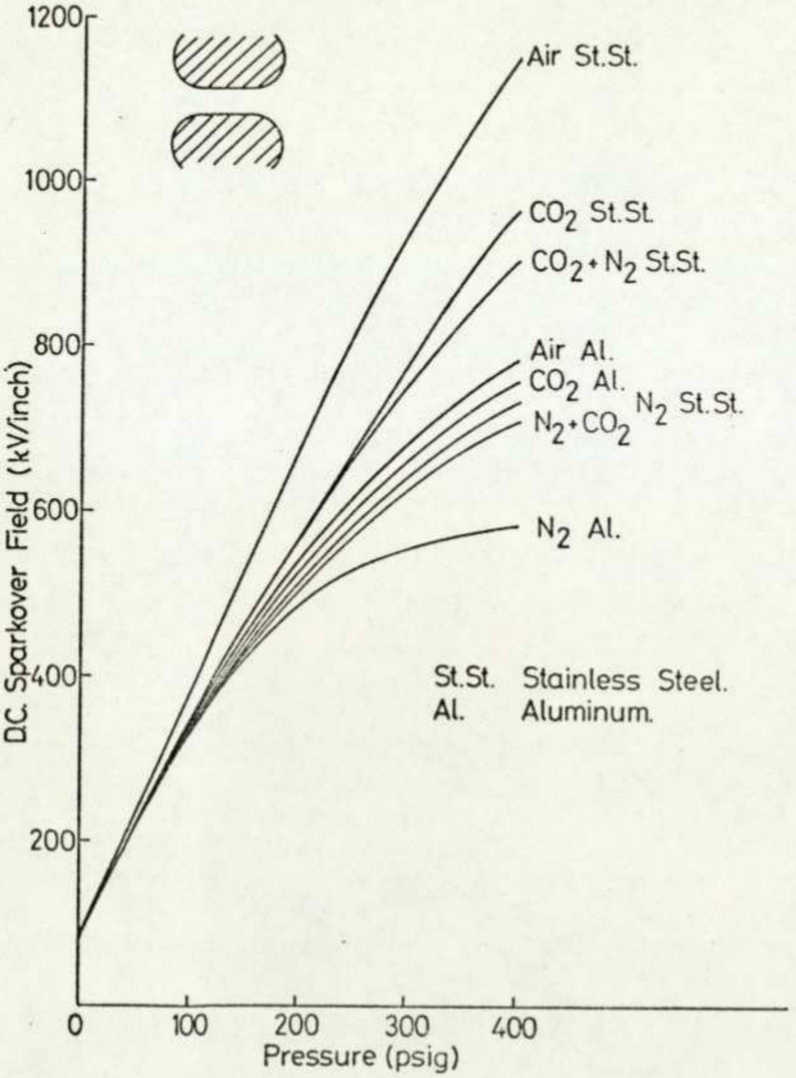

Electrode Material Effect (Trump et al)

Fig 3.15

Electrode conditioning.

The surface finish of the electrodes also play an important part in forming the shape of the self breakdown voltage verses pressure curve. When the electrodes are finished with a highly polished surface there are still microscopic irregularities which tend to create a non-linearity of the electric field in the region, reducing the voltage at which the gap will breakdown. If the gap is made to breakdown with low energy electric discharges these irregularities can be reduced, this is called electrode conditioning.

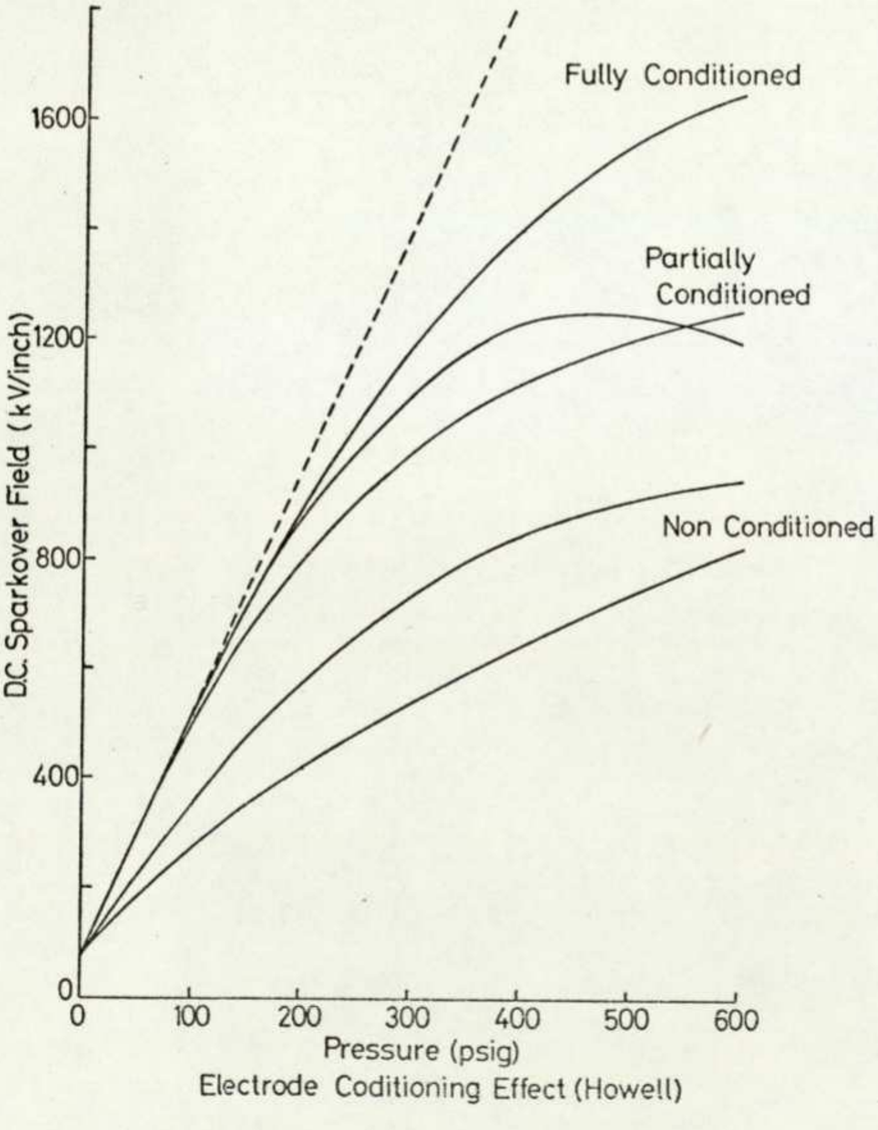

Electrode Coditioning Effect (Howell)

Fig 3.16

Several authors have considered quantitatively the effect of conditioning on the V_s verses pressure curve for a gap. Howell(1939) plotted these curves for rough, partially conditioned and fully conditioned electrodes, these results are given in figure 3.16. It can be seen that the more conditioned the electrodes the better the shape of the curve for use as a LTSG. Other workers,eg. Trump(1950), have pointed out that conditioning can be optimized, that is, if the conditioning discharges are applied beyond a certain stage the electrodes can behave as if they were becoming rougher. A further complication occurs with the LTSG due to the craters that are produced by the incident laser energy on one of the electrodes. The effect becomes evident if the electrodes are conditioned using an applied overvoltage and the gap is then operated as a LTSG the shape of the V_s verses pressure curve can change drastically, the conditioning of the LTSG should be undertaken using the laser radiation to produce the overvoltage. The results of conditioning using this technique can never be better than those obtained using normal overvoltage conditioning. This problem can be overcome by using a LTSG which ionizes the gas to produce the initiating electrons (this was discussed previously), with the disadvantage that higher levels of radiation are required to ionize the gas than are required to ionize the electrode material. In figure 3.16 the partially conditioned curve which has a peak is a fine example of misleading results due to experimental procedure, this curve was plotted with pressure decreasing and the gap was being conditioned more with each pulse, that is, at high pressures the gap was not well conditioned and at low pressures it was well conditioned.

Electrode shape and polarity.

The effect of the electrode shape on the self breakdown voltage verses pressure curve has been discussed in detail by Zeier(1932) for both air and nitrogen. Results for nitrogen only will be considered here. Zeier gives

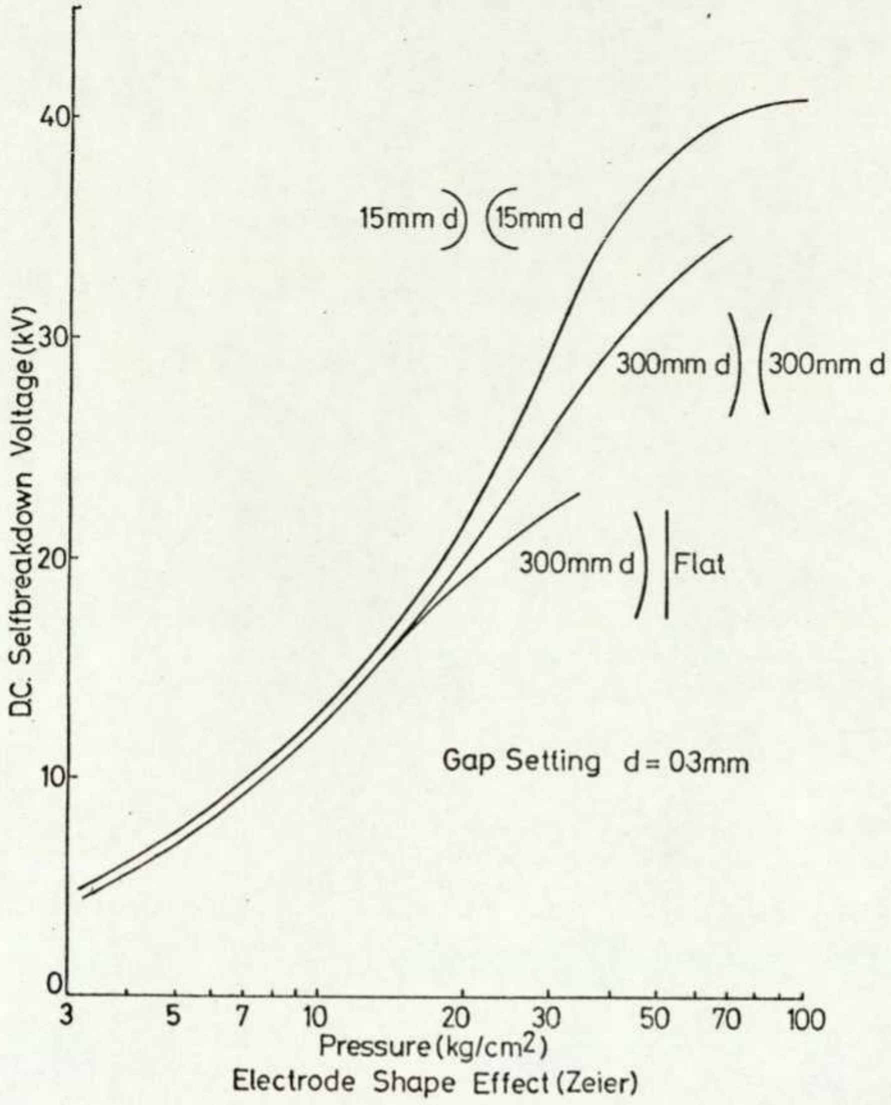

Electrode Shape Effect (Zeier)

Fig 3.17

results using several gap widths of self breakdown voltage verses pressure gap width product for a) two 15mm spherical electrodes b) two 300mm spherical electrodes and c) one 300mm spherical electrode and a plane electrode. Figure 3.17 gives the self breakdown voltage verses pressure for the three electrode configurations given above. The horizontal scale of pressure gap width product has been changed to pressure only by dividing by the gap width so that this curve can be compared with the others in this section. The surprising result implied by these curves is that as the electrode diameter reduces the arrangement becomes more suitable for LTSG operation, in that the curves follow Paschens law to a higher pressure as the electrode diameter falls. In the arrangement used in this work there will be a limiting value of electrode size determined by the hole through which the ionizing beam passes. A second advantage of using electrodes of very small physical size comes from the effect of streamer growth mentioned earlier, if the electrodes are small the inductance introduced by the discharge streamer will become smaller at an earlier stage since its diameter grows at a constant rate, this should lead to a faster minimum risetime. Zeier also considers the effect of polarity on a spherical electrode configuration. Figure 3.18 summerizes his results and suggests that the smaller electrode should always be made positive to achieve the best fit to Paschens law at a high pressure.

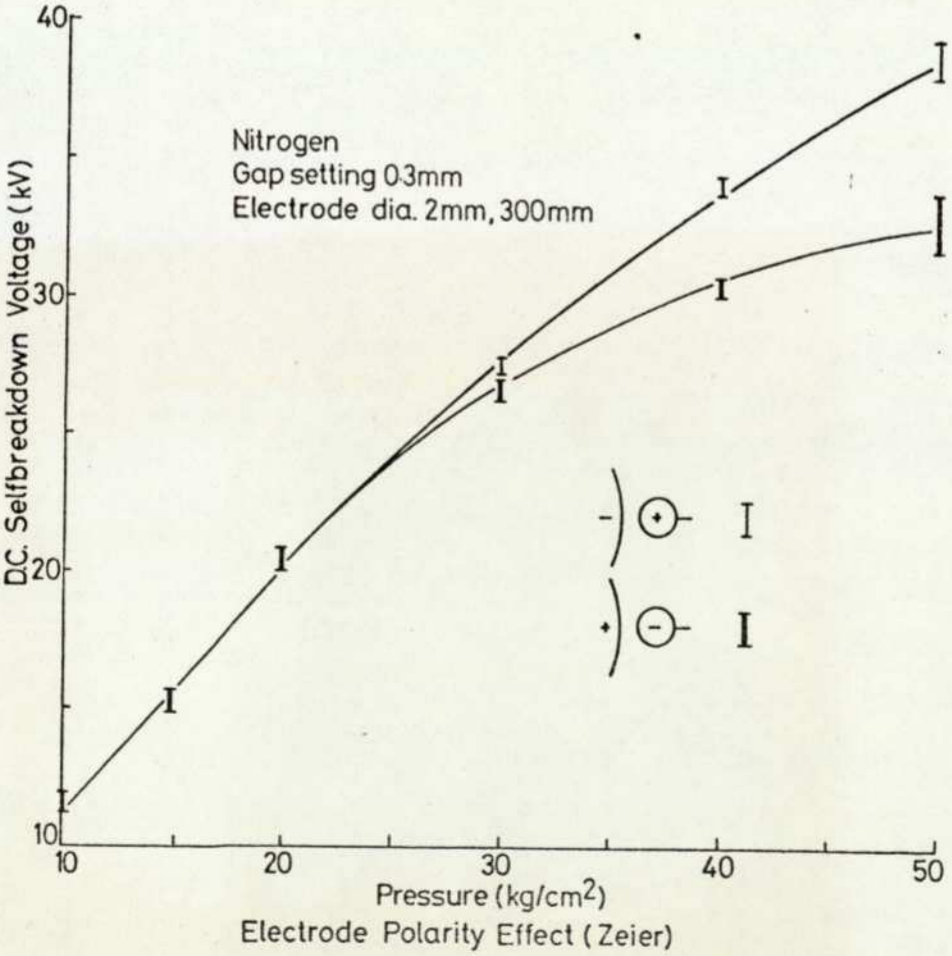

Electrode Polarity Effect (Zeier)

Fig 3.18

Laser triggered spark gap performance.

The laser triggered spark gaps were tested to determine their reliability and jitter characteristics as a pockels cell driver. An arrangement using the two terminal LTSG and a four terminal pockels cell was investigated firstly for its control of triggering level and secondly for the jitter between the firing time and the Q-switch pulse which triggers the LTSG.

A series of pulses was used to trigger the gap, each pulse being reduced in magnitude before entering the LTSG by a polarizing attenuator. Figure 3.20 shows the effect this produced on the output pulse. Breakthrough light representing the unswitched Q-switch pulse was purposely introduced so that the relative time at which the LTSG operates can be judged. The nine pulses were taken at one minute intervals. The control over the switching position as a function of the power entering the LTSG can be seen as the gradual movement of the switched pulse towards the trailing edge of the Q-switched pulse. The overall power output jitter was very small from pulse to pulse for a fixed input attenuation, this was attributed to a certain amount of self regulating that occurs to account for small changes in laser power.

This happens due to the fact that the trigger power for the LTSG is relatively constant as long as the physical conditions under which the spark gap operates are not changed. Then the power in the trigger pulse at the instant of switching determines directly the power that is passed by the pockels cell to produce the output pulse. If the LTSG is made to trigger at the position in the Q-switch pulse where the maximum gradient $\frac{dP}{dt}$ occurs (where P is the power) the jitter can be reduced even further.

The optimum condition for operating the LTSG and pockels cell combination appear to be; by attenuation arrange for the LTSG to switch at the greatest positive rate of change of power in the Q-switch pulse, delay the

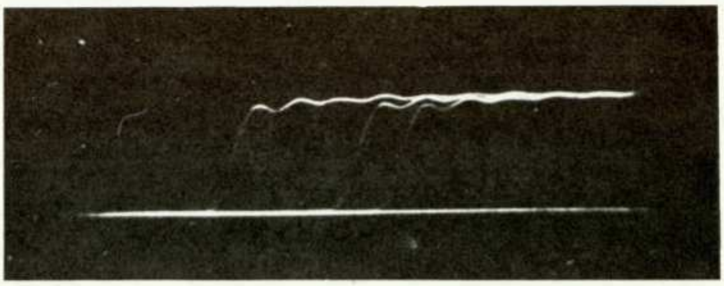

Fig 3.19 LTSG Current Pulses

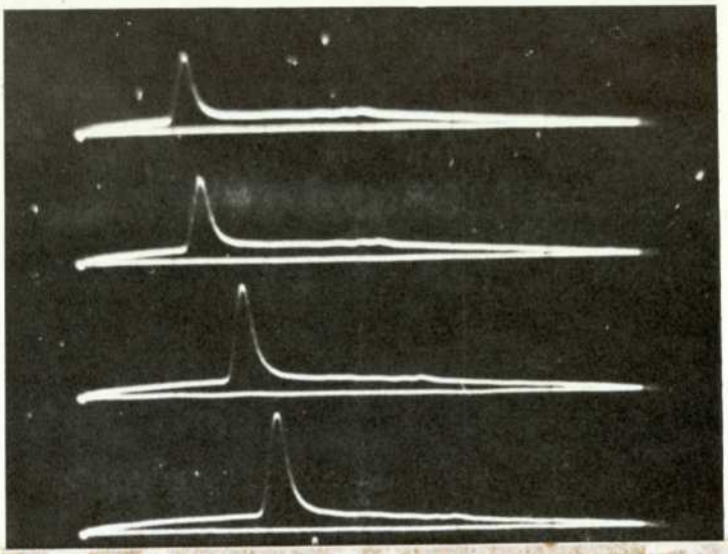

Fig 3.20 LTSG Delay Control

7r

Fig 3.20 LTSG Delay Control

voltage step produced by the LTSG by a time equal to the time between the maximum $\frac{dP}{dt}$ and zero $\frac{dP}{dt}$ (peak of the Q-switch pulse). This applies the voltage step to the pockels cell at a time when the optical power is relatively constant and hence any time jitter present will not show up as a power output jitter.

3.8 The laser amplifier.

The oscillator used by the author for the damage measurements had an output power of several megawatts. The trend of the variation of power density for damage threshold verses pulse length indicated initially that powers several times greater than those obtained with the oscillator would be needed in the 1ns region, and even higher in the picosecond region.

Since the oscillator power could only be increased at the expense of stability it was necessary to build an amplifier capable of producing the higher power single mode output needed for reproduceable high power densities.

The design critera for a simple travelling wave laser amplifier will now be discussed together with the results of the actual amplifier constructed.

If light passes through a medium with single pass gain G_o there will be a fraction of the energy reflected (r) at the entrance and exit surfaces. The energy incident initially (s_i) on the input surface will be divided into two components, $s_i r$ back along its path and $(1-r)s_i$ in the same direction as the incident beam. It can be shown using a geometric series summation that the resulting output divided by the input is

$$G = \frac{G_o(1-r)^2}{(1-rG_o)} \qquad 3.20$$

It is obvious from 3.20 that the amplifier will become unstable if $G_o r$ is greater than unity, this imposes a limit on the gain G_0 (and hence length) of the active medium for a given reflection coefficient at its surfaces. By using Brewster windows to terminate each end of the active medium very low values of r can be achieved, leaving the overall gain G approximately equal to the single pass gain G_0

The single pass gain and its theoretical determination has been discussed by many authors, for example Ross(1969) and Steele(1968). A brief discussion follows so that the practical design critera can be established and used to determine the efficiency and operating characteristics of the completed system.

As was done in section 3.3 the ruby can be approximated by a two level system if one of the two possible transitions is fast compared to the other. Figure 3.21 shows the energy level model of a two level laser material. n_1 and n_2 are the electron densities in each level and Φ is photon density moving with velocity c. The total photon flux $c\Phi$ interacts with the effective cross-sectional area of the energy lattice σ which produces stimulated emission of a photon. It can be shown that the photon density at any point x in the two level medium at time t can be expressed as

$$\frac{d\Phi}{dt} = -c\frac{d\Phi}{dx} + \sigma c\Phi(n_2 - n_1) \qquad 3.21$$

The rate equations for the electron densities are given as

$$\frac{dn_1}{dt} = \sigma c\Phi(n_2 - n_1) \qquad 3.22$$

and

$$\frac{dn_2}{dt} = -\sigma c\Phi(n_2 - n_1) \qquad 3.23$$

The number of electrons N in the system is constant, this can be written as

$$N = n_1 + n_2 \qquad 3.24$$

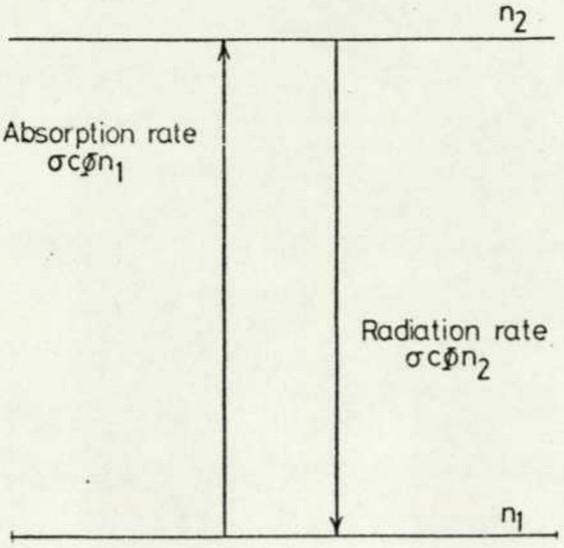

Two level energy model.

Fig 3·21

If η is defined as the proportion of population inverted t then

$$\eta = \frac{n_1 - n_2}{N}$$

and φ is defined as twice the total photon flux per atom

$$\varphi = \frac{2\Phi}{N}$$

substituting these expressions into equations 3.21, 3.22 and 3.23

$$\frac{d\varphi}{dt} = -c\frac{d\varphi}{dx} + N\sigma c\varphi\eta \qquad 3.25$$

and subtracting 3.22 from 3.23

$$\frac{d}{dt}(n_2 - n_1) = -2\sigma c\Phi(n_2 - n_1)$$

$$\frac{d\eta}{dt} = -2\sigma c\Phi\eta$$

$$= -N\sigma c\varphi\eta \qquad 3.26$$

Using equations 3.25 and 3.26 as well as the boundry conditions for the laser amplifier, solutions can be obtained to give φ and η at any point in the amplifier length L at any time t after the pulse enters the amplifier. These solutions are;

$$\eta(x,t) = \frac{\eta_o(x)\ \exp(-N\sigma\int_o^x \eta_o(x^*)dx^*)}{\exp(N\sigma c\int_{-\infty}^{t-\frac{x}{c}} \varphi_o(t^*)dt^*)\exp(-N\sigma\int_o^x \eta_o(x^*)dx^*)-1} \qquad 3.27$$

and

$$\varphi(x,t) = \frac{\varphi_o(t-\frac{x}{c})}{1-(1-\exp(-N\sigma\int_o^x \eta_o(x^*)dx^*))\exp(-N\sigma c\int_{-\infty}^{t-\frac{x}{c}} \varphi_o(t^*)dt^*)} \qquad 3.28$$

Equations 3.27 and 3.28 are solutions to the inversion fraction and photon density as a function of time and distance along the rod. η_o and φ_o are the initial inversion fraction and photon density respectively and x^* and t^* are dummy variables.

As a simplification the input to the amplifier may be considered to be square with photon density Φ_o and duration τ_o. Using this input to set the values of $\Phi_o(0,t)$, the integral in the second exponential term in equation 3.28 becomes $\frac{2\Phi_o}{N}(t-\frac{x}{c})$ and the integral in the first exponential term becomes $\eta_o x$, since the pumping is uniform along the length of the amplifier(no hot spots).

To obtain the gain, the intensity I is defined as

$$I = \Phi c \qquad 3.29$$

and the gain G_o as

$$G_o = \frac{I(L,t)}{I_o} \qquad 3.30$$

for a rod of length L. Substuting $\varphi(L,t)$ from 3.28 into 3.29

$$I(L,t) = \frac{I_o}{1-(1-\exp(-\sigma\eta_o NL))\exp(-2\sigma I_o(t-\frac{L}{c}))}$$

and is valid for the duration of the pulse only. This produces a gain G_o of

$$G_o = \frac{1}{1-(1-\exp(-\sigma\eta_o NL))\exp(-2\sigma I_o(t-\frac{L}{c}))} \qquad 3.31$$

The gain for a very short pulse where the rod does not have time to reduce the stored energy appreciably at a given point, $(t-\frac{L}{c})$ will be approximately zero leaving the gain as

$$G_o = \exp(\sigma \eta_o NL) \qquad 3.32$$

If the pulse is long and a reduction of inverted energy is appreciable during the pulses presence at a given point in the amplifier, the gain reduces exponentially for any section of the amplifier. This results in a pulse that has a maximum at its leading edge and drops off towards the trailing edge.

Figure 3.22 shows a plot of gain verses the

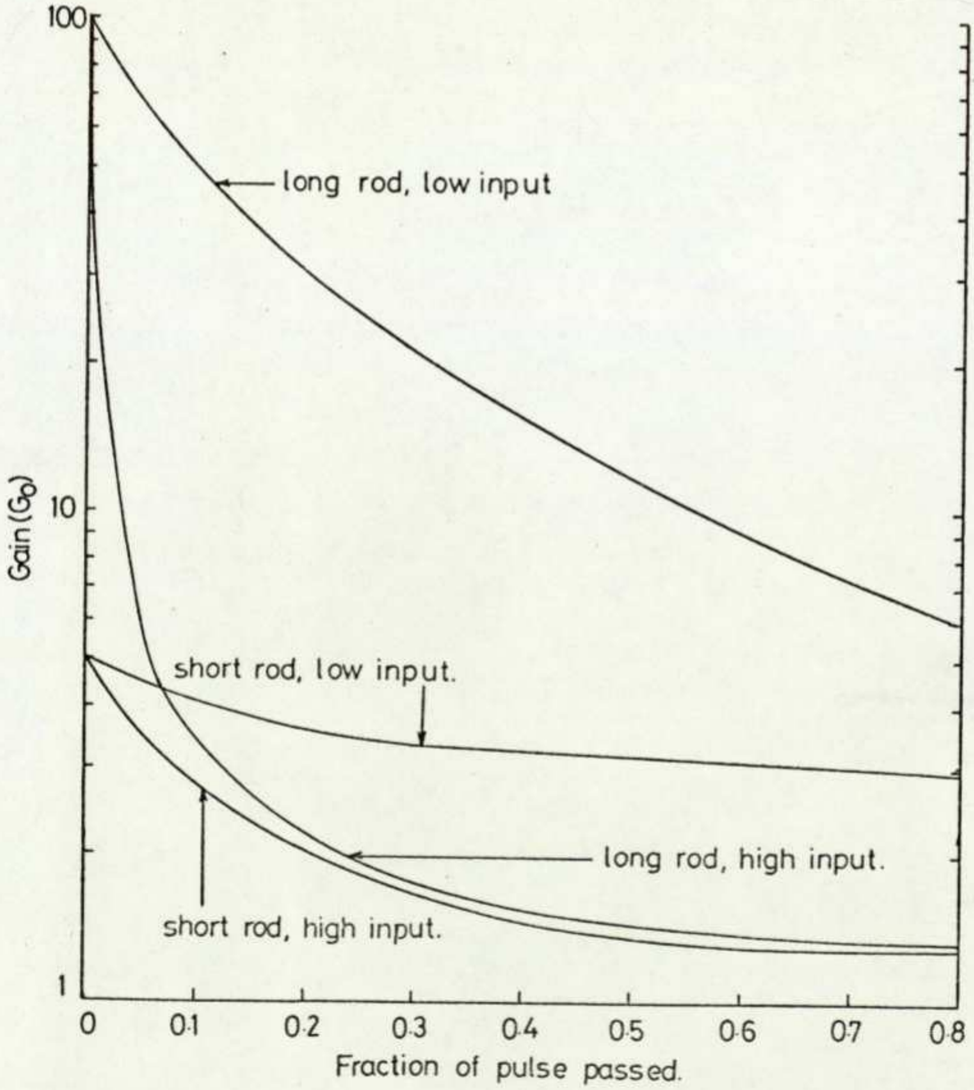

Fig 3·22

fraction of pulse that has passed a given point after leaving the amplifier. This shows the shortening effect that an amplifier can produce if the input power is high enough and long enough.

Since the input pulse to a laser amplifier is usually gaussian with time the shortening effect is not readily apparent. To make use of the effect in a practical arrangement the gaussian pulse can be chopped to produce a sharp leading edge at the peak of the gaussian distribution. The sharp edge will saturate the rod in a very short time producing very little output for the duration of the pulse. This results in a very short pulse being generated.

The design parameters will now be considered for a ruby laser amplifier to give a power gain of approximately five.

Since the input pulses will be in the order of 1ns long with a peak power of several megawatts the constant inversion condition can be considered giving the overall gain in equation 3.32.

Airtron(1969) give the percentage doping of Cr_2O_3 in the ruby used as 0.05% and the Cr^{+3} concentration N as 1.58×10^{19} ions cm^{-3}.

The constant of absorption $\alpha = \sigma N$ has been measured by Maiman(1961) as 0.4 cm^{-1} for the 0.6943 μm (R_1) line. By substitution

$$\sigma = \frac{\alpha}{N}$$

$$= 2.53 \times 10^{-20}$$

Due to flash tube inefficiencies and overall losses the inversion percentage was taken as 50%. If laseing only occurs as a result of the (R_1) transition N is taken as $\frac{1}{2}(N_{R_1} + N_{R_2})$. To find the length of rod needed to give a gain of 5 equation 3.32 is rearranged to give

$$L = \frac{\ln G}{\sigma \eta_0 N}$$

$$= 16.1 \text{ cm}$$

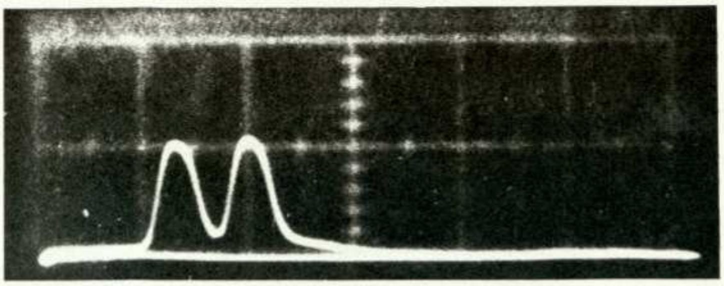

Fig 3.24 Amplifier Gain

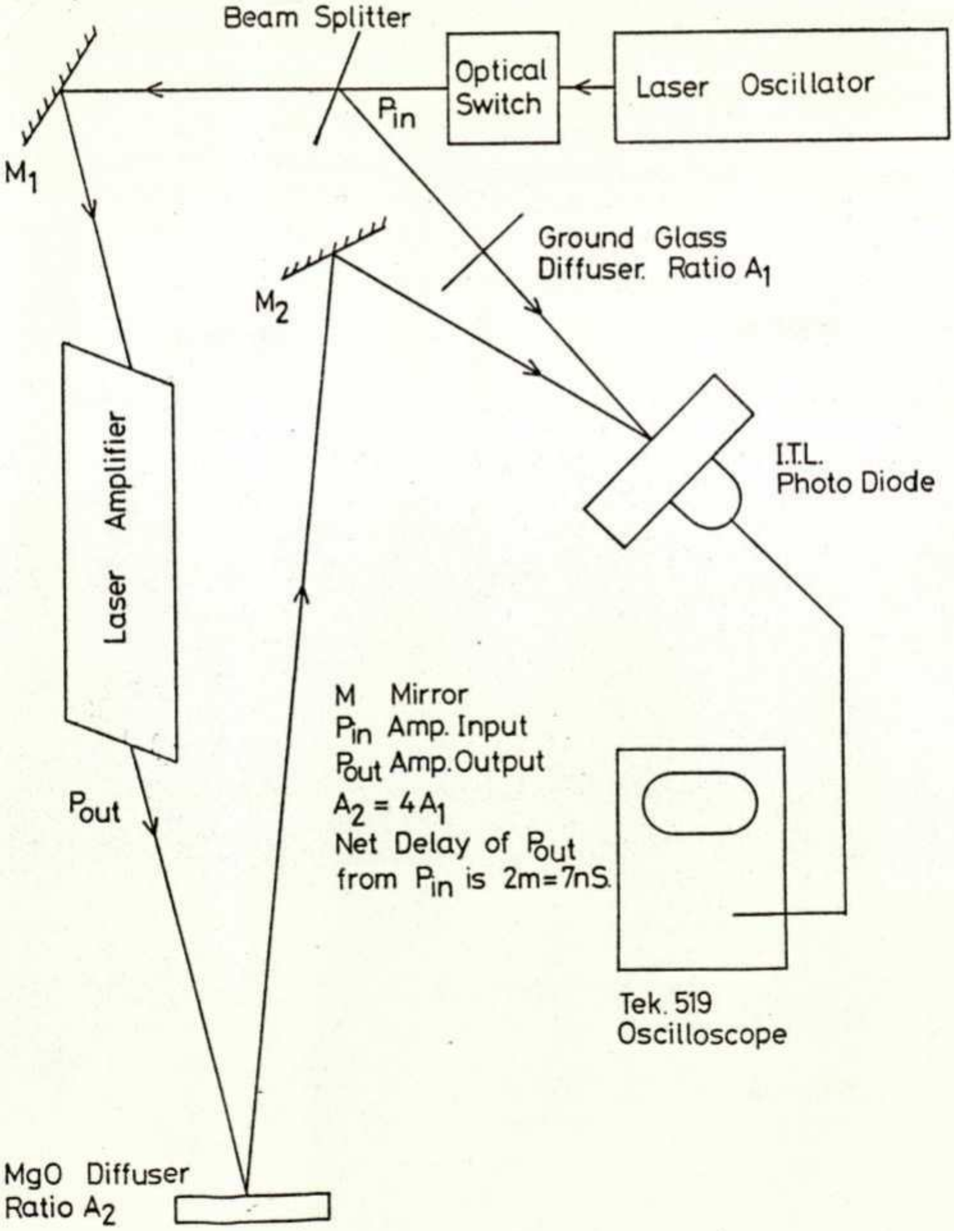

Layout for Amplifier Gain Measurement (G_o)

Fig 3.23

The amplifier was built using a rod of 20cm length with a radius of 5mm to accommodate the input beam of diameter 0.6cm.

Appendix 1 contains the workshop drawing of the amplifier head, using a helical flashlamp
The electronics to drive the flash tube was a duplication of the oscillator electronics but uprated to produce 21 kilojoules at 10 kilovolts.

The result of the amplifier performance is shown in figure 3.24 this photograph was taken using the layout in figure 3.23. The first pulse is that of the input to the amplifier and the second pulse is the amplifier output. The fact that the pulse shapes are almost identical confirms the initial assumptions concerning the lack of saturation effects at this pulse length.

Both the input and output pulse were attenuated before being imaged onto the detector, the ratio of output power to input power was arranged to be 4.0. From the peak powers indicated in figure 3.24 it is obvious that the gain of the amplifier was 4.0. This gain was produced with an input energy of 6 kilojoules. Increasing the input energy produced a considerable increase in gain.

SECTION

4

POCKELS CELL DESIGN

Introduction.

The design of present day commercial pockels cells is considered and the limitations of their risetime capabilities are discussed

A pockels cell design based on a stripline construction is investigated, and the difficulties arising from this type of geometry are discussed.

A combination of coaxial and stripline construction is used in the final design for a pockels cell with very fast response. The step response of this pockels cell is given together with the shortest pulse it can produce.

It is believed that the pockels cell described in this section has a better electrical response than others described in the published literature.

4.1 Present designs.

In section 3 it was shown that to achieve fast switching of a pockels cell the switching voltage must be applied to the crystal with no degradation to its risetime as it passes across the crystal. The voltage must be applied to the longitudinal modulator such that the field is constant along the light path but the voltage is constant across the aperture.

The fact that these requirements are not fulfiled by most commercial pockels cells is the reason why the best optical risetime reported in the literature is 400ps (Ireland(1975)).

If the step voltage is applied to the crystal via a coaxial cable which is the usual practice, the problem arises in matching the electrical impedance of the electrode crystal combination to the characteristic impedance of the cable. Any mismatch in impedance will degrade the risetime at the electrodes of the crystal. It can be seen that the limitation of the optical risetime is purely a function of the interface between electrodes and cable assuming the voltage step in the cable is ideal, the transit time of the step across the aperture is neglected and the crystal is short compared to the length of the minimum pulse length (within the crystal).

The linearity of the field within the crystal is a function of the crystal and electrode physical arrangements. In general the larger the area of the electrodes compared to the aperture area and length of the crystal the more linear will be the field. As the electrode area increases so the electrical capacitance increases which degrades the applied voltage. Thus there must be a trade off between linearity of field and applied voltage risetime.

The optimization of electrode arrangements to give the best voltage gradient in the crystal for various values of electrode capacitance has been discussed in detail by Steinmetz(1973). Their calculations giving the field non-uniformity as a function of electrode width and separation will be used in a later section to calculate the field non-uniformity existing in the newly designed pockels cell.

A typical modern commercial pockels cell such as the Electro-Optic Developments PC105 which was used for the initial long pulse length damage investigation consists of a coaxial terminal (high voltage BNC) connected to the cylindrical ring electrodes by a small length of wire, the length of this wire represents a characteristic impedance different from that of the connector. As well as this the electrode capacitance forms a characteristic impedance which is very low, due to the high dielectric constant of KD*P and other physical restraints.

Tests were carried out on the PC105 pockels cell using a time domain reflectometer having a 180ps risetime. The results are shown in figure 4.1. It is clear that a reflection coefficient of greater than 0.2 is present. The higher impedance of the connecting lead and the lower impedance of the crystal electrodes are visible. The same time domain reflectometer can be connected in such a manner as to show the degradation of the applied step voltage. This is the actual risetime that is being applied to the crystal. Figure 4.1 b) shows both the input and output voltage, the electrical risetime after deconvolution is 430ps. This figure varifies the best optical pulse that could be obtained with this pockels cell of approximately 800ps. It is clear from these observations that a better electrical match at the crystal should be achieved which would give a corresponding reduction in electrical and hence optical risetime.

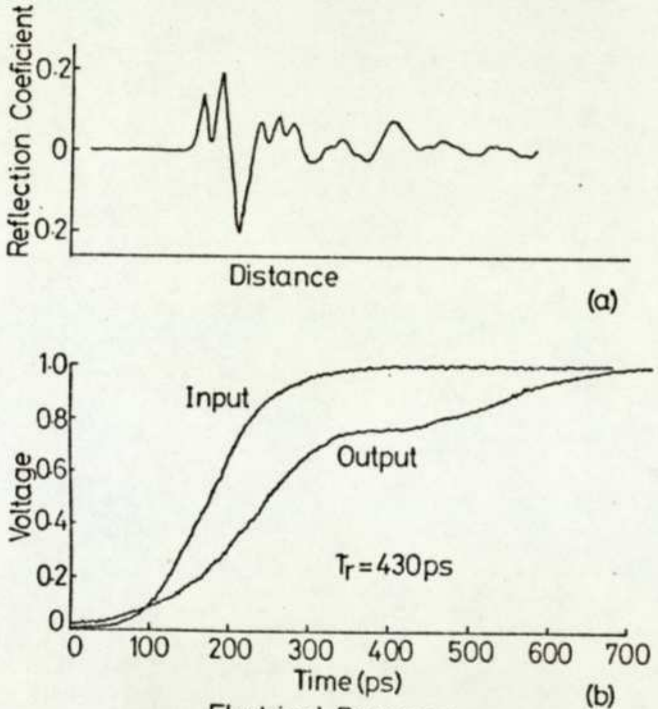

Electrical Response of EOD PC105 Pockels Cell

Fig 4.1

4.2 Strip line theory.

If the electro-optic crystal could be built into a matched strip line configuration the electrical degradation at the crystal would be negligable, resulting in a very fast electrical risetime.

A summery of the properties of ADP and KD*P is given in table 4.1. The material which will be used as the optical element in the pockels cell is KD*P because of its lower half wave voltage (3.6kV compared with 12kV for the half wave voltage of ADP at 0.69 microns). The dielectric constant of interest is ϵ_z since the applied field will be in this direction.

KD*P is many times more expensive than ADP so the fact that ϵ_x for ADP is approximately equal to ϵ_z for KD*P is very fortunate. For preliminary electrical tests ADP cut in the x direction was used in place of KD*P at a considerable saving in cost.

From table 4.1 it can be seen that both materials are very consistant having negligable dispersion up to 10^8 Hz and very small loss angles, indicating good high frequency performance.

Basic strip line theory will now be discussed to show the vital limitations inherent when using ADP and KD*P as dielectrics in this geometry.

The characteristic impedance of a stripline arrangement as a function of its physical dimensions has been discussed by many authors, for example Gunstone (1970). The arrangement best suited for this application is called microstrip and consists of a ground plane and

	KD•P				ADP			
f (Hz)	$\epsilon_{(a)}$	$\epsilon_{(c)}$	$\tan\delta_{(a)}$	$\tan\delta_{(c)}$	$\epsilon_{(a)}$	$\epsilon_{(c)}$	$\tan\delta_{(a)}$	$\tan\delta_{(c)}$
10^1	51	57		0.42				
10^2					55.9	14.7	0.04	0.24
10^6					55.9	14.3	0.0005	0.006
10^8					55.9	14.3	<0.001	0.005
10^{10}	50	56	0.01	0.03		13.7		0.005

Electrical Properties of KD•P and ADP

Table 4.1

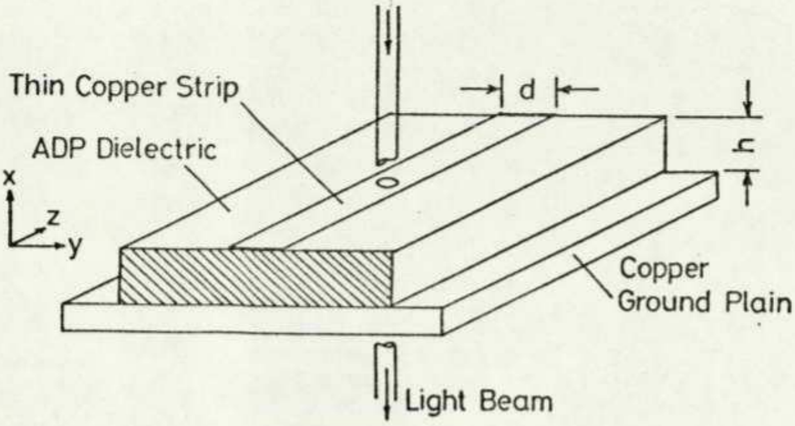

Theoretical Strip Line Pockels Cell
Fig 4.2

strip conductor separated by a dielectric material. Figure 4.2 shows this stripline arrangement in the form of a z cut longitudinal modulator.

The general equation for the characteristic impedance as a function of the strip width to height ratio is

$$Z_o = \frac{376.7}{2\sqrt{K}}\left(\frac{d}{2h}+0.441+0.082\left(\frac{K-1}{K^2}\right)+\left(\frac{K+1}{2\pi K}\right)\left(1.451+\ln\left(\frac{d}{2h}+0.94\right)\right)\right)^{-1} \quad 4.1\ a)$$

for d/h>1, and

$$Z_o = \frac{376.7}{\pi\sqrt{2}\sqrt{K+1}}\left(\ln\left(\frac{8h}{d}\right)+\frac{1}{32}\left(\frac{d}{h}\right)^2-\frac{1}{2}\left(\frac{K-1}{K+1}\right)\left(\ln\left(\frac{\pi}{2}\right)+\frac{1}{K}\ln\left(\frac{4}{\pi}\right)\right)\right) \quad 4.1\ b)$$

for d/h < 1, where Z_o is the characteristic impedance, h is the height of the strip above the ground plane, d is the width of the strip and K is the dielectric constant of the insulating material.

The dielectric constant of KD*P with voltage applied along its optic axis is 56. The value of d/h from equation 4.1 b) needed to produce a characteristic impedance of 50ohms with this dielectric is 0.133. The aspect ratio of a pockels cell is the ratio of aperture to the crystal length, and is usually no greater than 0.5. This is determined by the minimum field nonlinearity which

which can be tolerated within the crystal. In the strip line arrangement in figure 4.2 it is obvious that the maximium aperture is limited by the strip width. There are absolute limitations on d and h which prevent the ratio d/h from being much less than 0.5. The minimum value of d determined by the minimum aperture is approximately 5 mm, since a smaller aperture is not practical for most applications. The maximum value of h is determined by the electrical cutoff frequency in the strip line and the optical risetime given by the length of light within the crystal. A length h of 10mm limits the minimum risetime to 50ps.

The conclusion from the above discussion is that the ratio d/h is limited to approximately 0.5 by pockels cell considerations. The ratio of 0.133 from the strip line considerations can be increased by altering the remaining two independant variables in equation 4.1 b). Firstly, if a different electro-optic material was used, for example ADP as a z cut modulator, the ratio would be higher due to the lower dielectric constant. This would result in an unexceptably high half wave voltage. Secondly the impedance could be reduced, a reduction by a factor of two would increase the ratio considerably.

This lower impedance would necessitate the use of a 25ohm voltage source. If this voltage source was assumed to be a LTSG, the risetime would increase as the impedance decreased, this was shown in equation 3.17. This prediction does appear to be open to question, but an interpretation of the results presented may be that the inherent inductance L of the spark gap limits the risetime. This risetime is given by the expression L/R and as R is reduced, that is, the characteristic impedance is reduced the risetime increases.

For this application of the strip line it had to be accepted that the d/h ratio of exactly 0.5 was not practically attainable. For this reason an approximation to the strip line arrangement was used, this will be discussed in a following section.

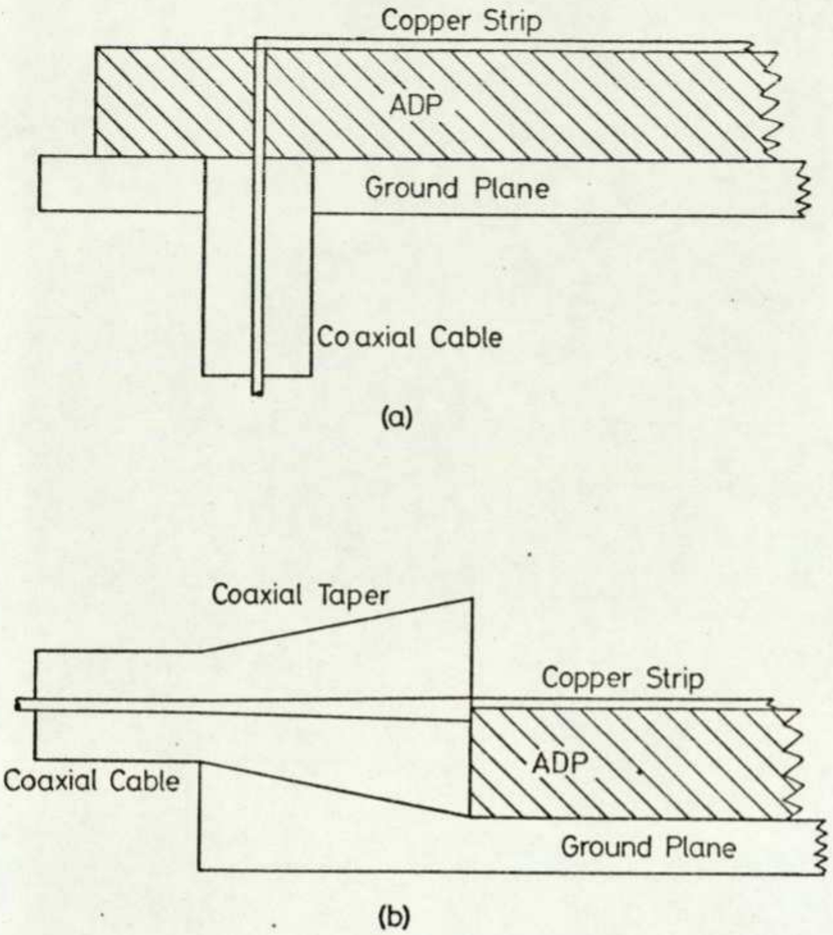

(a)

(b)

Coaxial to Strip Line Conversion
Fig 4.3

A major problem in the use of a strip line element in a largly coaxial system is the coaxial to strip line conversion. Figure 4.3 illustrates two common methods of achieving this transfer of electric and magnetic field pattern. Neither gives a perfect match but b) was chosen as it gives a more gradual change for large strip heights.

The minimum height of the strip line is determined by the minimum crystal length that can be used. This is approximately 1cm since it has been found experimentally (Ley(1977)) that this length of crystal can breakdown electrically with the application of voltages much above 8kV.

4.3 High frequency properties.

The first practical test consisted of building a long strip line of 50ohm characteristic impedance and checking its electrical performance. The line was 20cm long with a strip height of 16mm and strip width of 2.1mm using x cut ADP to simulate z cut KD*P.

The completed line was tested on the time domain reflectometer. Figure 4.4 a) shows the reflection coefficient from a 50ohm source, the impedance match was good indicating that the line dimensions were correct and the coaxial to strip line connectors functioned well. The step function response of the line is given in figure 4.4 b). Although the reflection coefficient was good the step response was poor with a risetime of 800ps for a 180ps input step voltage.

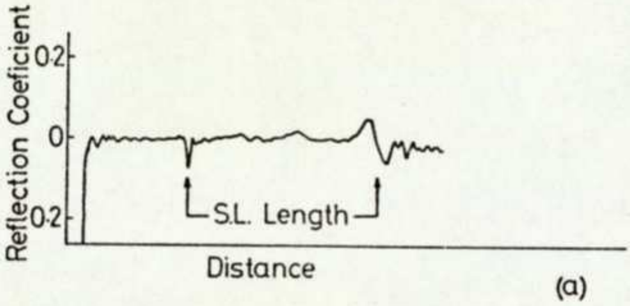

(a)

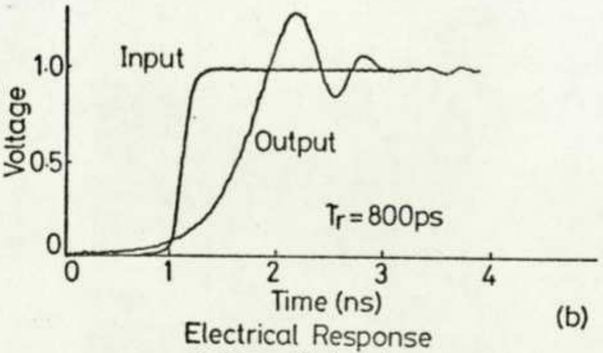

(b)

Electrical Response
of 20cm Strip Line

Fig 4.4

A variable frequency oscillator was connected to the line which was terminated with a 50ohm load. The VSWR was then noted at frequencies up to 2GHz.

Resonance occurred at multiples of 80MHz up to a high limit of 1.2GHz. Above this frequency the VSWR varied erratically. This high limit corresponded to a half wave length in the x direction in ADP of 1.6cm which was the height of the strip line.

A similar line of 2cm length was constructed with all other factors the same as the previous line. The time domain reflectometer reading indicated a good impedance match with the reflection coefficient still less than 0.05 but the step response had improved considerably, giving a risetime of 180ps.

In this case resonance occurred at higher frequency multiples, it can therefore be assumed that the better risetime achieved with this strip line was entirely due to some cutoff frequency related to the length of the line but not associated with the loss angle or dispersion of the dielectric (since both parameters are very small for ADP and KD*P).

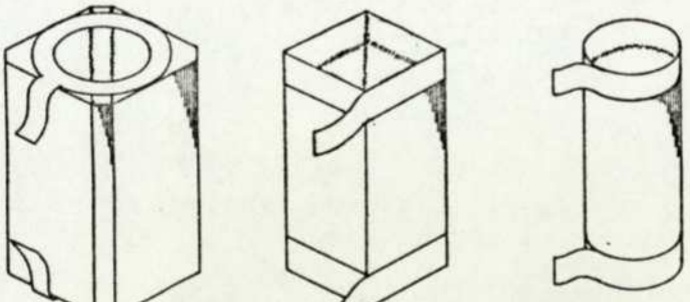

Electrode Arrangements
Fig 4.5

4.4 Electrodes.

Many authors have considered the problem of electric field nonuniformity for different electrode arrangements. The original end plate electrodes shown in figure 4.5 a) were commonly used by manufacturers until Vitkof (1968, 1969) considered the advantages of using ring electrodes shown in figure 4.5 b). He showed that the field nonuniformity for a given electrode area and crystal length was less than in the end electrode case. Steinmetz(1973) later used a cylindrical crystal and electrode arrangement which reduced the area even further. These electrodes, called cylindrical ring electrodes, are shown in figure 4.5 c) and are now used by most pockels cell manufacturers. These are the electrodes that were used in the construction of the new pockels cell.

Steinmetz gave a very useful design curve which specified the field nonuniformity for any cylindrical ring electrode geometry. This figure is reproduced here as figure 4.6.

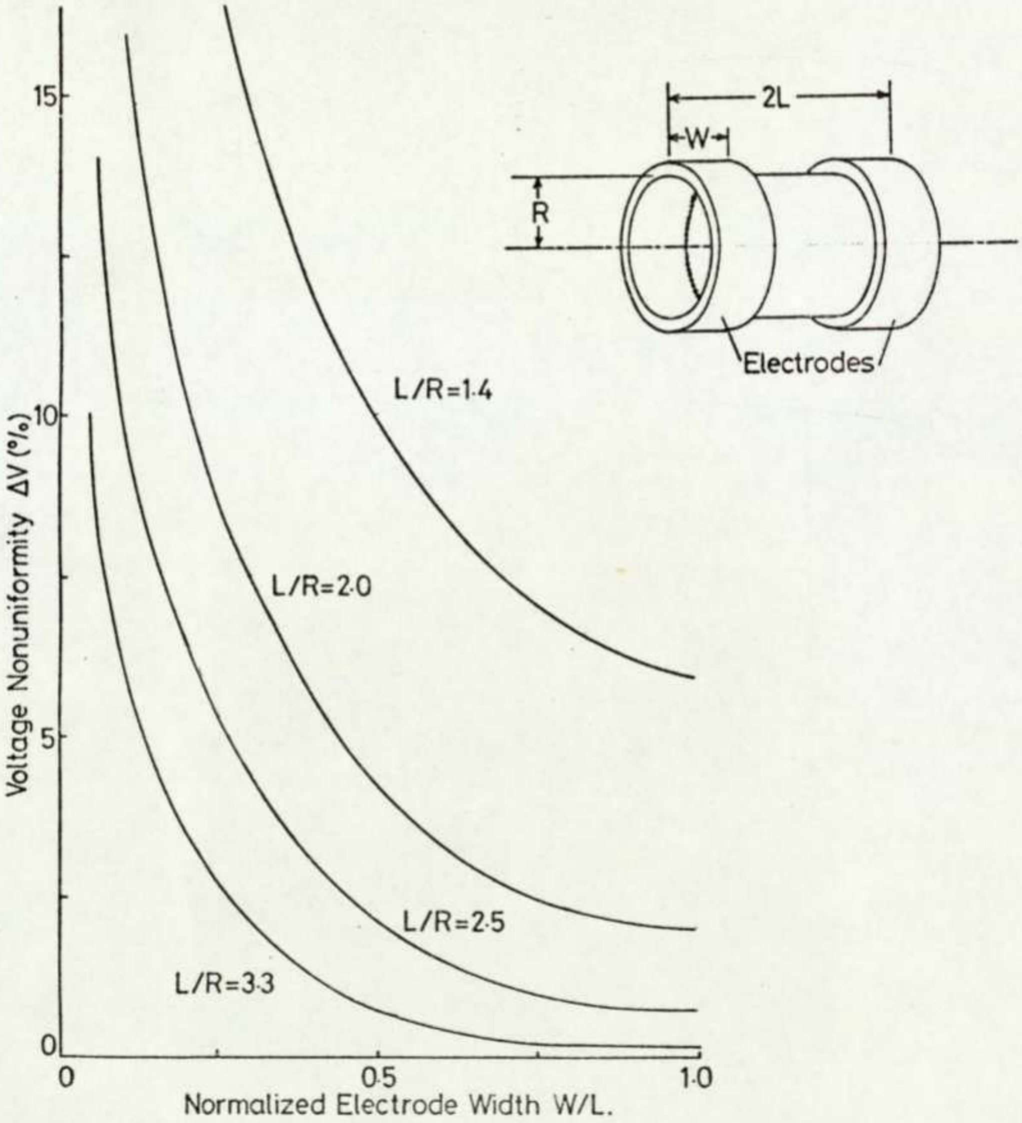

Cylindrical Ring Electrode
Design Curves (Steinmetz et al)

Fig 4.6

4.5 Design.

Since the electrical risetime degradation of the strip line was a function of its length the minimum possible length was used, this being determined by the optical aperture.

The electrode dimensions were chosen by setting an upper limit to the field nonuniformity (this was approximately 2.0% as defined by Steinmetz). An aperture of 5.0mm was chosen earlier, and the crystal length 2L of 16mm was the same as that used in the strip line investigation. From Steinmetz's curves in figure 4.6 it can be seen that the resulting value of the ratio of the ring electrode width W to half the crystal length L is 0.37. This sets the electrode width at 3mm.

If the ratio of inductance per unit length to capacitance per unit length can be kept the same from the true strip line to the pockels cell, the impedance will also be the same.

A calculation of the capacitance per unit length for the strip line results in

$$C_s = 0.10 \text{ pf/mm}$$

The same calculation for the pockels cell results in

$$C_p = 0.18 \text{ pf/mm}$$

There is no simple analytical expression for the inductance of the pockels cell electrodes so its calculation was not attempted. The order of magnitude agreement of the capacitances and the fact that each has the same dielectric separation suggests that the pockels cell arrangement can be approximated to the strip line in terms of impedance. An engineering drawing of the final pockels cell is given in appendix 3 and a photograph of two completed pockels cells mounted for pulse production is given in figure 4.7

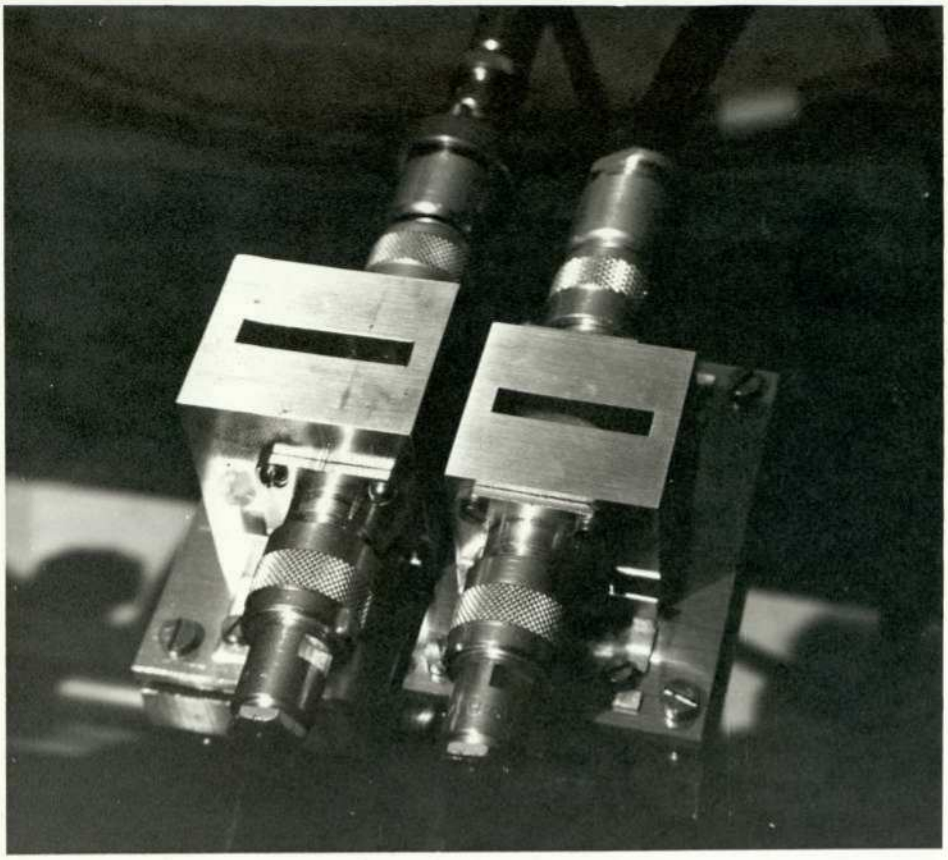

Fig 4.7 The New Pockels Cells

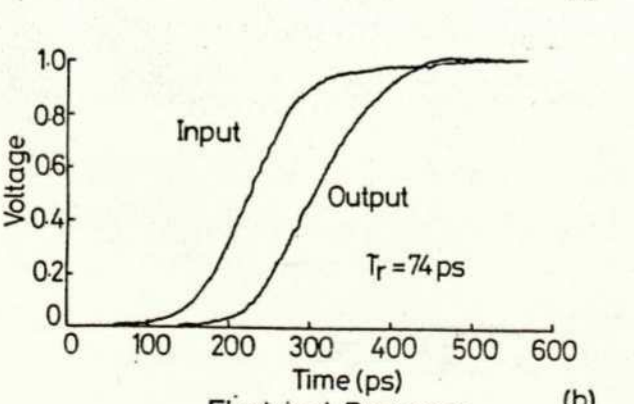

Electrical Response
of the New Pockels Cell

Fig 4.8

4.6 Pockels cell performance.

The completed pockels cell was investigated firstly for its electrical characteristics and secondly for its suitability as an optical switch.

Electrical risetimes were measured on a time domain reflectometer with 180ps risetime. Figure 4.8 a) shows the impedance match and figure 4.8 b) the input and output risetimes of the new pockels cell. The resulting risetime after accounting for the intrinsic system risetime (including connecting leads) was 74ps which is considerably shorter than the risetime of 430ps obtained with the commercial pockels cell.

Operating as an optical switch the new pockels cell had a DC half wave voltage of 3.9kV indicating good electrode contact with the crystal, and a qualitative investigation revealed a good extinction ratio across the complete width of the aperture. This suggests that the design parameters for field uniformity in figure 4.6 were being achieved.

The optical risetime of the pockels cell is given as the streak record in figure 4.9. When the pockels cell was turned off a certain amount of breakthrough light was present (due to diffusion at one surface of the crystal which was not perfectly polished). The fact that this light

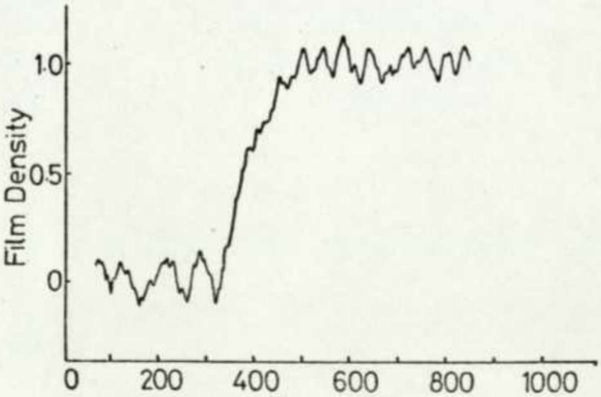

Pockels Cell Respons

Fig4.9

was visible on the streak record and that the light transmitted when the pockels cell switched on was not saturating the film,meant that the camera was resolving the entire dynamic range of the pulse.

The optical risetime in figure 4.9 is approximately 150ps which is considerably better than anything that has been published to date.

Apart from the electrical risetime applied to the crystal in the pockels cell there are two other optical risetime limiting factors. Firstly the length of light present in the crystal at the instant of switching. The time taken for this length of light to pass the exit face of the crystal will be the time required for the intensity to reach its final value, this time t_l is

$$t_l = ln/c \qquad 4.4$$

where l is the crystal length, c is the velocity of light and n is the refractive index of the crystal. For the pockels cell built by the author this time was approximately 60ps.

Secondly the finite aperture of the pockels cell means that the electrical pulse will take a time t_α to travel across the aperture. This time can be expressed in terms of the velocity of the pulse in the effective strip line, then

$$t_\alpha = \nu d/c$$

where ν is the velocity ratio in the strip line and d is the aperture diameter. This time for the pockels cell built by the author was approximately 90ps. The convolved sum of these two risetimes indicate that the actual risetime is very close to the theoretical limit.

If a very large aperture low impedance pockels cell was built the transit time across the aperture t_α could severely limit the optical risetime. This could be overcome by considering a method of correcting the spatially varying time delay. Depending on the electrode

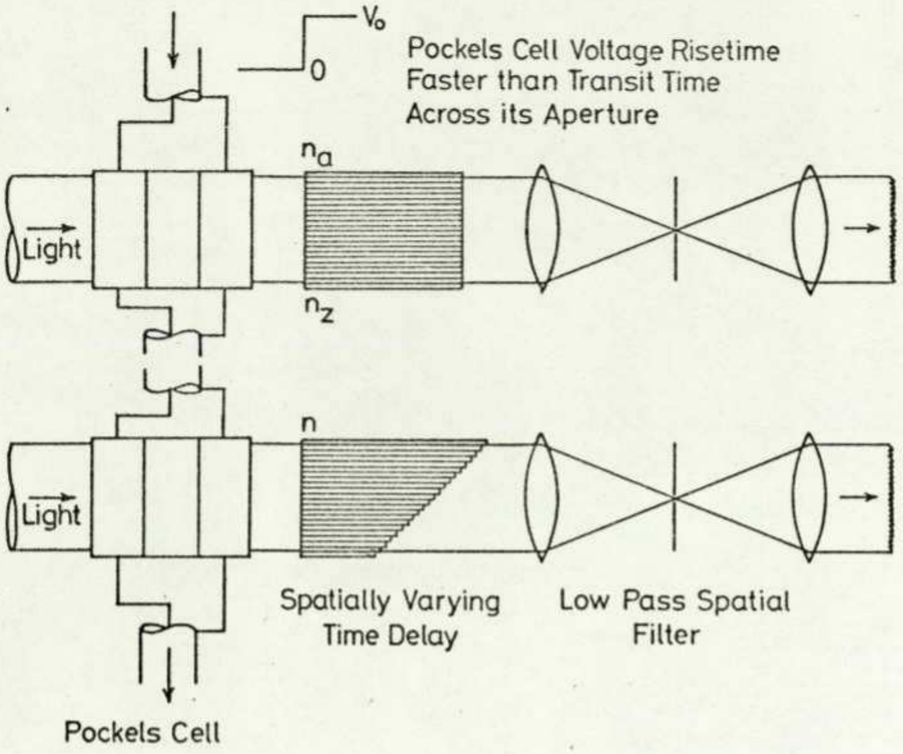

Pockels Cell Aperture Compensation

Fig 4.10

arrangement the spatial delay could vary linearly with distance across the aperture (transparent conducting end plate electrodes) or nonlinearly (in the case of cylindrical ring electrodes). By performing spatial streaks with a streak camera in orthogonal directions across the beam it would be possible to determine the value of delay needed for each section of the beam. This could then be corrected by one of two proposed methods, both relying on splitting up the beam and delaying each part separately. The size of the integral sections can be chosen to give the required accuracy. If a large number of sections is used diffraction effects could become excessive, the larger the integral sections the greater will be the energy passed by the low pass spatial filter.

Figure 4.10 illustrates two methods of performing the integral spatial delay a) using a bundle of glass fibres of different refractive index, the value of which is chosen to perform the required delay, and b) a bundle of constant valued refractive index optical fibres of various lengths chosen to give the required delay. In each system the fibres could be replaced by discrete sections of glass allowing coarser correction and hence lower diffraction losses. Both systems would be followed by a low pass spatial filter to reduce the high frequency components introduced by splitting the beam into sections. In theory this technique could reduce considerably the effect of the finite aperture size, and the resulting optical risetime would be dependant only upon the electrical risetime and the length of the crystal.

Due to the relatively long risetimes used in this work it was not considered warranted that a practical investigation of the above system should be undertaken.

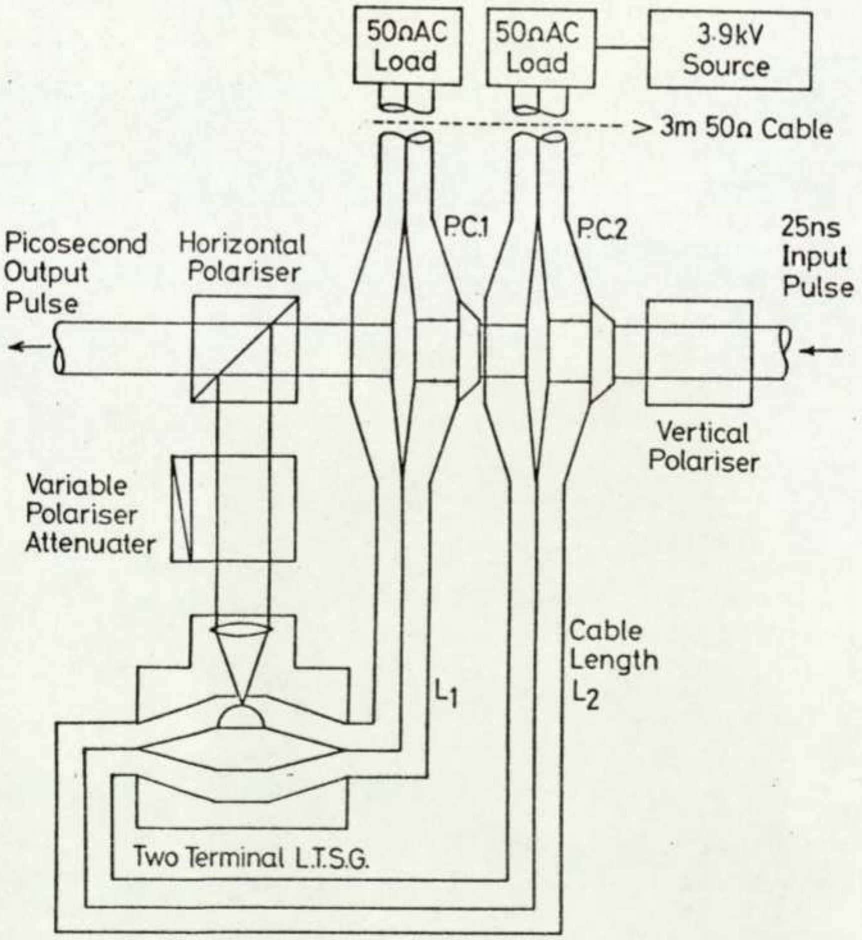

Picosecond Pulse Production

Fig4.11

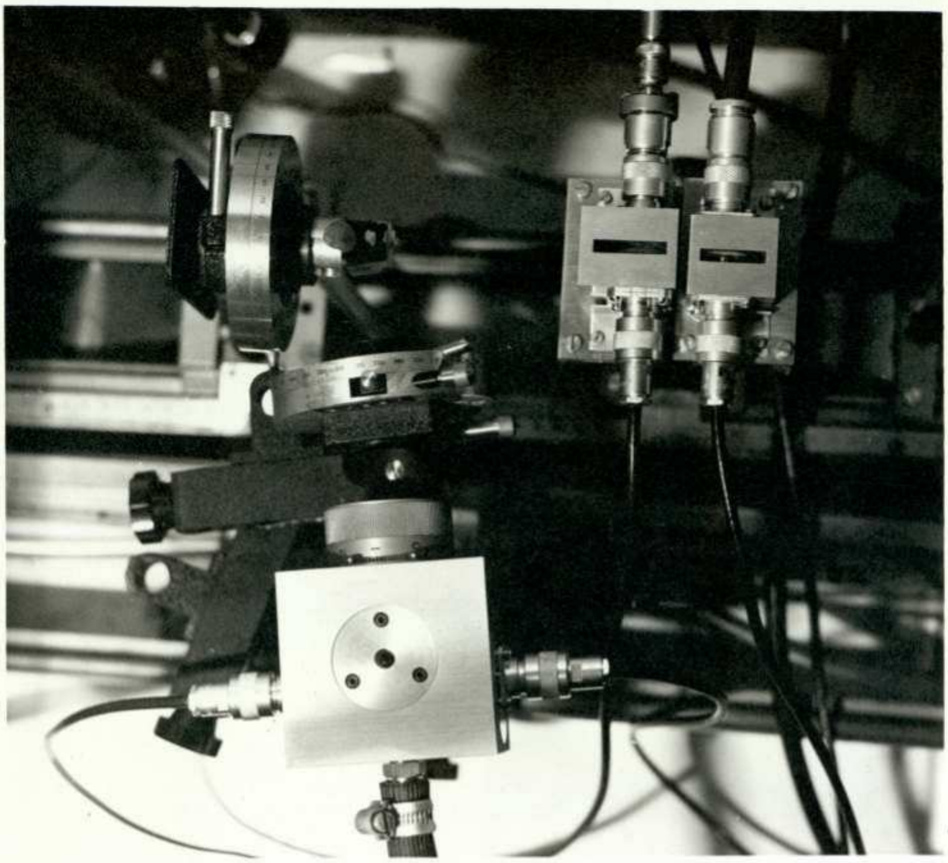

Fig 4.12 Double Pockels Cell and LTSG Arrangement

Minimum Pulse, Length Limited by Detector (3.5ns/cm)

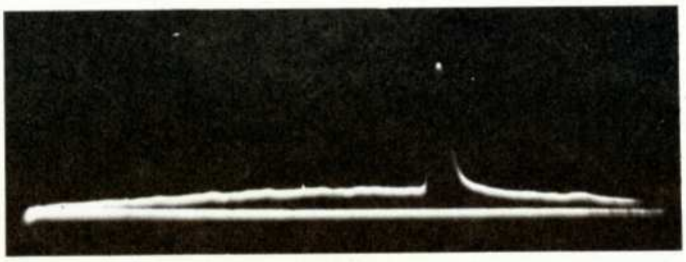

For optical pulse generation a second pockels cell was built to switch the light beam off just after the first pockels cell switched on. The arrangement for driving these two pockels cells from the two terminal LTSG is shown schematically in figure 4.11 and a photograph of the practical arrangement is given in figure 4.12 a)

Accurate determination of the minimum pulse length is difficult due to the film nonlinearity in the streak camera. A known pulse of 1ns width was generated by arranging the appropriate cable difference between L_1 and L_2 in figure 4.11. This difference was progressively reduced until the peak value of the light pulse began to fall. Half widths of 250ps were recorded by the streak camera before a fall in intensity was observed. A typical pulse is shown in figure 4.13.

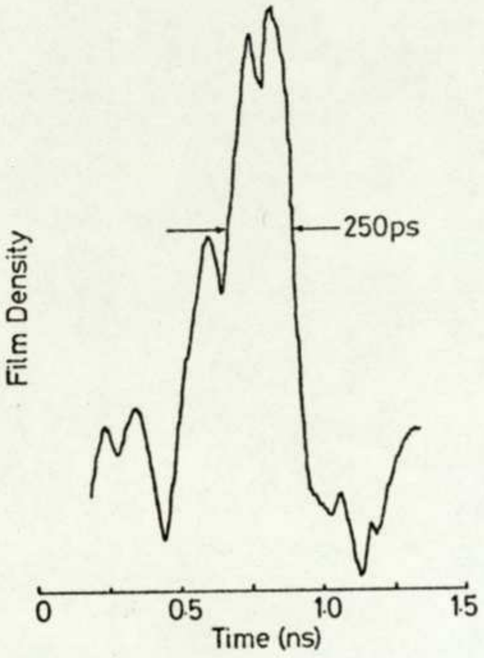

Optical Pulse

Fig 4.13

As the ratio of the cable difference in producing the 250ps pulse to that in producing the 1ns pulse corresponded exactly, it was considered that the measured half width of 250ps closely approximated the true optical pulse half width. Figure 4.12 b) shows the shortest pulse that was produced viewed with the photodiode oscilloscope combination after optical amplification, the indicated pulse length is limited by the response time of the measuring system.

SECTION 5 PARAMETER MEASUREMENT

Introduction.

Most people who have investigated the damage characteristics of transparent materials subject to high power laser illumination have been careful to specify very accurately the power and energy density at the point of damage, this being necessary to quote a figure for the absolute value of damage threshold.

Since the present work is involved with the pulse width dependence of damage threshold in materials that have been thoroughly investigated at one particular pulse length, the author has chosen to measure the damage threshold at differing pulse lengths and normalize these values. The normalized values may then be compared with the value recognised as the damage threshold for the material at that pulse length, which can be taken from the literature.

This method of measurement stipulates that the light in the area where damage occurs should be accurately specified in terms of its energy distribution but overcomes the error inherent in the determination of the absolute area. Together with this the peak power in the incident beam should be known since for a given area this will be proportional to the power density. Lastly the optical pulse should be specified absolutely and accurately in time.

This section deals with the specification and accuracy of all measured parameters used to produce the damage pulse length dependence curves given in section 6.

5.1 Definition of damage threshold.

When a laser beam passes through a dielectric material and a change in one or more of the materials properties occur, the change is termed damage. The damage can be reversible if the materials properties revert to their previous values after a given time or exposure to some annealing process. This thesis is concerned with damage that is permanent and therefore irreversible.

For damage to occur under the influence of incident optical radiation a proportion of this radiation must be absorbed by the material. The level of incident radiation necessary to raise the absorbed percentage to a value capable of causing damage is called the damage threshold of the material. The damage threshold will depend on two factors, the fraction of incident radiation absorbed and the absolute value of absorbed radiation that will cause damage.

Several authors have considered methods of detecting the onset of damage, Christmas(1973) measured the input and output beam power and tried to detect the point in time where a significant change in the two measurements occurred. Since the intrinsic absorption of the material at the wavelength studied was only in the order of a few percent the absorption at damage threshold would increase to several tens of percent, due to the dramatic increase of absorbing area. The practical limitation with this technique was that the crossectional area of the damaged region was very small compared to the optical beam crossectional area, thus reducing the percentage absorption measured by the ratio of the two areas. The resulting absorption was not large enough to be measured in practice.

In the present work the beam crossection is within an order of magnitude of the damaged region crossection at long pulse lengths making the above technique feasible. A problem occurs when very short pulse lengths are used. When a 20ns pulse is used to cause damage a detector with approximately 1ns risetime is sufficient to specify the power at which damage occurred. When a 300ps pulse is used to cause damage a detector with a response of approximately 15ps is required, the only detector with this time resolution available today is a streak camera. The use of this instrument to make accurate power measurements is not practicable.

There is a second technique for detecting the presence of damage which relies on visually detecting the presence of submicron sized scattering areas. Chu(1974) described the scattering effect of particles under the influence of laser radiation. This work indicates that using a 0.63 micron wavelength probing beam particles of approximately 0.03 microns or larger should be visible to the naked eye in at least one position in their field of view. In practice it has been found that scattered light from a particle can be seen with the naked eye where the particle itself could not be seen under a powerful optical microscope.

The technique of viewing the irradiated area with the naked eye and at the same time exposing it to low power 0.63 micron radiation from a HeNe laser has proven to be the most reliable and sensitive method of detecting the smallest damage regions. A 3mW HeNe laser was used which has no damaging effect on the eye when used in this way (Leith(1973)).

The above has been chosen as the method of detecting damage in this work. If a scattering point which was not present before the damage pulse was fired is visible after, then damage is said to have occurred.

The observation of each damage point also proved a valuable way of varifying that the damage mechanism was of a certain type, this will be discussed in detail in section 6.

5.2 Experimental measurement technique.

One of the most thorough investigations of damage threshold in the XDP materials was carried out by Christmas(1973). He studied the breakdown in ADP, KDP, and KD*P under the influence of 0.69 micron radiation at a pulse length of approximately 20ns. He attempted to produce shorter pulses but the system was unreliable and as a result he obtained no meaningful measurements at the shorter pulse lengths.

The measurements at 20ns involved focusing the light from a ruby laser with a converging lens. The sample was placed between the focus and the lens so that a power density existed ranging from a high value near tha focus to a low value near the lens. By measuring the position of damage within this gradient the power density was found. His measurements relied on a specific gradient and a known value of area at one point in the specified region. Defining the area can be difficult as many authors have found previously.

The author overcame this problem by not measuring the absolute area, but by relying on the fact that this area will be constant given that the laser operates under defined conditions. By comparing the peak input power for threshold at a short pulse length with that at 20ns a value of power density for threshold can be obtained which is normalised to that at 20ns.

The arrangement used to record the damage levels is shown schematically in figure 5.1 a). A beam of gaussian spatial distribution was focused to its diffraction limited beam diameter with a 10cm focal length lens. The sample to be tested was placed so that the focal point fell within its bulk, this ensured that the power density in the bulk was much greater than that at the surface, reducing the probability that surface damage should occur. After the pulse length was set the incident power was increased from a value below threshold, gradually, pulse by pulse, until a power was reached where damage occurred on at least five consecutive pulses, changing the position of the area illuminated after each pulse. The value of incident power at each pulse as well as the presence of damage was recorded on an experiment record sheet. The interpretations of these results are discussed in detail in section 6. Figure 5.1 b) shows the actual component arrangement.

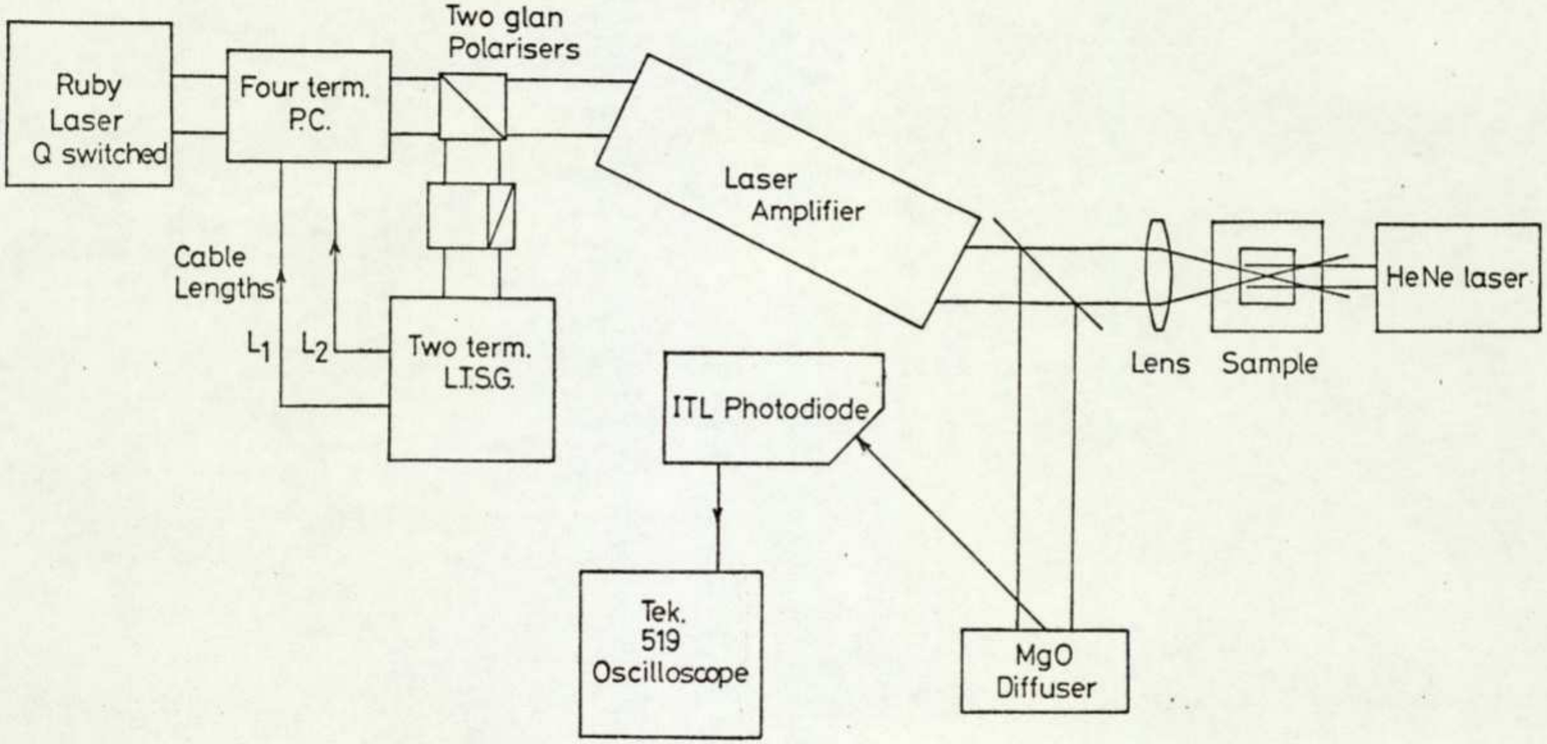

Experimental Arrangement for Damage Measurements.

Fig.5.1 a

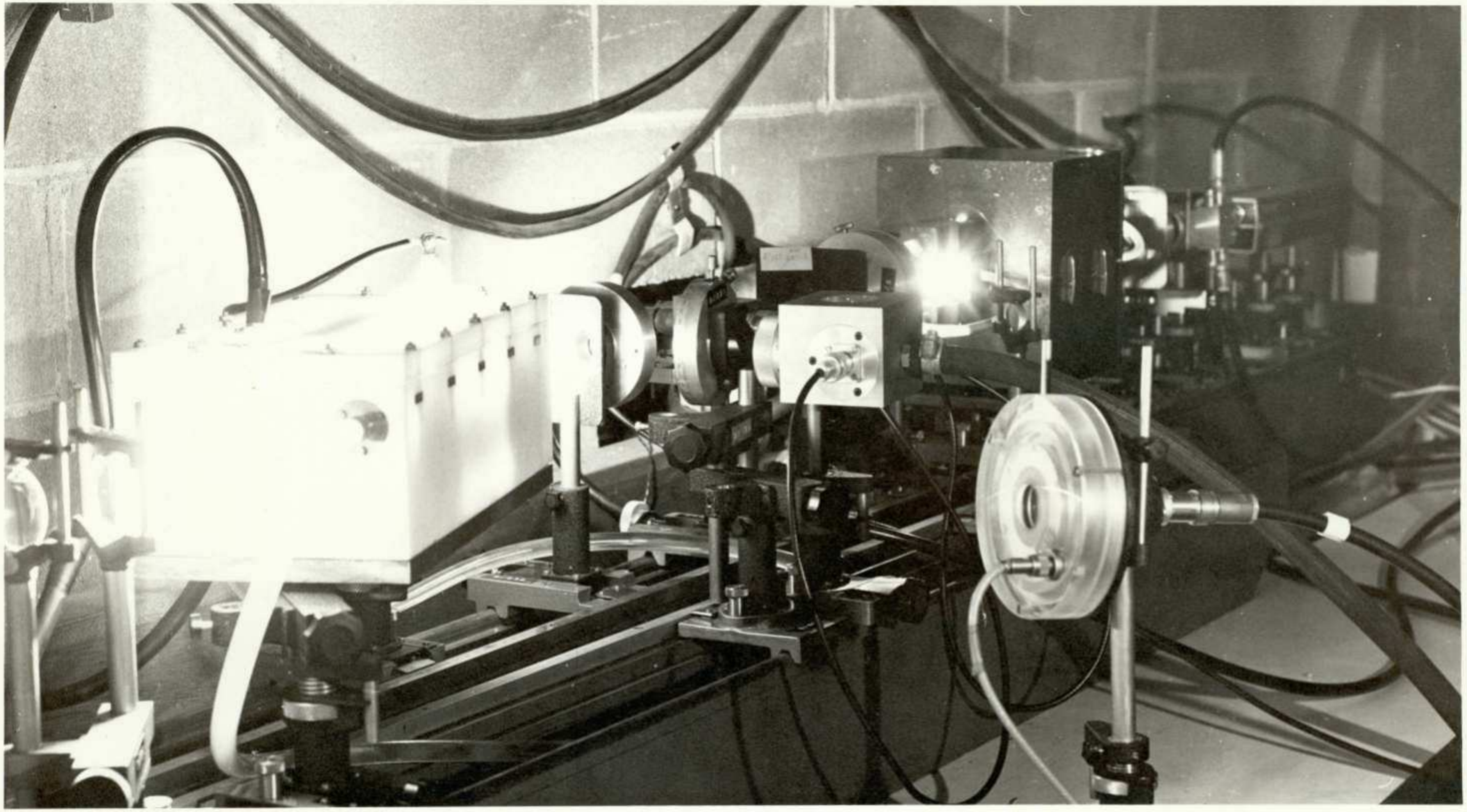

5.3 Damage area consistency.

Since the damage measurements quoted in this work are relative the absolute power density and hence beam area at the damage point are not required. The only condition which has to be satisfied is that the area be the same from pulse to pulse.

It is difficult to detect changes from a transverse mode other than TEM_{00}, to some other mode. If the laser operates at a higher order transverse mode, changes in mode shape could proceed undetected. When focused the power density distribution could vary from pulse to pulse leading to erroneous values of power density.

For this reason the single transverse mode gaussian spatial distribution of power density was used throughout this work, The production of this mode of operation is considered in the next part of this section.

Focusing the single transverse mode beam is very important since it is at the focal point that high damaging power densities occur. The consistency of the size of the focused spot affects the resulting power density trends. The absolute size of the focused beam area had to be estimated as this should have been large compared to the inclusion dimensions. This also helped to estimate the inclusion density within the crystals.

An estimate of the focal spot size can be found by considering the diffraction limited spot size of a beam with divergence θ_d focused with a lens of focal length f. The focused beam is incident normal to the crystal surface and forms the diffraction limited spot in the bulk of the crystal. The beam also passes through a layer of spectrosil glass and 'Freon E3' liquid. These two refractive index changes do not change the angle of convergence at the focal point so they do not have to be considered, although their presence was maintained throughout the experiments. An expression for the 1/e radius of the diffraction limited spot size r_o is

$$r_o = \frac{\lambda}{\pi\theta} = \frac{n\lambda}{\pi(\frac{a}{f} - \theta_d)} \quad \text{microns}$$

where λ is the radiation wavelength in microns, θ is the angle of convergence at the focus in radians, a is the 1/e input beam radius and n is the refractive index of the crystal (in the direction of propagation).

Kogelnik and Li(1966) give an expression for the change in beam radius with distance z towards the lens as

$$r^2 = r_o^2(1 + (\frac{\lambda z}{\pi r_o})^2) \quad \text{microns}^2$$

the 1/e length of the power density given by this area as shown in figure 5.2 is given by

$$z_{\frac{1}{e}} = \pi r_o^2\sqrt{e-1}/\lambda \quad \text{microns}$$

The volume in which damage is expected V_d is given approximately as the 1/e transverse area by the 1/e length

$$V_d = \pi^2 r_o^4 \sqrt{e-1}/\lambda \quad \text{microns}^3$$

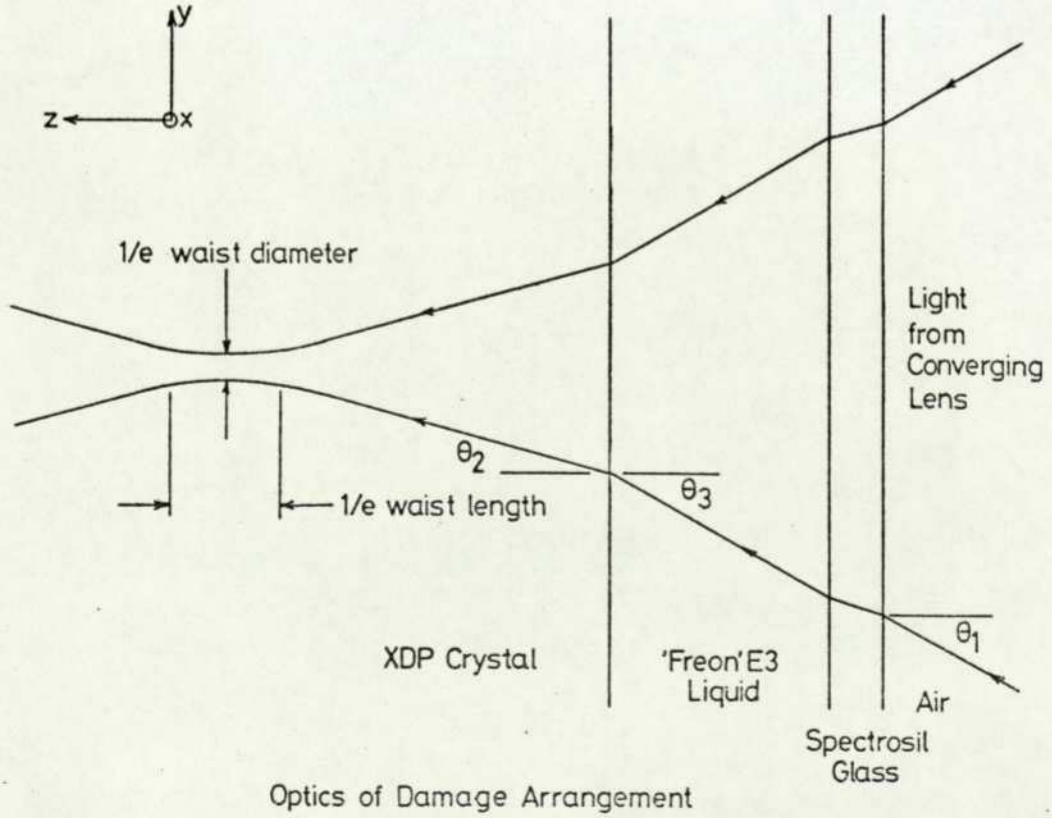

Optics of Damage Arrangement
Fig 5·2

The ruby laser system used for the damage measurements had a wavelength $\lambda = 0.69$ microns, a divergence angle $\theta_d = 0.005$ radians, beam diameter $2a = 6$ mm and the focusing lens had a focal length of 10cm. This gives θ, r_o and V_d from the above equations above as

$$\theta = 0.0183$$

$$r_o = 12\ \mu m$$

and

$$V_d = 3.8 \times 10^5\ \mu m^3$$

A practical estimate of the focused beam dimensions was found from the spatial beam profile investigation (section 5.4). The diameter was measured as approximately 50μm which is twice the calculated value. This inconsistency is possibly due to lens aberations and measurement error but is not important,and in fact reduces the possibility of error from effects such as conical refraction which will be discussed later.

The XDP materials are all anisotropic and fall into the uniaxial class of crystals. For any beam entering the crystal two refractive indicies are present each acting on the orthogonal components of the beam polarization. If the beam enters the uniaxial crystal along an axis other than one of the three principal axes two beams will be produced, their magnitude depending on the input polarization. Unless the input polarization is such that only one of the two beams can propagate in the crystal two discrete focal areas will be produced. For this reason the damage was always undertaken along a principal axis of the crystal (usually the z axis).

If the beam is incident along either the x or y axis two focal points will be produced along the input beam axis. They will be separated by a distance d where

$$d = y(n_o - n_e)$$

for small input convergence, y is the distance from the input face to the position the focus would occupy if the crystal had a refractive index of 1.0, n_o and n_e are the ordinary and extraordinary refractive indicies respectively. For KD*P $n_o = 1.5$, $n_e = 1.47$, if y is assumed to be 5mm then d = 0.15mm which is small compared to the waist length of 2mm given by the expression of Kogelnik and Li quoted earlier.

The above analysis neglects conical refraction which will occur with any converging beam, and is accentuated with the use of an anisotropic crystal. If the input beam is incident along the z axis only one beam propagates independant of the angle of polarization since the velocities in this direction are equal. Each ray in the incident cone will enter the crystal at a different angle to the z axis resulting in an elongation of the focal point. This will result since the off axis rays tend to form a focal point closer to the lens. The effective elongation can be found by considering the change in refractive index with the angle of refraction for both the e and o rays. If $n(\theta)$ is the refractive index experienced by a beam with wave normal at an angle θ to the optic axis then

$$n(\theta) = \frac{n_e n_o}{(n_o^2 \sin^2\theta + n_e^2 \cos^2\theta)^{\frac{1}{2}}}$$

Assuming an input cone of 0.03 radians in KD*P then $n(0.03) = 1.4999$. This indicates that the focus blurring for this amount of input convergence is very small, and as a result was neglected in these measurements.

It is apparent from the preceding discussion that for consistant damage area, from pulse to pulse, damage should always be incident along one of the three principal axes, preferably polarized in one of the remaining two axes. If the last condition is not satisfied it is possible that interference could occur between the two polarized rays travelling at different velocities. This would result in a nonuniform damage volume.

5.4 Laser mode stability.

The above discussion implies that it is essential that the laser operate in its single transverse mode. This is the mode which gives rise to a transverse power density distribution following an approximately gaussian relationship.

Varification that this was in fact the case with the laser used in this work was carried out using several quantitative and qualitative techniques. This investigation also revealed the divergence of the laser beam.

Initially the beam profile was photographed by placing an unexposed black and white film (Kodak Pan-X)

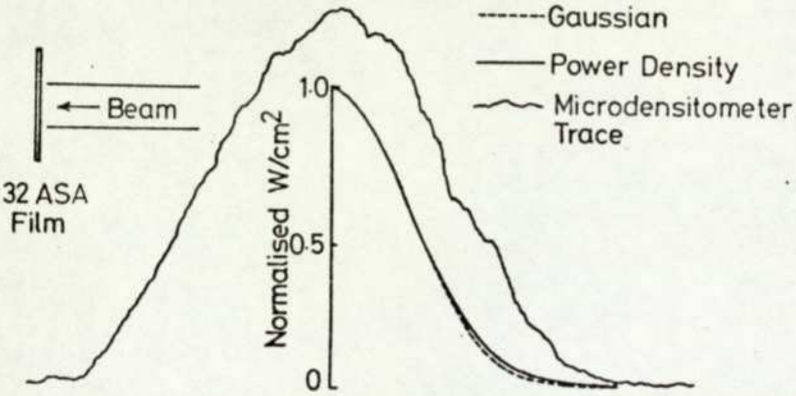

(a)
Film Density Response

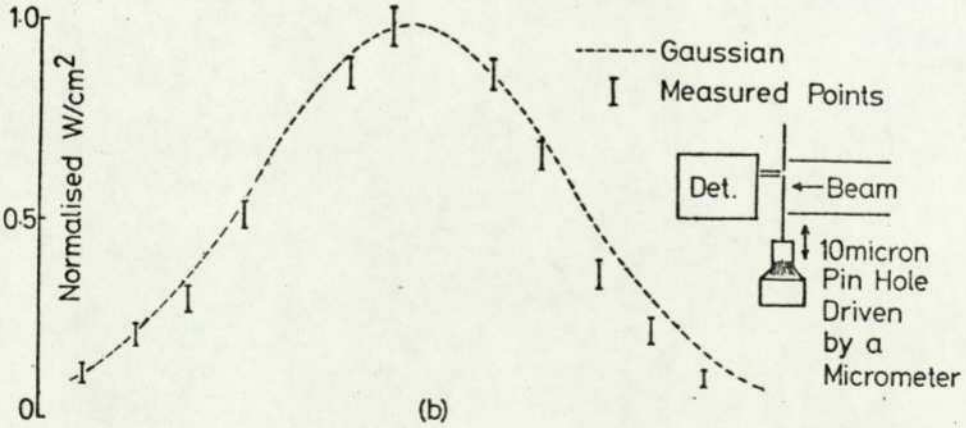

(b)
Spatial Power Sampling

Beam Power Density Distribution

Fig5.3

normal to the beam. A single pulse from the laser was used to expose the film.

An accentuated effect of the reciprocity factor of the film was noted, in that using a 20ns pulse the power required to give an adequate density on the film was less than a factor of 2 below the threshold for burning the film.

Figure 5.3 a) shows a microdensitometer trace of the exposed area of the film. When this trace is converted to the power density using the gamma function of the film the result is a relationship which is very close to being gaussian, in figure 5.3 a) the power density is given by the full line and the gaussian curve by the broken line.

A second quantitative result is given in figure 5.3 b) this is a plot of the power density at different points in the beam using different pulses for every set of readings at each position. To record this information a 10μm pinhole physically connected to a micrometer was use to scan the beam normal to the beam axis, a vacuum photodiode was used to record the power transmitted by the pinhole, this being proportional to the power density.

A qualitative verification of single mode operation was achieved by focusing the beam to its diffraction limited spot size, and using this high power density to burn a crater in a piece of copper. The high spatial frequencies assosiated with modes other than the TEM_{oo} mode would have resulted in the distribution at the focus being irregular. The crater produced revealed a very even dome shape when viewed under a microscope.

Of the two quantitative methods described above the pinhole measurement should be the most accurate, the reciprocity factor of the film in the first method leads to very narrow ranges of linearity of the film gamma function and hence large errors.

The change in beam diameter of the unfocused beam was measured at two points in the far field region to determine the beam divergence.

The single mode operation of the laser was achieved by placing an aperture within the laser cavity. The aperture was a 2mm diameter hole in an aluminium disc. Several different diameters were used but 2mm produced reliable single mode operation. The Fresnel number of the cavity using this aperture was 3.2, this is a low value and suggests that the laser should give stable single mode operation.

A secondary effect of the aperture is to reduce considerably the high power that the laser is capable of producing, this was sacrificed to ensure single mode operation.

5.5 Photodiode power monitor.

The device used to monitor the peak power level of the damaging pulse was an ITL FD125 vacuum photodiode. For reasons already described the absolute sensitivity of this device was not required, but an estimate of the consistency of its power indication was needed.

Much work has been carried out in this field, Edwards(1969, 1970, 1976) has investigated the effect of short pulse resolution and long term drift. He measured the rise and falltimes of the FD125 to be 620ps and 950ps respectively on a high repetition rate sampling system. Using a Tektronix 519 oscilloscope with 300ps risetime he also showed that the total rise and falltime became 715ps and 996ps respectively. It is obvious that this detector would be inadequate for measuring pulses of less than 1ns in length.

For this reason the photo diode used by the author was calibrated using a streak camera which will be described in a following part of this section. Pulses of 1ns and 300ps were recorded with both the streak camera and photodiode under constant conditions. Microdensitometer traces were used to varify the optical output, by comparing these with the photodiode intensity reduction in output when going from 1ns to 300ps a derating figure was obtained. This was approximately 2.1 for the photodiode used in this work.

Long term variations were shown to depend heavily on the biasing conditions and temperature at which the photodiode operated. Using intermittent biasing (switching off at night and on again in the morning) and uncontrolled temperature, Edwards(1970) showed that variations in sensitivity of up to 45% could be experienced over a period of 24 weeks. When a permanent biasing condition was imposed along with the control of temperature, a photodiode used with 0.69 micron radiation stayed within 5% of its mean value.

During the period of the damage measurements the photodiode was left switched on, while the experiments were conducted in an airconditioned laboratory. The overall power density measurement error was estimated to be less than ±5% for all pulse lengths, except the 300ps measurements where the effect of the streak camera calibration would increase the error slightly.

5.6 Pulse length measurement.

A streak camera consisting of a GEC P856 image deflection tube and a sinusoidal oscillator for the streak generation was used to measure the fast risetimes and pulse lengths produced by the new pockels cell. This basic streak camera arrangement has been discussed in detail by Palmer(1973).

The GEC P856 tube was driven by a sinusoidal 25MHz 1kV peak to peak oscillator. This voltage was applied to a set of plates on the tube which had a deflection sensitivity of 60mm/kV measured at the phosphor screen.

The oscillator was of the Hartley type, a circuit diagram is given in appendix 2. The frequency was measured with a Marconi TF643C frequency meter and by measuring the period of the sinusoid on a Tektronix 585A oscilloscope. The quality of the sinusoid was determined by measuring the value of any harmonics present using the Marconi frequency meter. The fact that no harmonics could be detected in the range up to 300MHz indicated that the oscillator was generating a low distortion sinusoidal signal.

The optical pulse was imaged onto the cathode of the image deflection tube using a 50mm f1.2 Cannon lens. The vertical plates of the tube were used to deflect the vertically oscillating image from one point to another between exposures so that several streaks could be obtained on one sheet of film. Several streaks had to be taken for each reading as the probability of getting the required optical risetime or pulse within the linear region of the sinusoidal oscillation was approximately 0.3. This can be seen in figure 5.4 which shows the tangential slope at the maximum rate of change of velocity of the image across the screen. This slope S is given by the expression

$$S = M\pi/T \quad \text{mm/ns}$$

where M is the peak to peak displacement of the image on the film in mm, T is the period of the applied sinusoid in ns.

The choice of frequency used to drive the deflection tube was a compromise between the maximum sweep rate S needed to resolve picosecond pulses and the minimum light level needed to expose the film.

Because of the low spatial frequency response of the GEC P856 tube a sweep rate of at least 200ps/mm as seen on the phosphor is needed to realize 100ps pulses. At this sweep rate there are barely enough electrons

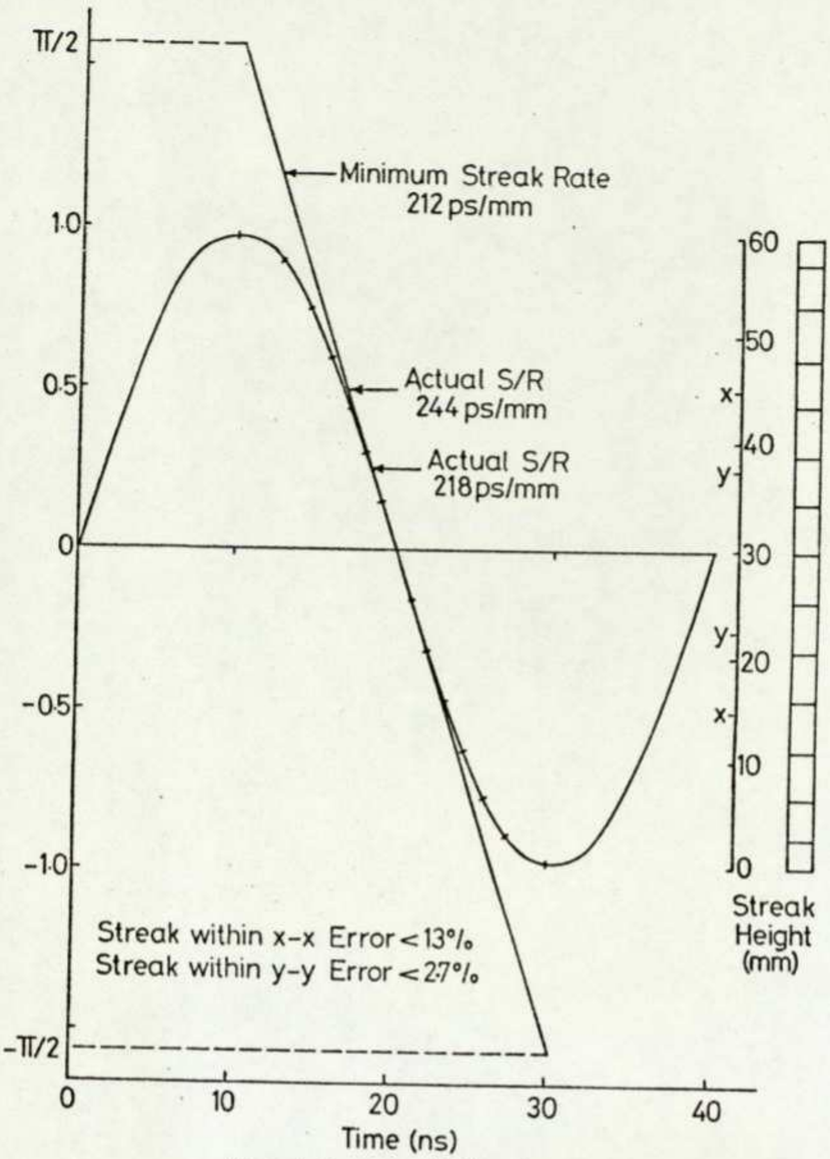

Streak Camera Calibration

Fig5.4

generated by the cathode to produce sufficient light after striking the phosphor to expose the film used (Kodak type 2485 developed in Kodak MX642-1 developer for 4 minutes at 32°C having an effective rating of 12000 ASA). One factor contributing to the lack of sensitivity was the fact that the P856 tube had an S11 cathode which has a response at 0.69 microns of less than 0.1 of its peak response at 0.44 microns. With incident light on the cathode increased above a certain value the cathode would saturate (and slightly higher it would burn), below a certain value the film would not respond. The intensity dynamic range of the streak camera was therefore very limited. One method of overcoming this would have been to use an image intensifier. A sweep rate of 200mm/ns was used which specified an oscillator frequency of approximately 25MHz.

The laser beam that was switched by the pockels cell was expanded so that it would completely fill the aperture of both the 5mm aperture pockels cell built by the author and the 10mm aperture commercial pockels cell. The beam was focused by an anamorphic lens with its long focal length in the horizontal plane and a focal length of 10cm in the vertical plane onto a screen, the image formed was then focused onto the streak tube cathode by the f1.2 Cannon lens. This provided the possibility of studying the spatial time resolution of the pockels cell as well as the overall risetime.

Since the production of each pulse was achieved by the voltage step from the LTSG an arrangement was investigated to slow down the rate of change of voltage and apply this to the P856 tube inplace of the high frequency oscillator. This would produce a voltage ramp that would be perfectly synchronized with the event being photographed. In practice the production of a relatively slow ramp from a 180ps risetime pulse that was free from interference was found to be very difficult.

5.7 Overall accuracy.

Figure 5.4 gives a graphical representation of the maximum error in time measurement that could result by not having the reading at the centre of the spatially oscillating image. Considering this result and the accuracy of the frequency measurement, the maximum error in time measurement for all readings on the streak camera was estimated to be less than 13% and typically in the region of 4%.

The errors involved in relative power density measurement are small compared to those resulting if absolute values were determined. Christmas(1973) calculated an overall error in his power density measurements of 32% maximum and typically 16%. In the present work the accuracy of a figure quoted for power density at a pulse length relative to that at a standard pulse length is the combination of the possible variations of power measurement and the possible variations of focused area.

The power measurement was discussed in section 5.5 and a value of ±5% was quoted. The focused area error from pulse to pulse is more difficult to evaluate. Christmas quoted a value of 10% for the absolute area measured using the photographic method. This figure does not include the possible pulse to pulse variation since his measurement of area was made from only one pulse. The pinhole photodiode method of beam diameter measurement produces an error band associated with the power reading at each point in the beam area for several laser pulses. If two curves are drawn through the extremities of the error bands one represents the largest diameter and the second represents the smallest diameter (figure5.3). The error resulting for the system was approximately ±3%. This figure contains the error of beam stability and power reproducability, the latter should be very small but the former can be high in this type of laser especially where high repetition rates are used (faster than 1 shot per minute), due to schleiring effects within the ruby and cooling system water. The actual focused spot size error from pulse to pulse should be considerably smaller than ±3%.

Using the power and area errors the maximum overall error in the measured power densities would be ±8%.

SECTION

6

EXPERIMENTAL DAMAGE RESULTS

Introduction.

The results of an investigation of inclusion damage in any material are heavily dependent on the sample chosen for the investigation. This is because the properties responsible for this form of damage are not intrinsically related to the material, but are introduced in some way during the manufacturing process.

In this section the validity of assuming a generatized result from that of several specific results is considered. Results of the pulse length dependence of damage threshold of three different samples of ADP and four of KD*P are given.

The interpretation of the statistical nature of the method of measurement is used to predict the volume density of inclusions which are responsible for damage.

An investigation of the size and composition of these inclusions is discussed, the latter in relation to the information available after damage has taken place.

6.1 Crystal samples.

The ADP used in this work was from a batch grown for the Admiralty by Boush Clevite in the United States. This ADP is several years old but proves to be very consistant in quality. Using a HeNe laser probe beam, scattering points could be observed in most samples. Iron is introduced in minute quantities in the ADP growing process. It is thought to be present in its ionic form and not as discrete metalic inclusions.

The KD*P used in this work came from two sources. Two of the samples were grown by Isomet in the United States. In the manufacturing process this material was filtered using a 0.3 micron filter. A mass spectrometer analysis of the material revealed the results in table 6.1.

Two crystals of KD*P were grown in the UK by Cyncryst. The mass spectrometer analysis of this material is also given in table 6.1, this material was filtered using a 10 micron filter in the manufacturing process.

The number of scattering points observed in the KD*P was considerably less than that in ADP.

The position of areas that were investigated for damage threshold was chosen without prejudice, with the exception that large obvious inclusions were avoided. The distribution of the damage results for both the ADP and KD*P indicate a consistency of material from crystal to crystal.

Element	Isomet		Cyncryst	
	A	B	C	D
Chromium	<1	<1	3	3
Iron	3	2	60	60
Nickel	2	2	—	—
Copper	<1	<1	<1	<1
Sodium	~54	~78	—	—
Aluminium	—	—	50	50

Mass Spectrometer Analysis (ppm)
of KD*P used in this Work
Table 6.1

6.2 Damage threshold verses pulse length results.

The three samples of ADP studied gave consistent results. The maximum deviation from the mean value of damage threshold was 12% for the 20ns pulses, 10% for the 2.5ns pulses and 4% for the 300ps pulses (two samples only were investigated at 300ps). The mean of each of these damage thresholds were in the ratio 1:1.05:>4.1 for 20ns, 2.5ns and 300ps respectively. Figure 6.1 illustrates these results graphically. A continuous line is drawn through the points for comparison with theories that will be developed later.

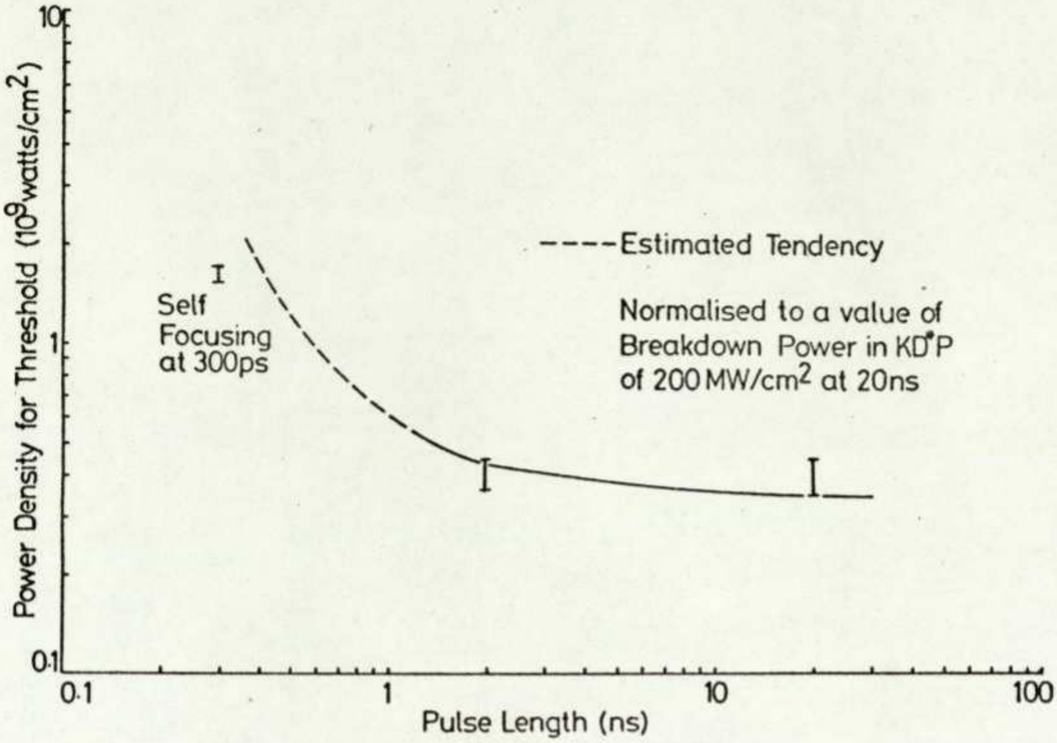

Measured Power Density Threshold
verses Pulse Length
in ADP

Fig 6.1

Damage occurring at the 300ps pulse length was not inclusion damage. The damage shown in figure 6.2 a) is typical of damage at this pulse length in ADP. Figure 6.2 b) shows inclusion damage in ADP at 20ns pulse length for comparison, both damage areas in figure 6.2 occured just above threshold. The damaged region in figure 6.2 a) was approximately 3mm long and 3μm wide. This geometry is typical of self focusing. Inclusion damage can be seen along the self focusing track. The illumination of ADP with 300ps pulse length radiation was the only occasion where self focusing was observed at threshold levels.

Of the four samples of KD*P studied only three will be considered in the pulse length dependence results as the fourth was chosen due to the fact that it had obvious inclusions, this sample was used specifically in the inclusion size and composition investigation.

The consistency of the results for KD*P was similar to that of ADP with the exception of one crystal which for one set of measurements gave a damage threshold at 300ps of 2.5 times that obtained with a different crystal at the same pulse length. When the measurements

Fig 6·2(a) 300ps Self Focusing Damage in ADP (×200)

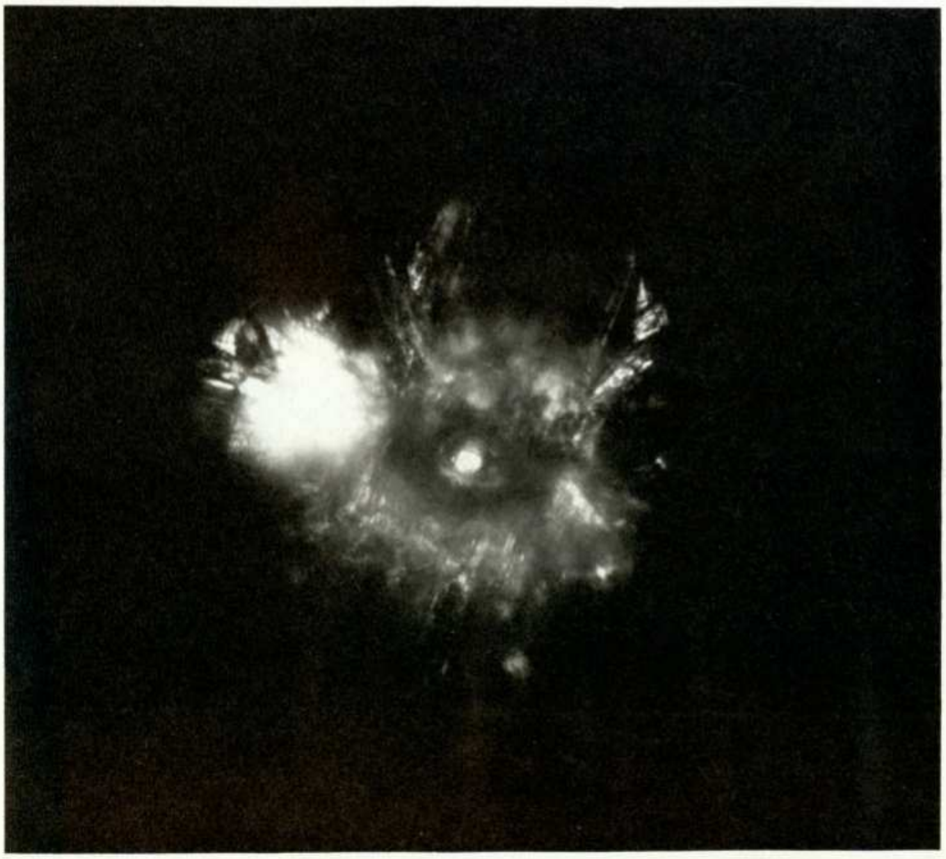

Fig 6·2(b) 20ns Inclusion Damage in ADP (×100) were repeated at a different position in the crystal the results agreed with those of the other crystal. The ratios of the mean of these results were 1:1.8:2.6 for 20ns, 2.5ns and 300ps pulse lengths respectively. Figure 6.3 illustrates these results graphically. Figure 6.4 a),b) show the 300ps pulse length damage and 20ns pulse length damage respectively. Note the difference between figure 6.4 a) and figure 6.2 a), the damage in KD*P at this pulse length is inclusion damage and this was typical of damage at this pulse length.

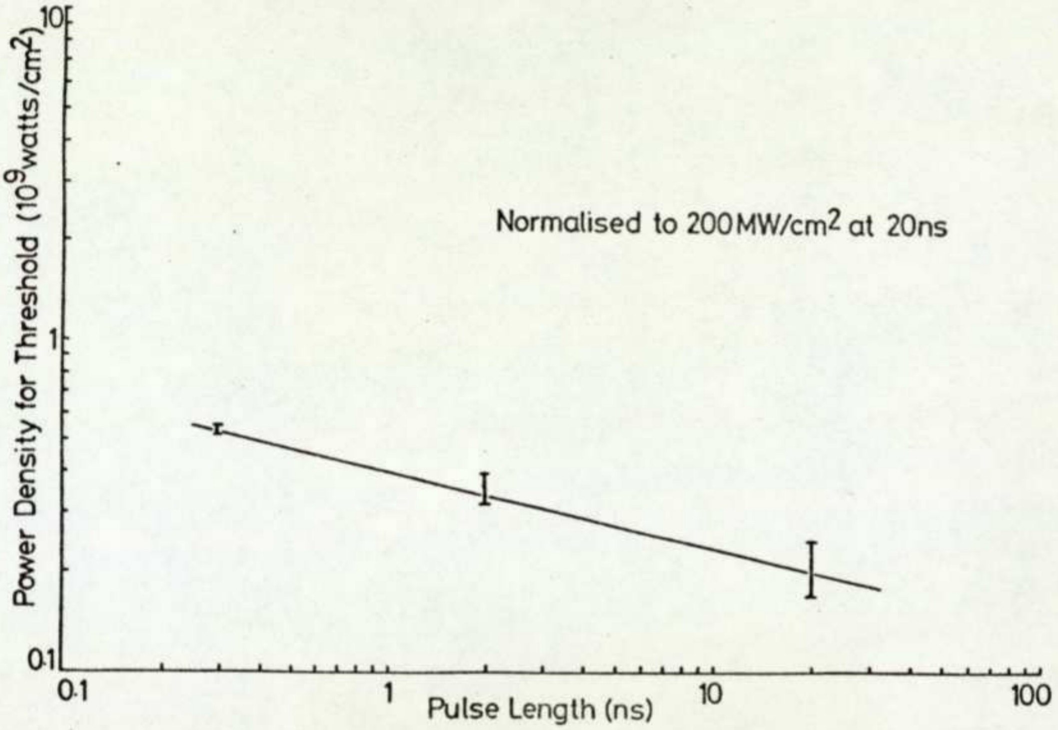

Measured Power Density Threshold verses Pulse Length in KD*P

Fig 6.3

The appearence of damage in ADP at 20ns and 2.5ns was virtually identical to that in KD*P at the same pulse lengths. At 2.5ns damage was usually either a small sphere of 5-10μm diameter (figure 6.5 a)) or the same sized sphere with a disc of cleavage extending hundreds of microns into the bulk of the material (figure 6.5 b) looking at an angle to the disc). The damage caused by the 20ns pulse was much larger than that at 2.5ns even when the 20ns pulse damage was very close to threshold. Figure 6.5 c) shows a 2.5ns damage sphere and disc edge on, together with a single sphere of damage. The damage size fell into specfic regions, the ranges and ratios of damage site sizes not including areas of crystal cleavege were 100-10:10-2:2-x(where x was to small to be measured) μm for 20ns, 2.5ns and 300ps respectively.

Fig 6.4(a) 300ps Inclusion Damage in KD*P (×200)

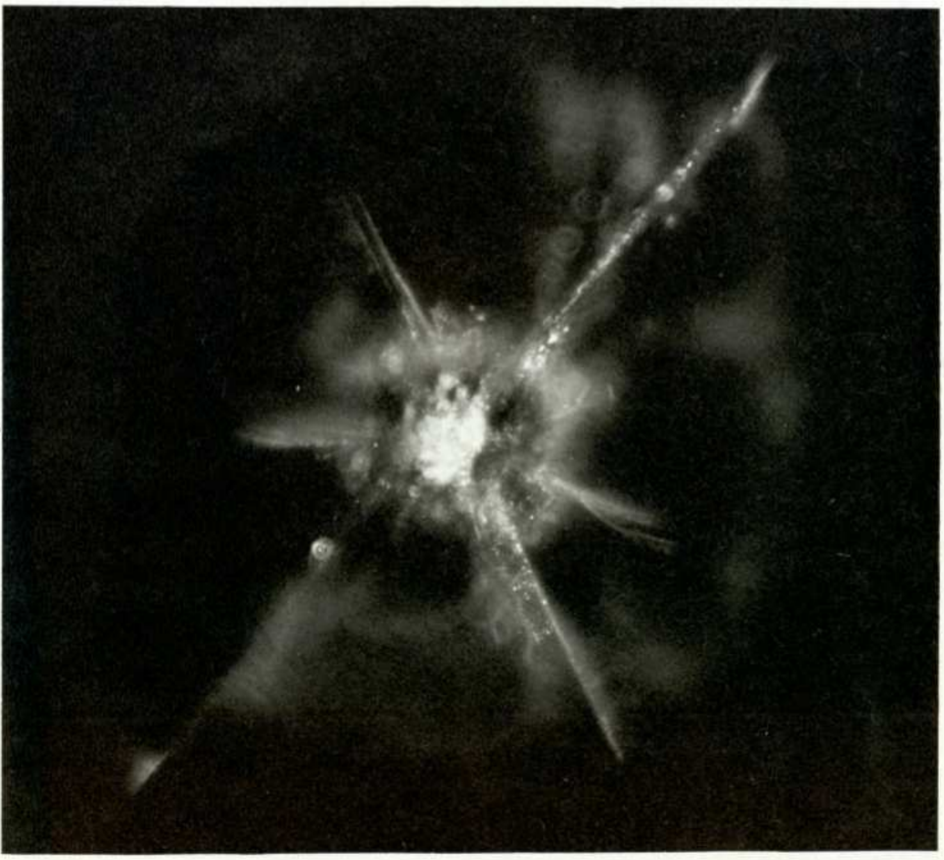

Fig 6.4(b) 20ns Inclusion Damage in KD*P (×100)

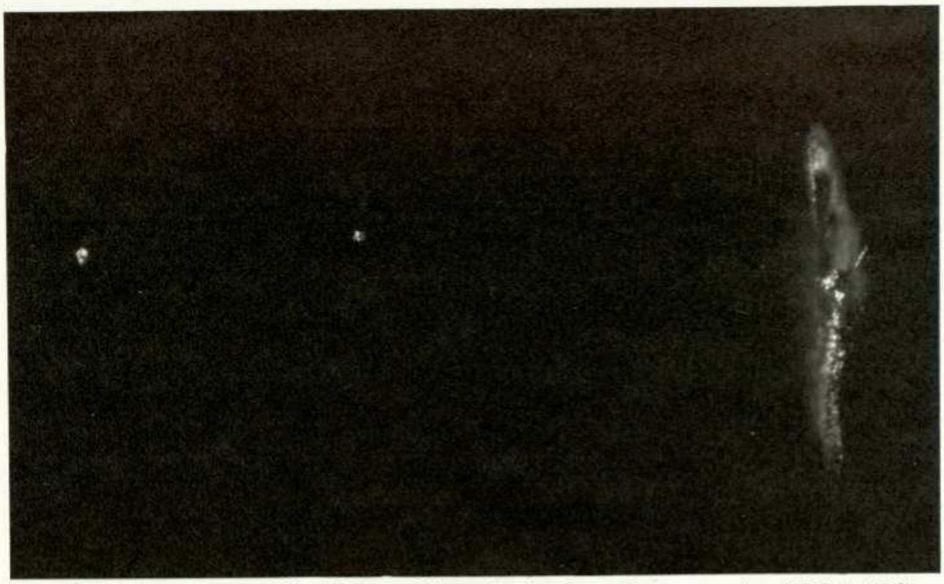

Fig 6·5(a) 2·5ns Inclusion Damage in ADP (×100)

Fig 6·5(b) 2·5ns Inclusion Damage in ADP (×100)

Fig 6·5(c) 2·5ns Inclusion Damage in ADP (×400)

6.3 Interpretation of damage results.

The information from the damage measurements was recorded such that the presence of damage for a series of power levels was varified, the visible form of each damage region was also recorded. These measurements were tabulated in a manner that clearly showed the resulting damage threshold value as well as an area of uncertainty. Figure 6.6 shows a typical result for KD*P at 20ns and 2.5ns pulse length. The minimum power that caused damage (neglecting freak events that were obviously not representative of the typical crystal) was taken as the value of damage threshold, P_{th}. As figure 6.6 shows the probability of damage continued at a value less than 1 up to some power density P_c. This band of uncertainty has special significance when the inclusion volume density is considered.

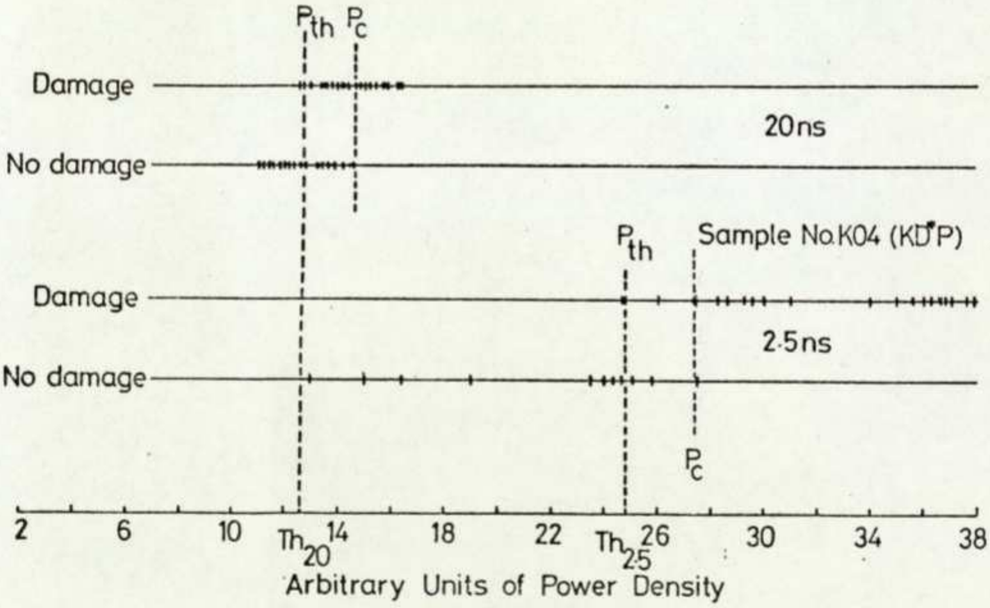

Graphical Representation of
Damage Measurements
Fig 6.6

The volume of material that experiences a power density level above the threshold level is a function of the fraction the power density is above threshold. Figure 6.7 illustrates this condition for one plane parallel to the optical axis of the system. If the power density is initially low the volume of material above threshold will be zero, when the peak of the power density distribution curve strikes the threshold level P_{th} the volume V will be very small and the probability of an inclusion being in this volume is small. As the power density increases the volume V increases so the probability of finding an inclusion within V increases, this corresponds to the region of uncertainty in figure 6.6. When the volume V reaches a level V_c where the probability of finding an inclusion is one, which corresponds to power densities above P_c the inclusion volume density can be assumed to be $1/V_c$ inclusions per unit volume.

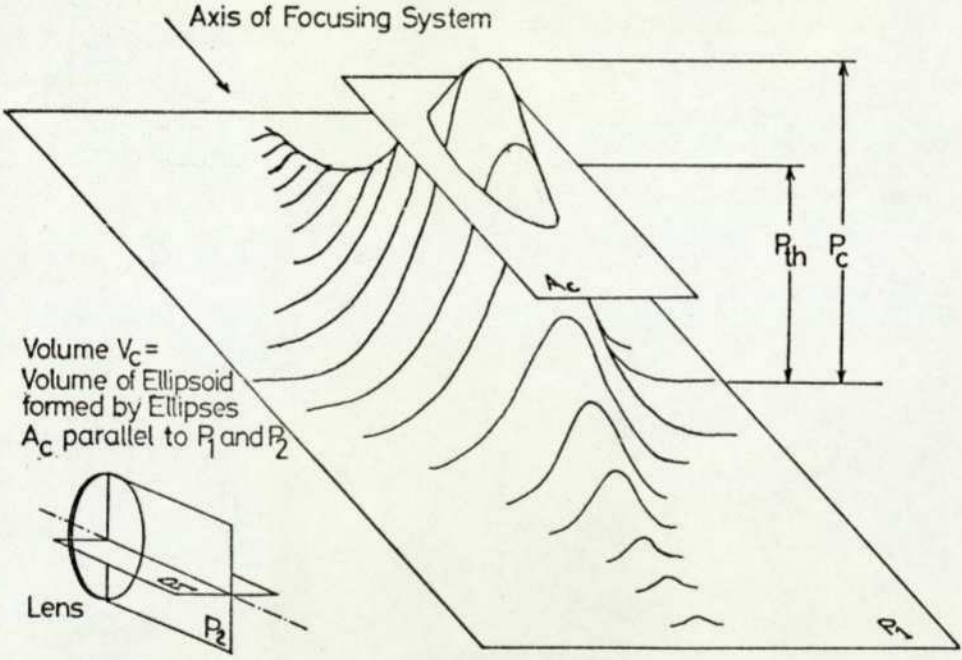

Volume where the Probability is One
that Damage will Occur

Fig 6.7

Due to the fact that the absolute power densities were not known the absolute volume densities could not be found, but a comparison of some crystals varified that this technique could give a true indication of the relative volume densities of inclusions responsible for damage.

The normalized distribution of power density across the beam focus is given by

$$P = \exp(-\frac{r^2}{A})$$

where r is the radius normal to the optical axis and A is a constant. The distribution along the optical axis of the beam can be approximated for this analysis by

$$P = \exp(-\frac{z^2}{B})$$

where z is the distance from the geometric focus and B is a constant.

The volume of material with power density greater than P_{th} in a distribution with peak power density P_c is given by the inequality

$$V \alpha (-\log(P))^{-\frac{3}{2}}$$

where $P=P_{th}/P_c$.

Then a relative figure $(-\log(P))^{-\frac{3}{2}}$ can be quoted for a material which is proportional to the volume density of the inclusions.

Analysis of the experimental results revealed that the ADP had approximately the same volume density of inclusions causing damage at 20ns as that at 2.5ns. A quantitative investigation was possible with the KD*P samples. In section 6.1 the sample history revealed that one sample of KD*P had been filtered with a 10 micron filter and the other two samples had been filtered with a 0.3 micron filter, this implies that the concentration of inclusions in the range from 0.3 to 10 microns should be lower in one sample compared to the other. The results indicate that the mean value of the relative volume density of inclusions damaging at 20ns and 2.5ns is 6.6 and 20 respectively for the two 0.3 micron filtered samples. These figures for the 10 micron filtered sample of KD*P were 20 and 500 for pulse lengths of 20ns and 2.5ns respectively. The presence of a lower density of inclusions causing damage in the finely filtered sample corresponds to the theory derived in the next section of this work relating the size of inclusions responsible for damage to the pulse length of the radiation causing the damage.

A second point gained from the analysis with KD*P was that in the three samples studied inclusions causing damage at 2.5ns existed in higher concentrations than those responsible for damage at 20ns.

The above technique could be used as a basis for an instrument that could quantitatively test the quality of optical components. Not that a sample with one inclusion per unit volume is any better than one with one thousand inclusions per unit volume as both will cause damage at the same power density, but in the manufacturing process monitoring of the inclusion density might reveal methods for reducing the inclusion density which applied simultaneously could reduce the number of inclusions to zero.

6.4 Damage at known inclusions.

An investigation was undertaken to determine the effect on the damage threshold when inclusions of known size were present. One sample of KD*P had large voids of up to 80 microns diameter which appeared when the crystal growing process was interupted. The voids were formed along lines following the natural crystal edges and were thought to contain dideuterium oxide. This is thought to be one of the possible causes of inclusions in KD*P

A sample of ADP was found to have a high concentration of inclusions in one area. The size of these inclusions could not be measured accurately but they were estimated to be no larger than 10 microns in diameter. Using this sample and the HeNe laser probe beam to photograph the inclusions before and after exposure to high power densities, a set of measurements was taken at 20ns pulse length. Figure 6.8 shows the results of

Before Damage After Damage

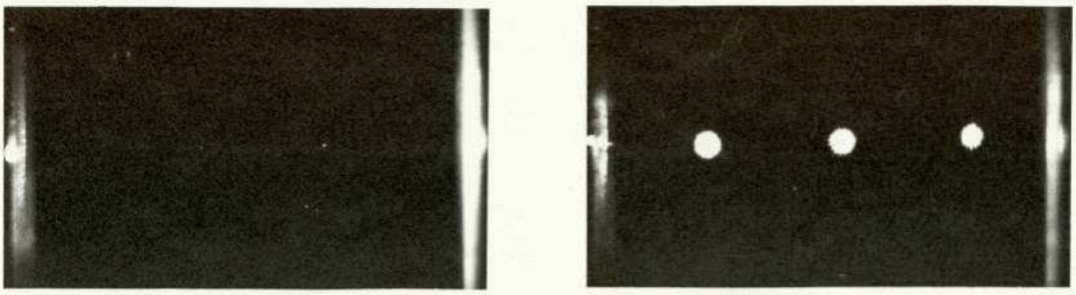

Area 1

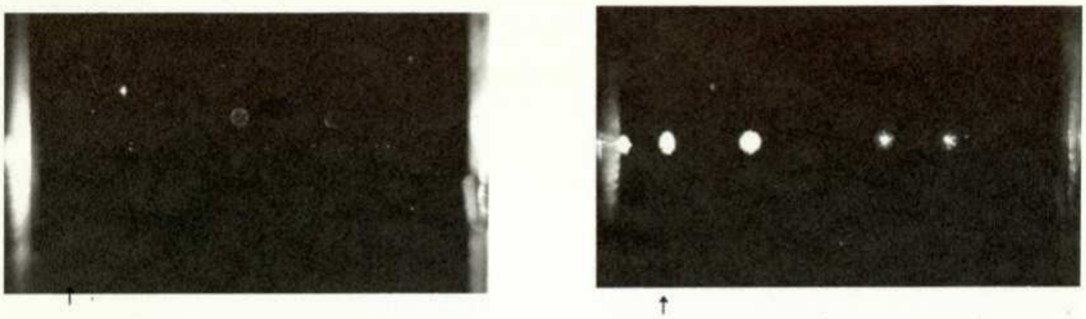

Area 2

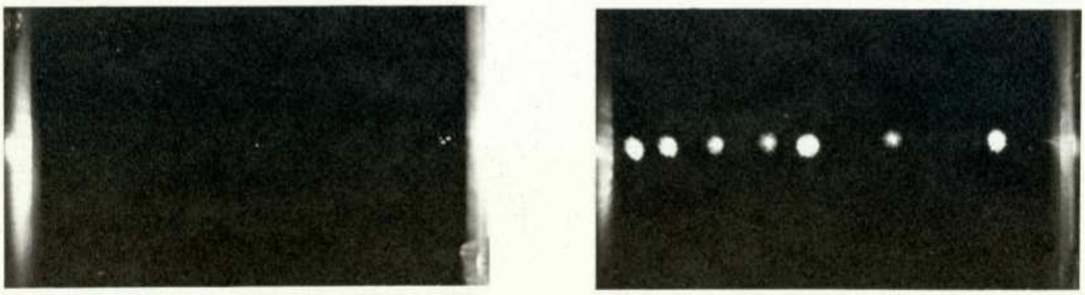

Area 3

Selectivity of Size of Inclusion Damaged (x 1)

Fig 6.8

three which were typical of a total of fourteen which were photographed. The value of damage threshold that was associated with these measurements was within 12% of the mean of all other measurements of damage threshold in ADP at 20ns.

The obvious result illustrated by figure 6.8 is that the presence of visible inclusions appears to have no effect on the damage threshold. Of the 15 damage points only 1 occured at a position where a visible inclusion was previously present. This together with the fact that the damage threshold was not affected indicates that inclusions of this size are not responsible for damage at this pulse length.

The sample of KD*P was investigated firstly with an optical microscope and secondly with a scanning electron microscope. Figure 6.9 a) shows the line of voids viewed with the Reichert optical microscope. Two specific sizes of voids can be seen, the larger approximately 35 × 80 microns and the smaller approximately 20 × 20 microns, the shapes were regular and the same, from void to void of the same size. Figure 6.9 b) and c) show scanning electron microscope photographs of the large and small voids respectively. The sample was prepared by breaking the crystal in a plane through the line of voids pictured in figure 6.9 a) and viewing the surface immediately afterwards. The stresses in the crystal around the voids are clearly visible with an area of high stress reaching at least 100 microns away from the large void, this is invisible when viewed with the optical microscope even under crossed polarizers.

An attachment to the electron microscope could perform X-ray fluorescence analysis at a point in the area being viewed, apart from phosphorus nothing above sodium in atomic weight could be detected within or around the void. No inclusions of this type less than 10 microns in size could be found (using the optical microscope) but the

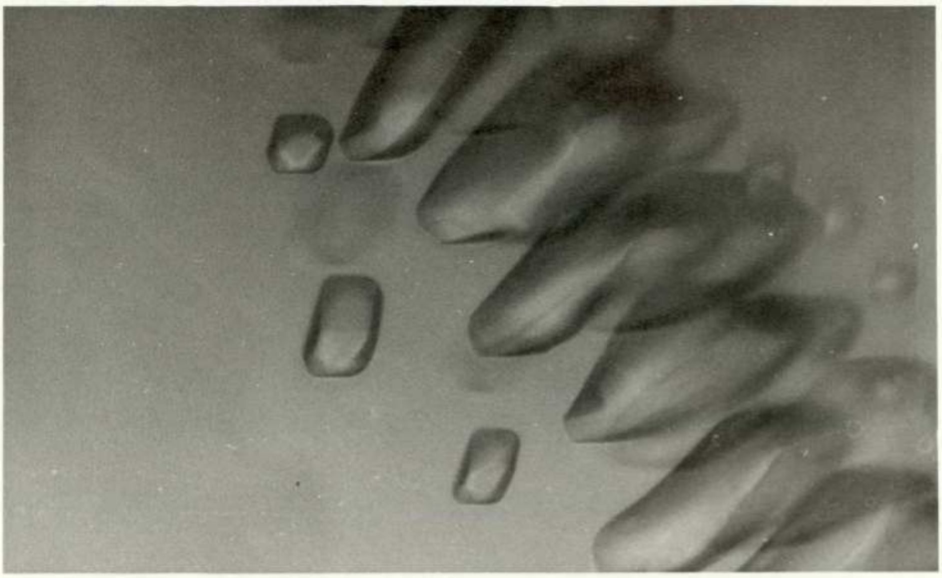

Fig 6.9(a) Growth Voids in KD*P (×200)

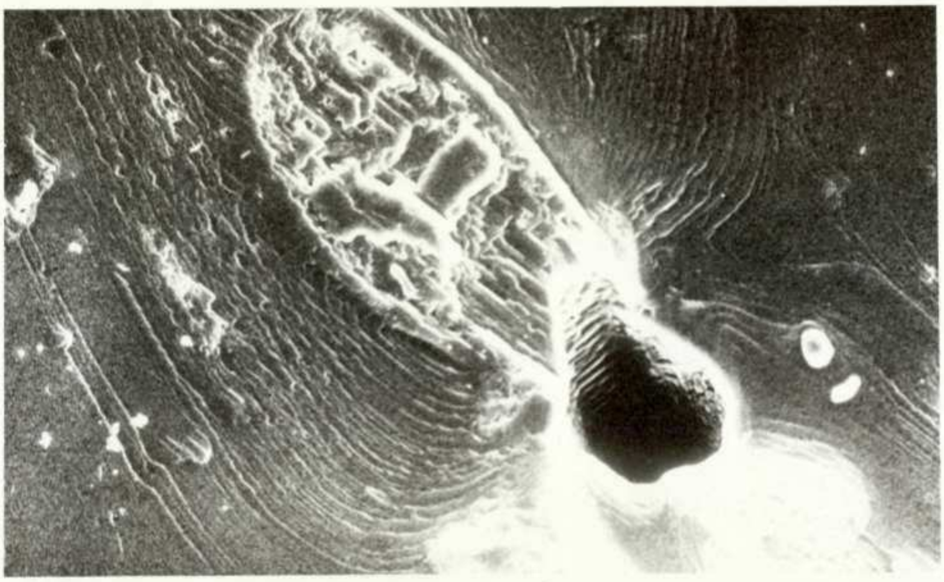

Fig 6.9(b) Large Void Fractured (×300)

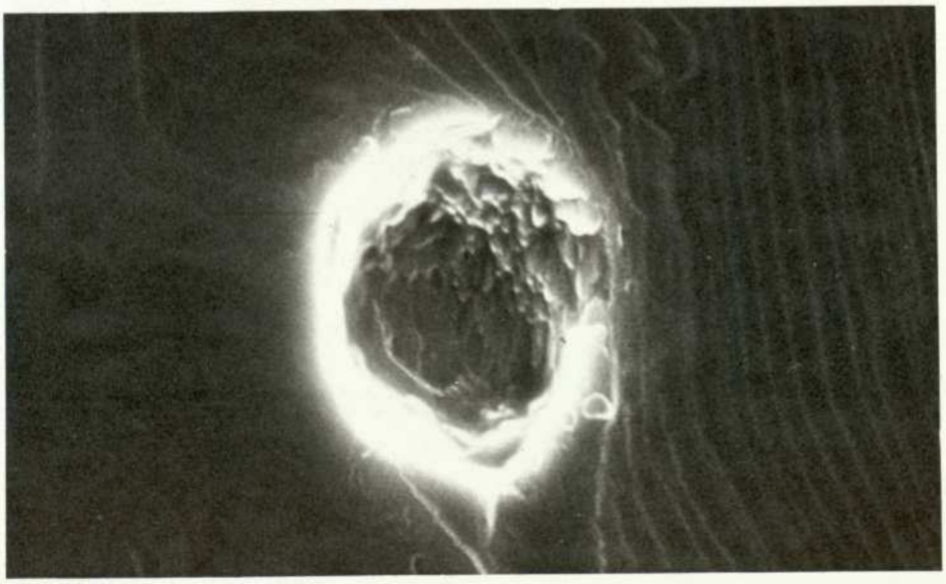

Fig 6.9(c) Small Void Fractured (×1000)

absence of such voids does not mean that the stress variations within the crystal were not present.

Before these voids were investigated as described above they were subject to a set of damage measurements at 20ns pulse length. The laser radiation was focused on to ten different voids in succession with increasing power in the usual manner. Five of these pulses caused damage, in three of these five, damage was remote from the void in the remaining two damage was close to a void. The result of the damage threshold level was within 8% of that for the mean of KD*P at 20ns pulse length. The conclusion from this investigation in KD*P was that voids such as these are unlikely to cause damage in the 20ns pulse length range.

6.5 Inclusion damage site investigation.

Solving the problem of determining the composition of inclusions which cause damage is the first step in reducing the damage threshold of a material. The secondary electron scanning microscope used with an X-ray fluorescence analysis unit (XRF) is one of the few methods of determining the composition of very small amounts of material in localised areas on the surface of a material. The basic problem associated with the use of such an instrument for the analysis described here is that inclusions of interest are present in the bulk of the material and XRF can only analyse material at the surface.

Two techniques were used, both relying on detecting any material deposited on the walls of the cavity produced after the inclusion had caused damage.

A sample of ADP was damaged by placing the sample between the focus and lens, at the exit face where the power density was enhanced by reflection damage occurred. The damage was severe due to the fact that the power density was considerably above damage threshold. This exit face was investigated using XRF techniques.

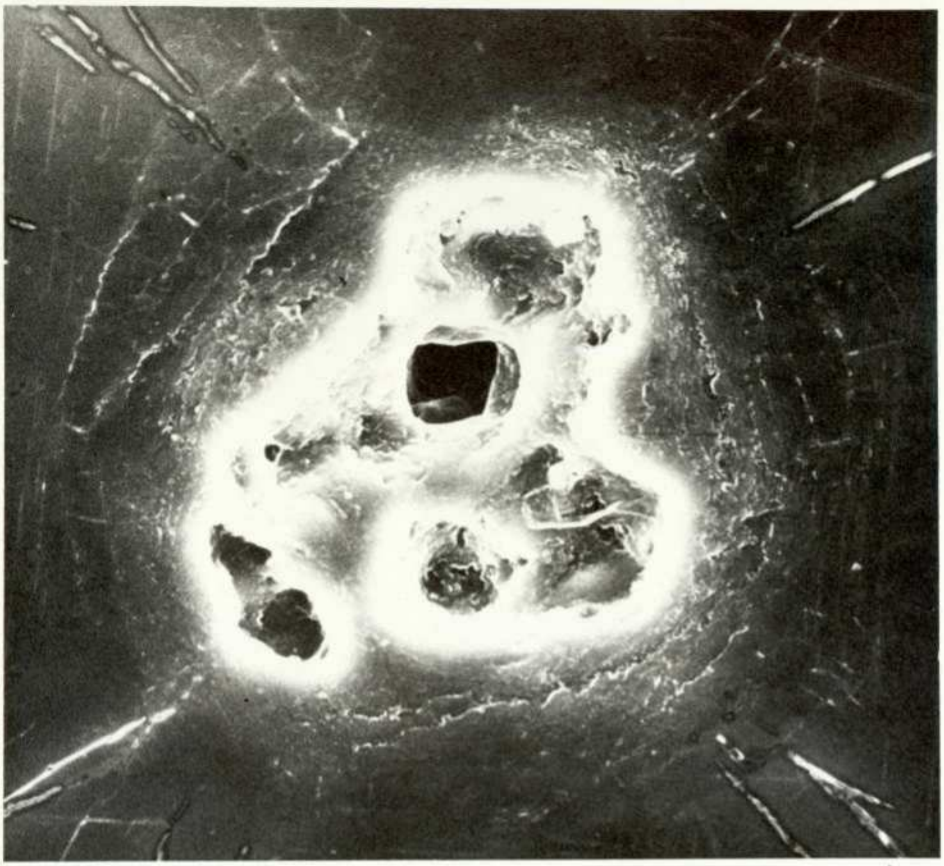

Fig 6.10 20ns Surface Damage in ADP (×300)

Figure 6.10 is a view looking towards the laser. A hole approximately 150 microns in diameter can be seen extending into the crystal with what appear to be inclusion craters along its length. Craters can also be seen at the exit face. Cleavage planes along the minimum stress axes of the crystal are visible radiating from the principal damage region. XRF revealed nothing apart from phosphorus in the damage region.

This negative result could have been due to the fact that the crystal had to be cut to size to fit the electron microscope sample holder. This entailed the application of cutting oil and cleaning with acetone which could have removed any deposits present in the damage region.

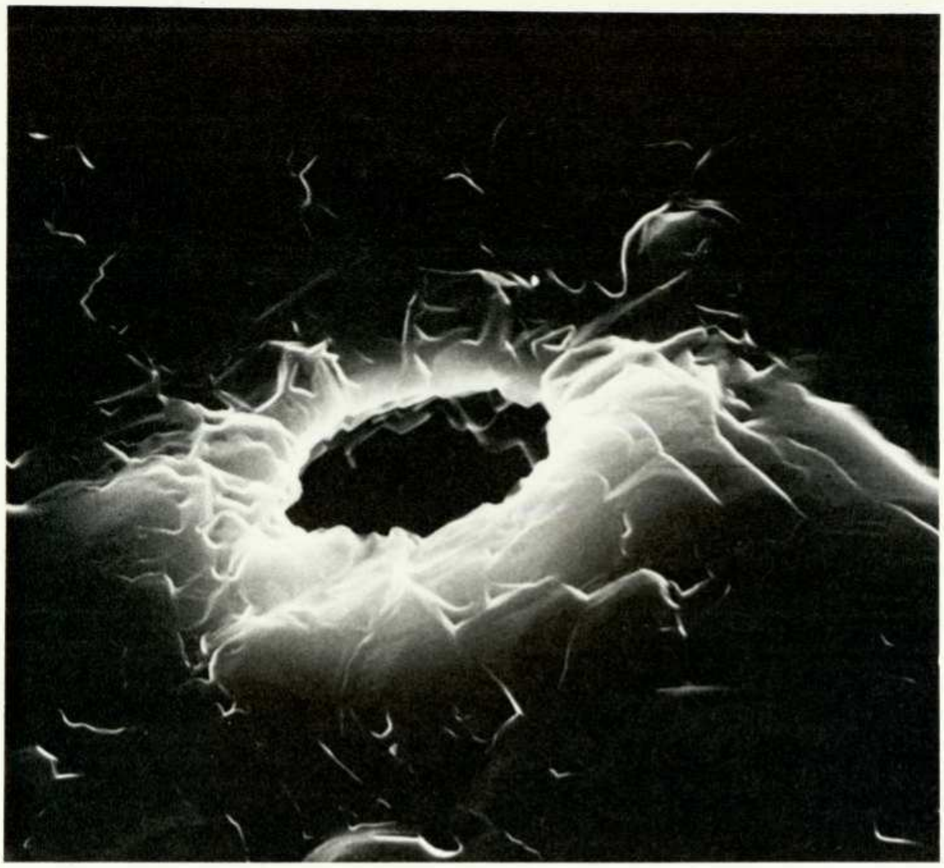

Fig 6·11(a) Damage Site in ADP (×2700)

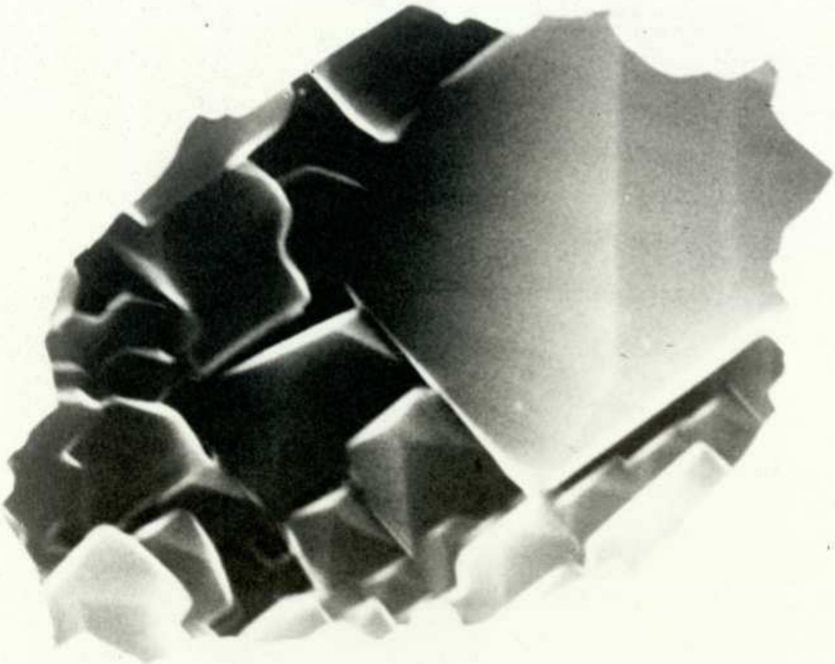

Fig 6·11(b) Detail of Damage Site in (a) (× 8500)

A second technique was used to try and detect remaining deposits of the original inclusion within the damage site. A sample of ADP which had been used in the damage threshold measurements was used. This sample had approximately 30 damage sites within its bulk. The sample was shattered, then, using a microscope, a piece was found which contained a 20ns damage site, the centre sphere in this case was approximately 13 microns in diameter. The damage site was approximately 1mm under the surface of a piece approximately 4mm square. Using a pair of tweezers, a scalpel and a dissecting microscope the small sample was immersed in acetone and layers of ADP were scraped from the surface until the nucleus was reached. The instant the nucleus was pierced a stream of several dozen bubbles each being no smaller in volume than the nucleus itself rose to the surface of the acetone. One further light scrape was made to ensure an adequate opening for the XRF studies. The resulting hole was then flashed with 150 angstroms of carbon and placed in the scanning electron microscope. Figure 6.11 a) shows the resulting hole, the roughness around the hole is due to the fragmented chipping caused by the scalpel.

The orientation of the cleavage disc through the nucleus was such that it was still present in the bulk of the crystal below the nucleus in the lower part of the photograph, comming out of the face of the crystal (and hence removed) at approximately 45° towards the upper part of the photograph. Figure 6.11 b) shows an enlarged view of the inside of the nucleus, minature boulds of ADP can be seen growing with the same orientation. The smaller boulds were less than one micron in size. The presence of the boulds is probably the cause of the dimpled structure of the nucleus when viewed with the optical microscope (figure 6.4 b)).

X-ray fluorscence studies were made of the visible area of the hole. A large peak corresponding to the spectrum of phosphorus was present as a basic constituent of ADP. A very small peak almost indistinguishable from the noise in the system was found corresponding to the spectrum of alumimium. It is expected that this was due to the presence of a small amount of aluminium in the system. If aluminium had been the original inclusion its presence would have been detected in considerable quantities. This analysis indicated that no element, apart from phpsphorus, above sodium in atomic weight was present in the cavity. Further, more intensive, experimental work will have to be undertaken to varify whether or not the traces of aluminium detected were related to the measuring environment or the actual crystal inclusions.

The observation of the bubbles comming from the nucleus when it was fractured shows that the sphere contained a gas under a relatively high pressure. This suggests together with the perfectly formed boulds of ADP that the high temperatures dissociated the ADP leaving a gas or gas mixture of either nitrogen oxygen or hydrogen, the molten material that was not dissociated reformed as small boulds of ADP.

SECTION

7

INCLUSION BREAKDOWN THEORY

Introduction.

The low damage threshold power densities measured when inclusions are present in the bulk of a material are attributed by most authors to the fact that inclusions absorb some of the incident energy. The resulting increase in temperature causes stresses that can be sufficient to fracture the bulk material. Bennett(1971) suggested that the increase in temperature of the inclusion and surrounding bulk material could cause a focusing effect producing higher than normal power densities. For the XDP materials this is impossible since the effective lens produced would be a diverging lens, due to the negative change of refractive index with temperature.

Both Bennett and Hopper et al(1973) considered the problem of finding the temperature of an inclusion in a bulk material subject to exposure by high power radiation. They used basicly the same technique of solving the heat diffusion equation for the inclusion and its surrounding material. Hopper considered only platinum in a typical laser glass. Bennett compared the stresses produced by platinum and aluminium oxide inclusions in two common laser glasses.

Both the analyses of Hopper and Bennett assume that the crossectional area of the inclusion for energy absorption calculations is equal to the physical crossectional area of the inclusion. In this section it is shown that this assumption can lead to significant errors since the inclusion sizes are comparable to the optical wavelength of the incident radiation.

The following theoretical work considers the temperature increase of submicron inclusions subject to pulses ranging from picosecond to nanosecond lengths.

7.1 Inclusion temperature.

In appendix 1 an equation describing the temperature of inclusions in ADP and KD*P after exposure to laser radiation is derived. This equation together with that derived by Hopper and Uhlman(equation 7.11 in appendix 1) describe the temperature of any inclusion in any bulk material. The final equation applicable to metalic and dielectric inclusions in ADP and KD*P is equation 7.16 from appendix 1.

$$T = \frac{3\epsilon_\lambda JR}{mC_{vi}D_g}\Bigg[\frac{m}{q^2+m^2} + \frac{\exp(\frac{q^2-m^2}{4R^2}D_g t)}{\sqrt{q^2+m^2}}\left(\sin(\frac{qmD_g t}{2R^2})\frac{q}{q^2+m^2} - \cos(\frac{qmD_g t}{2R^2})\frac{m}{\sqrt{q^2+m^2}}\right)$$

$$\operatorname{erfc}(\frac{q\sqrt{D_g t}}{2R}) - \frac{2}{\sqrt{\pi(q^2+m^2)}}\exp(\frac{-m^2 D_g t}{4R^2}) \int_0^{\frac{m\sqrt{D_g t}}{2R}} \exp(\delta^2)\cos(\frac{q\sqrt{D_g t}}{R}\delta -$$

$$\frac{qmD_g t}{2R^2})\ \frac{q}{q^2+m^2} - \sin(\frac{q\sqrt{D_g t}}{R}\delta - \frac{qmD_g t}{2R^2})\frac{m}{\sqrt{q^2+m^2}})\,d\delta\Bigg] \qquad 7.16$$

Equation 7.16 specifies the temperature of an inclusion with radius R and heat capacity C_{vi} within a host material of heat capacity C_{vg} and diffusivity D_g. The inclusion is exposed to radiation of J joules with a pulse length of t seconds, under the condition that $3C_{vg}/C_{vi}$ is less than 4. This equation has not previously been published. The presence of oscillatory terms is interesting, one effect is to produce a secondary maximum of temperature in the very short radius region, the position of which depends on the specific material physical properties.

The integral in equation 7.16 was performed using a 10 element numerical integration. Checking the accuracy of this with a 100 element numerical integration it was found that a small error exists with the 10 element integration for extremly small inclusion radii.

Equation 7.16 gives the temperature rise for an inclusion with radius large compared to the wavelength of

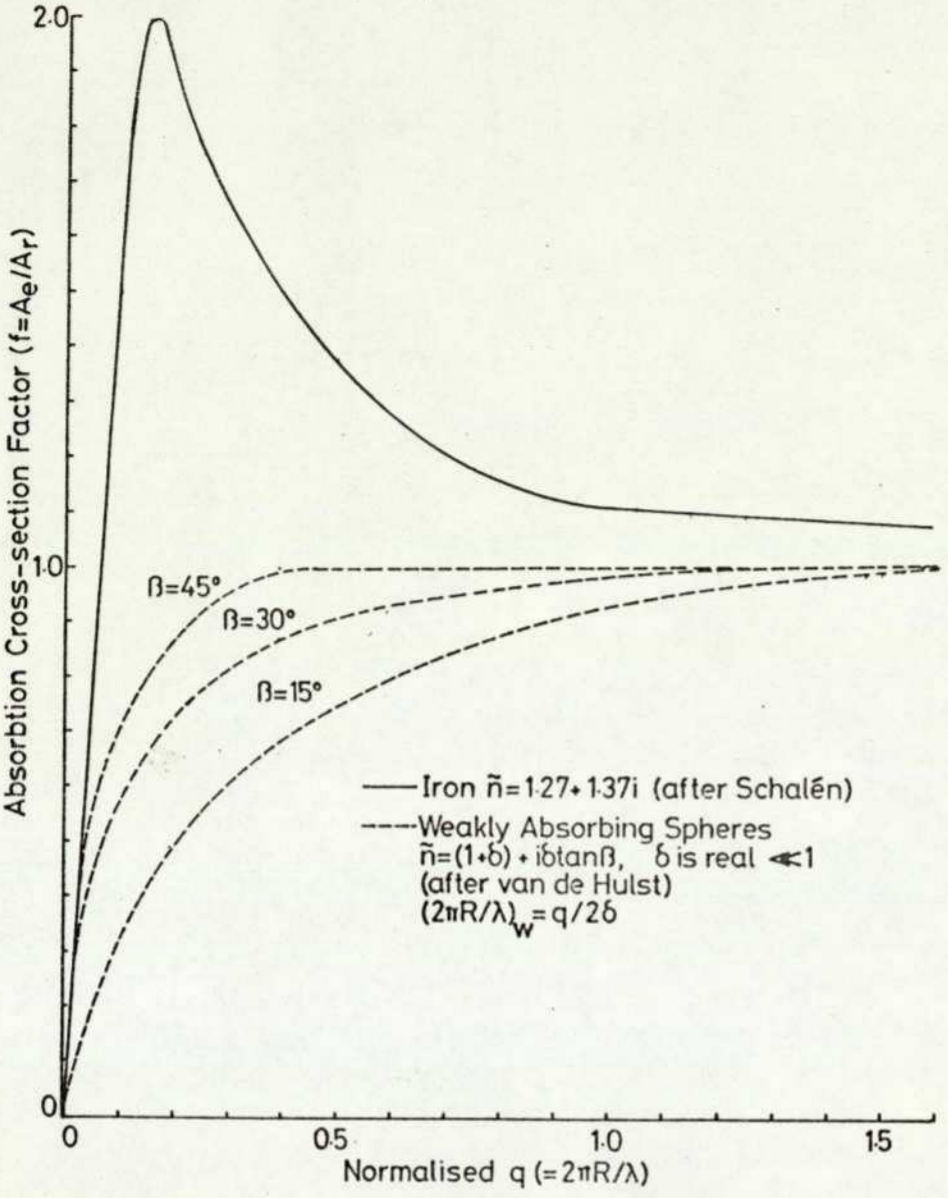

Absobtion Cross-sectional Area Variation
with Incident Light Wavelength
(Born & Wolf)

Fig 7.1

the incident radiation. A closer approximation to the temperature of the inclusion would be achieved if the temperature is multiplied by a factor f which accounts for the fact that the wavelength of the incident radiation is in the same order of magnitude as the inclusion radius.

The scattering of radiation incident on a small partical was considered by Mie in 1908. He derived expressions for the magnitude and direction of scattered radiation as a function of the physical properties of the material. These results are given by Van de Hulst(1950). The absorbed energy can be found by subtracting the scattered energy from the incident energy. The expression for the scattered radiation from a conducting absorbing sphere is very complicated. Only a small number of authors have considered special cases, (see Born and Wolf(1970). One special case was that of iron particles with a refractive index of $n = 1.27 + 1.37i$. Iron is one of the inclusion possibilities considered in this work. The other inclusion possibilities, aluminium, tin and lead have similar refractive indices (compared to dielectrics), so the factor f for iron will be used in the general equation for metals. The ratio of the effective area for absorption to the geometrical crossectional area is f and can be seen in figure 7.1 plotted against the physical crossectional area. The solid line representing iron and the broken lines representing weakly absorbing spheres with a refractive index of $n = (1+\delta) + i\delta\tan\beta$ where δ is small and real. $2\pi R/\lambda$ for these weakly absorbing spheres is $q/2\delta$ where q is the horizontal scale in figure 7.1. This means that the absorption crossection for a weakly absorbing sphere is much less than 1 for relatively large inclusions.

Equation 7.16 together with the information in figure 7.1 is the basis of a computer program written to find the temperature variation with particle size and pulse length. This program is listed in appendix 4.

Figures 7.2 and 7.3 give the resulting temperature of inclusions of iron and aluminium in ADP and KD*P respectively for pulse lengths of 20ns, 2ns and 200ps. The emissivity of both aluminium and iron has been taken as 0.3 and the input energy as a constant value of 20 J/cm^2 for each pulse length. Relevant values of the physical properties of the inclusions were taken from Carslaw and Jaeger(1950) and for ADP and KD*P from the Handbook of Electro Optic Materials(1972) edited by J.T.Milek and M.Neuberger.

7.2 Temperature induced stress.

The stress produced by the increase in temperature of the inclusion has also been considered in detail by both Hopper and Bennett. The fact that the thermal physical properties of the materials involved are only known at moderate temperatures and pressures means that

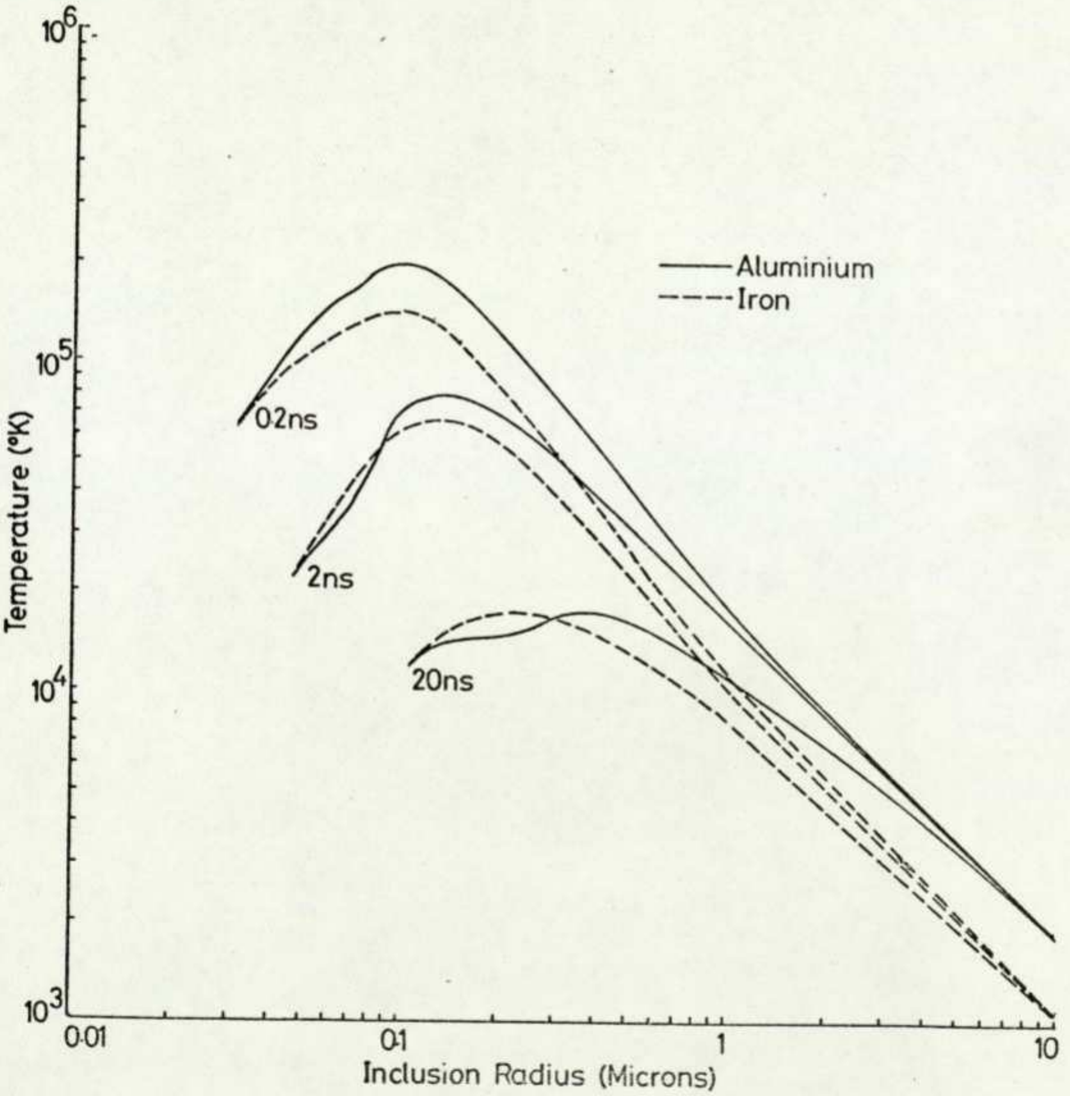

Temperature of Metalic Inclusions in ADP for Constant Input Energy

Fig 7.2

in predicting the stresses needed to cause damage, large errors may be present. To simplify the calculation it is assumed that no phase change occurs. Hopper argues that if a phase change does occur the molten material will be superheated and will form a layer around the inclusion, relieving the stress, this could increase the temperature needed for breakdown by a factor of two he predicts.

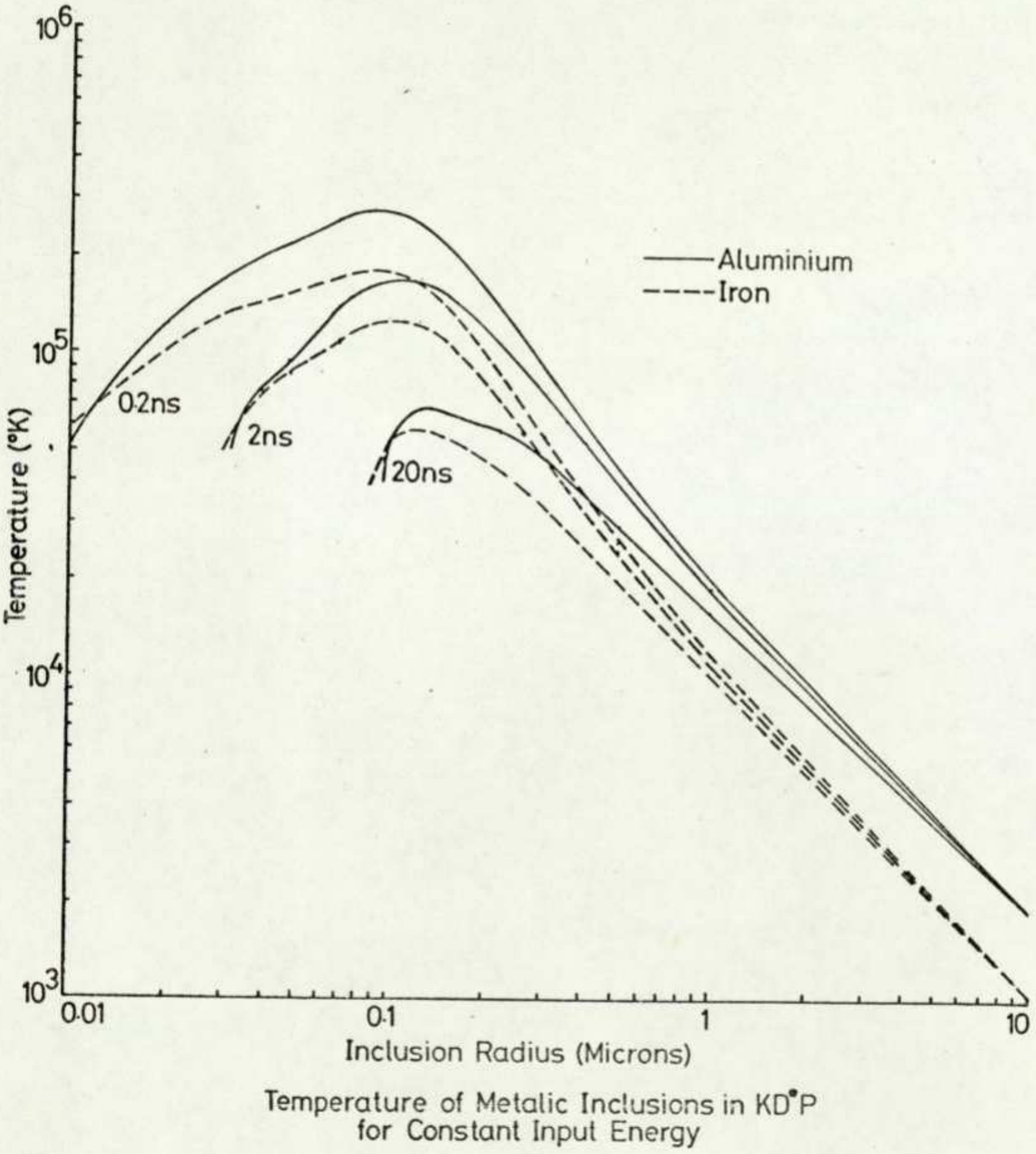

Temperature of Metalic Inclusions in KD*P
for Constant Input Energy

Fig 7.3

Hopper quotes that the maximum stress ϕ_{max} tangential to the inclusion surface is given as

$$\phi_{max} = \frac{6B_iG_h\ {}_iT}{4G_h+3B_i} \qquad 7.17$$

where B_i is the bulk modulus and G_h is the shear modulus. For ADP this reduces to

$$\phi_{max} = 1.4 \times 10^5\ T \quad Nm^{-2}$$

The maximum shear stress for the XDP family is approximately $2 \times 10^9\ Nm^{-2}$ (Christmas(1973)). This is the theoretical maximum and in practice can be much smaller. Assuming a maximum practical shear stress of $5 \times 10^8\ Nm^{-2}$ the temperature needed to cause this stress will be

$$T = 3 \times 10^3\ {}^oK$$

7.3 Pulse length dependence of breakdown.

Allowing a factor of three for the effective stress relief due to the phase change, the temperature needed to cause crystal structure failure would be approximately $10^4\ {}^oK$.

Using this figure as the temperature threshold for damage of an inclusion the results of the computer program used to solve equation 7.16 can be used to plot curves of damage threshold variation with pulse length. The validity of the actual threshold temperature is not important as the variation from pulse to pulse is the information sought from this analysis.

Figure 7.4 gives the resulting power threshold variation with pulse length for ADP and KD*P with inclusions of iron, tin, aluminium and a dielectric with the same thermal properties as the host material but an emissivity of 0.3.

The absolute value of power density is that arrived at using the critical temperature ($10^4\ {}^oK$) and emissivity of the inclusions. These values can shift the curve in the vertical position but will not effect

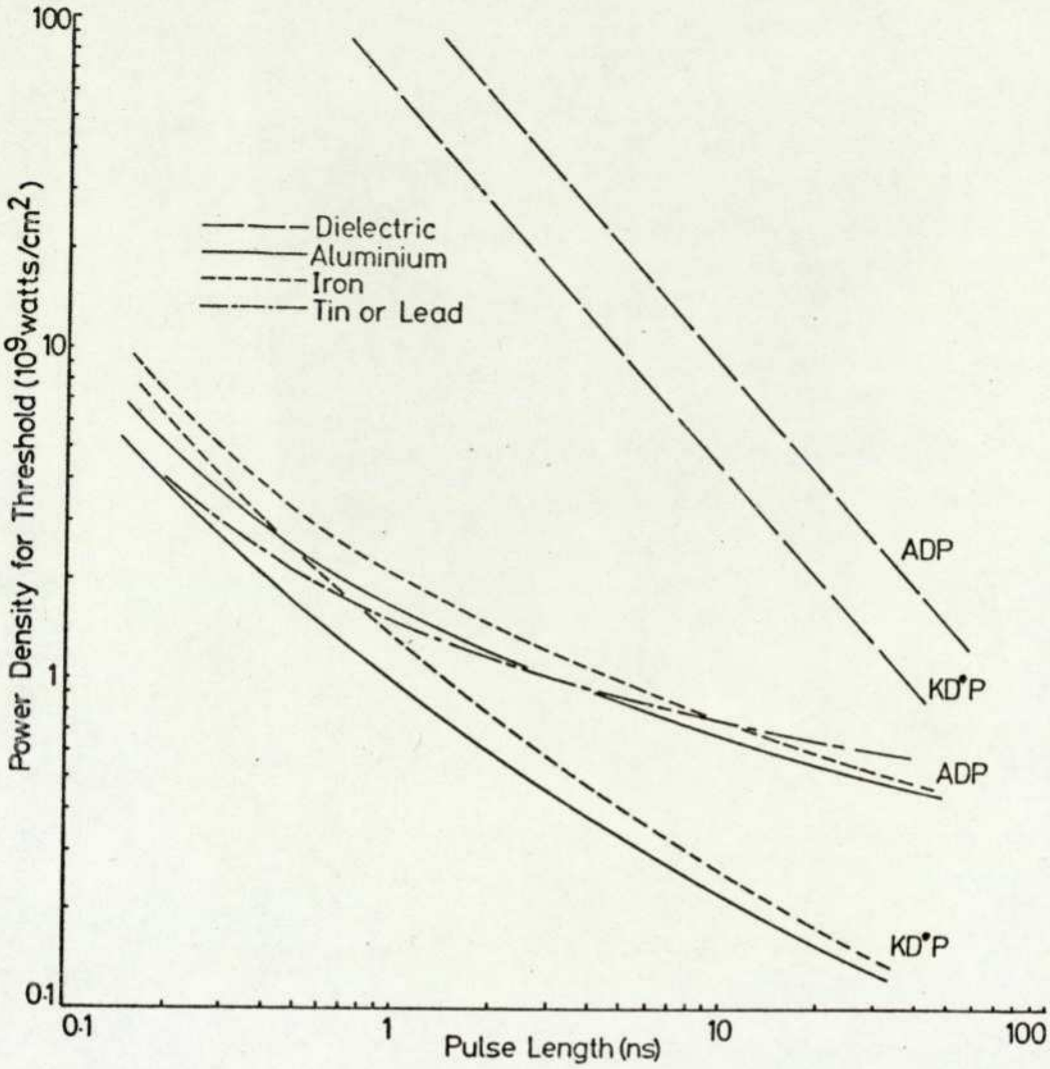

Power Density Threshold verses Pulse Length in ADP and KD*P for Metalic and Dielectric Inclusions

Fig 7.4

the tendencies with pulse length variation. In section 8 these tendencies will be compared with experimentally measured tendencies.

7.4 Size of damage area produced.

Hopper derives an expression for the temperature gradient existing in the bulk material which is produced by the inclusion at high temperatures. If the incident energy is well above threshold he shows that temperatures above the critical temperature can be produced extending well into the bulk material, thus producing damage regions many times the radius of the inclusion itself. Once fracturing takes place around the inclusion, damage in the form of slip planes can extend for great distances into the bulk material.

It is expected however that the damage region produced would have some relation to the inclusion size damaged. This was in fact consistent with experimental results described in section 6.

SECTION 8

DISCUSSION OF RESULS WITH CONCLUSIONS

Introduction.

In this section an attempt is made to link the theoretically predicted pulse length variation of damage threshold to the variations which were obtained experimentally. These tendencies give information as to the composition of the inclusions causing breakdown. This information will be compared with the damage site investigation results revealed by the X-ray fluorescence studies.

The selective properties of the pulse length in relation to inclusion size damaged predicted by the theory will be compared with the actual damage characteristics observed.

This is followed by the overall damage measurement conclusions as well as conclusions resulting from the complete system development.

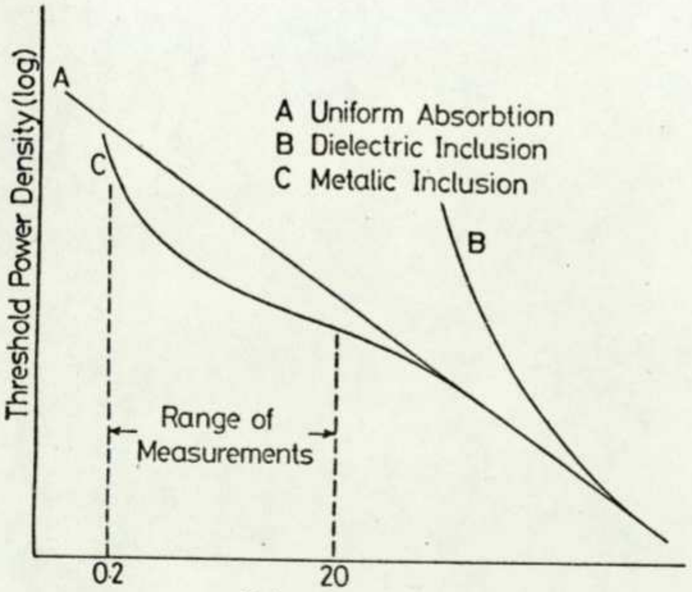

Inclusion Refractive Index Effect on Damage Tendencies

Fig 8·1

8.1 Damage threshold variation with pulse length.

Figure 8.1 summerises the effect of the inclusion refractive index on the pulse length dependence of damage threshold. Curve A represents the trend of an inclusion that absorbs energy across its geometric crossection for all pulse lengths. Curve B represents a real dielectric inclusion which has been compensated for its change in crossectional area relative to the incident energy wavelength. Curve C represents a metalic inclusion which has also been corrected for area crossection. The tendencies of the measured power threshold levels shown in figures 6.1 and 6.3 compare favourably with the low slope of a metalic inclusion, given quantitatively in figure 7.4. ADP has a slope of zero from 20ns to 2.5ns and then increases rapidly from 2.5ns to 300ps. The general shape up to 2.5ns could be that of any of the metals in figure 7.4 for ADP, in particular lead or tin. KD*P has a slope from 20ns to 2.5ns that again corresponds to any of the metals in figure 7.4.

The dramatic increase in slope in ADP from 2.5ns to 300ps is puzzling. This could be due to the fact that no inclusions exist which fall at the peak of the temperature curve for 300ps in ADP, higher powers are needed to increase the temperature of inclusions lower down the curve (figure 7.2) to that of the critical temperature.

The comparison of the 10 micron filtered sample and the 0.3 micron filtered sample of KD*P in section 6.3 supports the arguement that inclusions causing damage are present as discrete inclusions even in the pre grown solution. The results of this experiment imply that absorbing areas such as crystal growth discontinuities and bubbles containing a liquid or gas are not likely to cause damage in KD*P.

The previous experimental evidence suggests that the inclusions causing damage are discrete metalic particles present in the solution from which the crystals are grown.

8.2 Pulse length selection of particle size responsible for damage.

Figures 7.2 and 7.3 illustrate the theoretically predicted maximum temperature variation with pulse length in ADP and KD*P. These curves predict that inclusions in both materials likely to cause damage have diameters from 0.3 microns to 0.1 microns for pulse lengths ranging from 20ns to 200ps. These curves are for metalic inclusions, if the peak temperatures for the same pulse lengths were plotted for a dielectric the range would be wider. In general the shorter the pulse length the smaller the diameter of the inclusion responsible for damage.

These predictions are supported by the experiment described in section 6.4. Using a 20ns pulse in ADP inclusions with diameters no greater than several microns were purposely irradiated. The probability of such an inclusion causing damage was shown to be small. The damage threshold of this sample was approximately equal to that of other samples of ADP. Samples of KD*P with very large inclusions were investigated using the same procedure, again the probability of an inclusion causing damage was small.

The two experimental observations described above support the theoretical prediction that inclusions probably greater than one micron in diameter are not responsible for damage occuring at these pulse lengths using 0.69 micron wavelength radiation.

8.3 Conclusions.

Damage investigation.

Power density thresholds have been measured in several samples of ADP and KD*P at pulse lengths of 20ns, 2.5ns and 300ps.

Damage critera based on the observation of scattered light by the damaged region revealed the ratios of power damage threshold in KD*P as 1:1.8:2.6 and in

ADP as 1:1.05:>4.1 for pulse lengths of 20ns, 2.5ns and 300ps respectively.

Damage at 300ps in ADP was the only non inclusion damage observed at threshold levels, this was the highest threshold value measured and was attributed to the presence of self focusing.

The damaged area produced became smaller as the pulse length was reduced with the appearance of damage in both materials being similar for the same pulse length (except at 300ps).

Several observed factors indicate the presence of discrete metalic inclusions which are introduced before the crystal forms. Investigation of the damaged region shows the presence of a gas under high pressure. Phosphorous was the only element above sodium in atomic weight that could definitely be detected within the damaged region. This presents the remote possibility that discrete fragments of phosphorous or a compounded form could be present in the crystals, as this fits all the observed critera for KD*P.

A technique has been described for measuring the volume density of inclusions responsible for damage, which could be the basis of an analytical instrument used for quality control in the manufacture of the XDP materials.

Laser system.

The production of a controled pulse length reaching a lower limit of 250ps has been made possible by a novel arrangement of a two terminal laser triggered spark gap and an ultra-fast KD*P pockels cell. Both these devices were developed specifically for this work. The pockels cell has an electrical risetime of 74ps. Measured optical risetimes are in the order of 150ps. These are limited by the laser triggered spark gap used to drive the pockels cell. The spark gap has produced electrical risetimes of approximately 180ps and a system is suggested in the next section of this work which could appreciably reduce this risetime.

Pockels cell electrical risetimes were measured on a Hewlett Packard time domain reflectometer, and optical risetimes were measured with a streak camera. The streak camera was used to calibrate the ITL vacuum photodiode for various pulse lengths so that measurements could be made conveniently at the shorter pulse lengths.

SECTION 9

SUGGESTIONS FOR FURTHER WORK

Further work relevant to this thesis falls into two main areas, firstly the refinement of the laser system and secondly a damage threshold investigation including both particle identification and extended threshold measurements.

In the field of damage measurements, the method of statistical analysis described in this thesis could be applied to other electro-optic materials for surface damage investigation as well as that for bulk damage. A thorough investigation of XDP materials at even shorter pulse lengths could reveal important aspects of self focusing and avalanche breakdown as it is expected that inclusion damage would not occur in the low picosecond region. This has been shown in ADP during the course of this work.

Although it seems likely that the inclusions responsible for damage are metalic a thorough investigation and identification is needed. The possibility of a conducting inclusion consisting of the pre-grown solution (which is strongly acidic) adds to the complexity of the energy absorption calculations. A more thorough analysis could be carried out by extended investigation of damaged and undamaged regions of the cleaved crystal using the scanning electron microscope and X-ray fluorescence analysis. This instrument is ideally suited to this task as its sensitivity is extremly high being limited by the finite area under analysis, this can be as small as one hundredth of one micron.

The laser system could be extended to shorter pulse lengths in two ways, firstly a mode locked laser could be used to generate picosecond pulses as described in section 3.2, alternatively the switching arrangement used with the Q-switched pulse in this work could be extended, a basic limit exists with the latter approach determined by the pockels cell itself. It is believed that optical pulses shorter than around 20ps are impossible due to the light contained in the pockels cell.

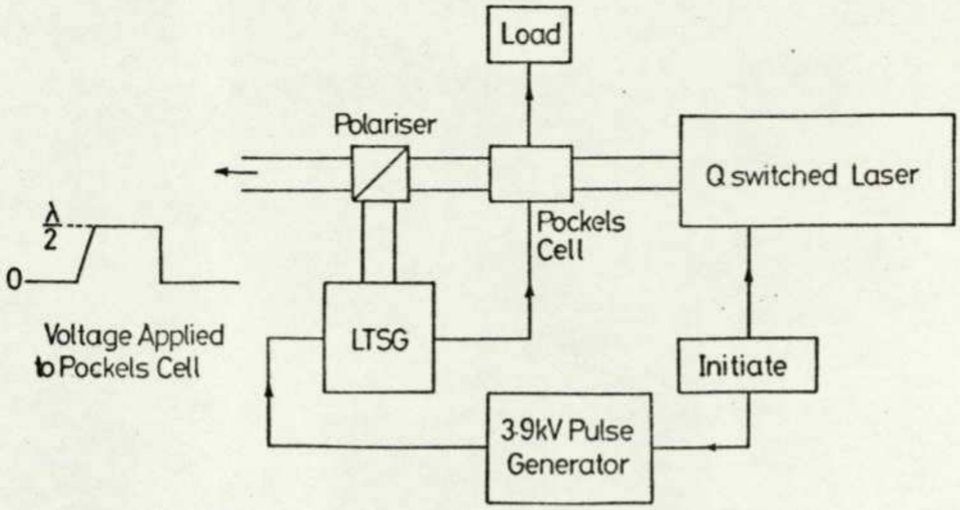

LTSG Over Voltage Operation

Fig 9·1

With the existing pockels cell it is thought that optical risetimes in the order of 100ps are possible, the limiting factor is then the laser triggered spark gap. Section 3.7 describes several ways by which the risetime can be reduced. One method not discussed, which could reduce the risetime considerably, involves overcomming the limitation of the maximum DC voltage gradient the gap can withstand. It is known that a gap can 'hold off' a considerable overvoltage for a very short time. Figure 9.1 illustrates a system which for the gap used in this work could produce risetimes much faster than those obtained previously. The half wave voltage of the pockels cell is applied to the spark gap at a time no less than Tns before the LTSG is due to be triggered. This time T is the sum of the electrical delay from the LTSG to the pockels cell and half the total Q-switched pulse length. This would be typically about 40ns. The short time this voltage is present at the LTSG before it was triggered would allow a much higher electrical stress to be applied to the gap, and according to equation 3.11 or 3.17 this would result in a shorter risetime. The pre-pulse could be applied to the LTSG with a krytron or hydrogen thyratron.

For risetimes much faster than those measured in this work the modification to the streak camera suggested in section 5.6 would have to be carried out to increase its streak rate and dynamic range.

It is suggested that a detailed investigation be made of the system described in section 5.6 for driving the streak camera from the LTSG. This would result in a very well synchronized and exceptionally fast streak rate without the inconvenience of the high frequency, and by necessity, high power oscillator.

SECTION 10

ACKNOWLEDGEMENTS

I wish to express my appreciation to Dr A.W.Palmer for many helpful discussions and constant encouragement during the course of this work.

I am indebted to [redacted] [redacted], of Electro-optic Developments Ltd. for numerous helpful suggestions as well as supplying and fabricating many of the samples used in this work.

Thanks are also due to [redacted] [redacted], [redacted] [redacted] [redacted] of the electrical engineering workshop for their superb workmanship which is evident in the construction of the pockels cells and laser triggered spark gaps.

Special appreciation is due to [redacted] [redacted], without her support and encouragement this work would not have been possible.

SECTION 11 REFERENCES

AIRTRON, Data sheet No RB/1969, Litton Industries.

ALCOCK A.J. and RICHARDSON M.C. Optics Comm. Vol.2 No.2 1970 p65.

BARAFF G.A. Phys. Rev. 128 1962 p2507.

BASS M. and BARRET H. IEEE QE-8 No.3 1972 p338.

BENNET H.S. J. Appl. Phys. Vol.42 No.2 1971 p619.

BLISS E.S. Appendix, NBS Special Pub. No.435 1975 p105.

BORN M. and WOLF E. 4th Ed., Principles of Optics, Pergaman 1970.

CARSLAW and JAEGER Conduction of Heat in Solids, Oxford 1950

CHIAO R.Y. TOWNS C.H. and STOICHEFF B.P. Phys. Rev. Lett. No.12 1964 p592.

CHIAO CERMIRE and TOWNS Phys. Rev. Lett. Vol.13 No.15 1964 p479.

CHRISTMAS T.M. WILDEY C.J. and LEY J.M. Proc. IEE No.117 1970 p479.

CHRISTMAS T.M. Ph.D Thesis, The City University, 1973.

CHU B. Laser Light Scattering, Academic Press 1974.

CHYNOWETH A.G. Phys. Rev. No.109 1959 p1537.

EDWARDS J.G. J. Phys.E Vol.3 1970 p567.

EDWARDS J.G. J. Phys.E Vol.2 1969 p1126.

EDWARDS J.G. Private communication 1976.

FLETCHER R.C. Phys. Rev. Vol.76 No.10 1949 p1501.

FRADIN YABLONOVITCH and BASS Appl. Opt. Vol.12 1973 p700.

GUNSTONE M.A.R. Microwave Transmission Line Impedance Data, Van Nostrand Reinhold

HELLWORTH D.W. Damage in Laser Materials, NBS Special Publication No.341 p67.

HERCHER M. J. Opt. Soc. America No.54 1964 p563.

HESS H. J.Phys.D Vol.8 1975 p685.

Von HIPPLE Dielectric Materials and Applications, Wiley 1954.

HOPPER R.W. and UHLMAN D.R. J.Appl.Phys. Vol.41 No.10 1973 p4023.

HOWELL A.H. Trans.Amer.Inst.Elec.Engineers No.58 1939 p193.

IRELAND C.L.M. J.Phys.E Vol.8 1975 p1007.

KAY and WALDERMAN J.Appl.Phys. No.36 1965 p1319.

KERR E.L. Phys.Rev.A Vol.4 No.3 1971 p1195.

KOGELNIK H. and LI T. Appl.Opt. No.10 Vol.5 1966.

LASERMETRIC Data sheet, Model 1080 Pockels cell.

LEITH I.S. Laser Hazards and Safety Measures, Laser Applications Conference, Ian Clunies Ross Memorial Foundation, Melb. Australia 1973

LENGYEL B. Lasers, Wiley 1971.

LEY J.M. Private communication 1977.

Von der LINDE D. BERNECKER O. and LAUBEREAU A. Opt.Comm. Vol.2 No.5 1970 p215.

MAIMAN T.H. Phys.Rev. No.123 1961 p1145.

MEEK and CRAGGS Electrical Breakdown of Gases, Oxford 1953.

MICHON M. GUILLET H. GOFF D. and RAYNAUD S. J.Phys.E Vol.40 No.2 1969 p263.

PALMER A.W. Ph.D Thesis, The City University 1973.

QUELLE F.W. Am.Soc.Testing and Materials, Special Publication No.469 1969 p149.

RAETHER H. see REES J.A.

REES J.A. Electrical Breakdown in Gases, Macmillan 1973, paper by RAETHER H. 1939.

REES J.A. Electrical Breakdown in Gases, Macmillan 1973, paper by ROGOWSKI W. 1928.

REES J.A. Electrical Breakdown in Gases, Macmillan 1973, paper by TOWNSEND J.S. 1910.

ROGOWSKI W. and RENGIER H. Arch.Elektrotech No.16 1926 p73.

ROGOWSKI W. see REES J.A.

ROSS D. Lasers Light Amplifiers and Oscillators AP 1969.

SHOCKLEY W. Czech.J.Phys. No.1311 1961 p81.

SORENSEN T.P. and RISTIC V.M. J.Appl.Phys. Vol.48 No.1 1977 p114.

SPARKS M. and DUTHLER C.J. J.Appl.Phys. Vol.44 No.7 1973 p3138.

SPARKS M. Laser Induced Damage in Optical Materials, NBS Special Publication NO.435 1975 p331.

STEEL E.L. Optical Lasers in Electronics, Wiley 1968.

STEINMETZ L.L. POUTIOT T.W. and JOHNSON B.C. Appl.Opt. Vol.12 No.7 1973 p1468.

TOWNSEND J.S. see REES J.A.

TRUMP J.G. CLOUD R.W. MANN J.G. and HANSON E.P. Elec.Eng. No.69 1950 p196.

VITKOV M.G. Opt.Spect. No.24 1968 p480.

VITKOV M.G. Opt.Spect. No.27 1969 p185.

WASSERMAN A. Appl.Phys.Lett. No.10 1967 p132.

WILDEY J. Ph.D Thesis, The City University 1973.

YARIV A. Quantum Electronics, Wiley 1967.

ZEIER O. Ann.Phys.Lpz. No.14 1932 p415.

ZEREV G.M. MIKHAILOVA T.M. and POSHKOV V.A. Sov.Phys.JETP No.26 1968 p1053.

ZERNIKE F. MIDWINTER J. Applied non-linear Optics, Wiley 1973.

SECTION

12

APPENDICES

Introduction.

Appendix 1 contains the derivation of the equation used in this work to predict the temperature increase of an inclusion imbeded in the bulk of a host material. This work extends that of Hopper and Uhlman(1973) to cover an infinite range of physical properties for the host material and inclusion.

Appendix 2 contains the circuit diagrams of the Krytron pockels cell driver arranged for both Q-switching and pulse chopping, a block diagram of this system is given on page 41 of the text.

In appendix 3 engineering drawings of the single terminal and two terminal laser triggered spark gaps are given, these should be read in conjunction with each other. A drawing of the new pockels cell is also given in this appendix.

The computer program written to give a graphical solution of equation 7.16 (derived in appendix 1) is given in appendix 4. This program uses a standard library function for the error function (erfc) which was labeled (S15ADF(X,Y)) on the computer used for the analysis.

Appendix 5 contains copies of published papers.

Appendix 1. Derivation of the inclusion temperature equation.

When solving the heat diffusion equation, certain assumptions are made. Firstly the incident radiation is assumed to be of rectangular shape. Secondly the heat loss by radiation is assumed to be small compared to the heat loss by conduction. This is valid for the duration of the pulse, while the radiation is small, also the thermal resistance between the inclusion and bulk material is very low because the large expansion of the inclusion relative to the bulk ensures good physical contact at all times. Thirdly the inclusion is assumed to be perfectly conducting.

For larger inclusion diameters the area of the inclusion for absorption will be considered as the geometrical area, for smaller diameters a factor will be introduced later to account for this assumption.

The following list gives a definition of all terms used in the analysis.

C_V volume heat capacity cal cm^{-3} $^oK^{-1}$
C_m mass heat capacity cal gm^{-1} $^oK^{-1}$
D thermal diffusivity $(k/C_m\rho)$
ϵ_λ emissivity at wavelength λ
ρ density gm cm^{-3}
J flux level Watts/cm^2
k thermal conductivity
R radius cm
t time ns
T temperature ^oK

subscripts; i inclusion
g host material

The final equation for the temperature of an inclusion subject to the conditions stated above is quoted by Hopper et al(1973), the derivation of this equation will be included here as it together with its modified form describe the temperature for any value of inclusion and bulk material physical properties.

The quantity of heat absorbed by the inclusion with no heat conduction from the inclusion to the host material is

$$\epsilon_\lambda J\pi R^2\, t = ht$$

The quantity of heat needed to give a temperature increase of T^oK is

$$\frac{4}{3}\, R^3 C_v T = CT$$

equating these heat quantities results in a temperature increase of

$$T = \frac{3\,\epsilon_\lambda Jt}{4C_{vi}R_i} \quad {}^oK$$

This indicates that as the radius approaches zero the temperature of the inclusion approaches infinity. If heat conduction from the inclusion to the host material is taken into account an expression for temperature can be derived using the heat conduction equations given by Carslaw and Jaeger(1950)

These equations are

$$C\frac{dT}{dt} + k_g\left(-\frac{dv}{dr}\right)_R 4\pi R^2 = h \qquad 7.1$$

where T = 0 at t = 0 for the inclusion

and $$\frac{dv}{dt} = D_g\left(\frac{dv}{dr} + \frac{2\,dv}{r\,dr}\right) \qquad 7.2$$

for the glass, $v = T$ at $r = R$ for $t > 0$.

Using Laplace transforms

$$Cs\bar{T} - a\frac{d\bar{v}}{dr_R} = \frac{h}{s} \qquad 7.3$$

where $a = 4\pi R^2 k_g$

and $$s\bar{v} = D_g\left(\frac{d^2\bar{v}}{dr^2} + \frac{2}{r}\frac{d\bar{v}}{dr}\right) \qquad 7.4$$

where $\bar{v} = \bar{T}$ at $r = R$

let $u = vr$, that is $\bar{u} = \bar{v}r$

and substituting into equations 7.3 and 7.4

then $$Cs\bar{T} - a\left(\frac{1}{R}\frac{d\bar{u}}{dr} - \frac{\bar{u}}{R^2}\right) = \frac{h}{s} \qquad 7.5$$

and $$s\bar{u} = D_g\,\frac{d^2\bar{u}}{dr^2}$$

at $r = R$, $\bar{u} = R\bar{T}$

then $$\frac{d^2\bar{u}}{dr^2} - \frac{s}{D_g}\bar{u} = 0$$

This has a solution of the form

$$\bar{u} = A\exp(-\sqrt{\tfrac{s}{D_g}}\,r) + B\exp(\sqrt{\tfrac{s}{D_g}}\,r)$$

since $\nu \to 0$ as $r \to \infty$ then $\nu \to 0$ as $r \to \infty$ therefore $B = 0$

thus $$\bar{u} = A\exp(-r\sqrt{\tfrac{s}{D_g}})$$

substituting $r\bar{T}$ for $\bar{u}$

$$R\bar{T} = A\exp(-R\sqrt{\tfrac{s}{D_g}}) \qquad \text{at } r = R$$

therefore $$\bar{u} = R\bar{T}\exp(-\sqrt{\tfrac{s}{D_g}}\,(r-R)) \qquad 7.6$$

using this equation in the inclusion equation (7.3)

$$Cs\bar{T} - a(\tfrac{1}{R}(-\sqrt{\tfrac{s}{D_g}}\,R\bar{T}) - \tfrac{1}{R^2}R\bar{T}) = \frac{h}{s}$$

simplifying this expression

$$\bar{T}(Cs + a\sqrt{\tfrac{s}{D_g}} + \tfrac{a}{R}) = \frac{h}{s}$$

therefore $$\bar{T} = h/(s(Cs + a\sqrt{\tfrac{s}{D_g}} + \tfrac{a}{R})) \qquad 7.7$$

The inverse Laplace transform of equation 7.7 is

$$T = \frac{h}{2\pi i}\int_{r-i\infty}^{r+i\infty} \exp(st)ds/(s(Cs + a\sqrt{\tfrac{s}{D_g}} + \tfrac{a}{R})) \qquad 7.8$$

The integral in equation 7.8 is calculated such that no singularities occur within the contour of integration.

let $\sqrt{\frac{s}{D_g}} = \sigma$ then $s = D_g\sigma^2$

The roots of the integral in equation 7.8 occur at points where

$$CD_g\sigma^2 + a\sigma + \frac{a}{R} = 0$$

these points are:

$$\sigma = \frac{-a}{2D_gC} \pm \frac{1}{2CD_g}\sqrt{a^2 - \frac{4CD_ga}{R}}$$

$$= \frac{-a}{2D_gC} \pm \sqrt{\frac{a^2}{4(CD_g)^2} - \frac{a}{RCD_g}} \qquad 7.9$$

the roots are real if $\frac{a}{4D_gC} > \frac{1}{R}$ that is if $\frac{aR}{CD_g} > 4$

but $\frac{aR}{CD_g} = \frac{3C_{vg}}{C_{vi}}$, let $\frac{3C_{vg}}{C_{vi}} = q$

then $q > 4$ for real roots.

rearranging equation 7.9

$$2\sigma R = -q \pm \sqrt{q(q-4)}$$

let $m = (q(q-4))^{\frac{1}{2}}$

then
$$\sigma = \frac{-q \pm m}{2R} \qquad 7.10$$

From equation 7.7

$$\bar{T} = h/(s(CD_g\sigma^2 + a\sigma + \tfrac{a}{R}))$$

using the two values of σ from equation 7.10

$$\alpha = \frac{-q - m}{2R} \qquad \beta = \frac{-q + m}{2R}$$

we have

$$\bar{T} = [h/\ CD_g(\alpha-\beta)]\left(\frac{1}{s(\sigma-\alpha)} - \frac{1}{s(\sigma-\beta)}\right) \qquad 7.7a$$

taking the inverse Laplace transform of equation 7.7a

$$T = \frac{h}{CD_g(\alpha-\beta)}\Big[\Big(\frac{1}{|\alpha|} - \frac{1}{|\alpha|}\exp(\alpha^2D_gt)\,\mathrm{erfc}(|\alpha|\sqrt{D_gt})$$
$$- \frac{1}{|\beta|} - \frac{1}{|\beta|}\exp(\beta^2D_gt)\,\mathrm{erfc}(|\beta|\sqrt{D_gt})\Big]$$

now substituting the values of α and β

$$T = \frac{hR}{CD_gm}\Big[\frac{2R}{q-m} - \frac{2R}{q-m}\exp\Big(\big(\frac{q-m}{2R}\big)^2D_gt\Big)\,\mathrm{erfc}\Big(\frac{q-m}{2R}\sqrt{D_gt}\Big)$$
$$- \frac{2R}{q+m} + \frac{2R}{q+m}\exp\Big(\big(\frac{q+m}{2R}\big)^2D_gt\Big)\,\mathrm{erfc}\Big(\frac{q+m}{2R}\sqrt{D_gt}\Big)\Big]$$

but $h=\epsilon_\lambda J\pi R^2$ and $C=\frac{4}{3}\pi R^3 C_{vi}$. Substituting for h and C and removing 2R from the square brackets leaves

$$T = \frac{3\,\epsilon_\lambda JR}{2C_{vi}D_g m}\left[\frac{1}{q-m}\left(1-\exp\left(\left[\frac{q-m}{2R}\right]^2 D_g t\right)\mathrm{erfc}\left(\frac{q-m}{2R}\sqrt{D_g t}\right)\right) - \frac{1}{q+m}\left(1-\exp\left(\left[\frac{q+m}{2R}\right]^2 D_g t\right)\mathrm{erfc}\left(\frac{q+m}{2R}\sqrt{D_g t}\right)\right)\right] \quad 7.11$$

This equation is the final result given by Hopper and Uhlman.

The condition that m is real implies that q is greater than 4

$$\text{therefore} \quad \frac{3C_{vg}}{C_{vi}} > 4 \qquad 7.12$$

A possible inclusion material is copper with $C_v = 0.817$ if ADP is assumed to be the host material then $C_{vg} = 0.47$ then from equation 7.12

$\frac{3C_{vg}}{C_{vi}} = 1.72$ which is less than 4 and means that the roots of the conduction equation are complex Equation 7.11 cannot be used in the form given.

The modified form of equation 7.11 can be obtained by substituting im for m in equation 7.11 $(i = \sqrt{-1})$ Equation 7.11 becomes,

$$T = \frac{3\,\epsilon_\lambda JR}{2C_{vi}D_g im}\left[\frac{1}{q-im}\left(1-\exp\left(\left(\frac{q-im}{2R}\right)^2 D_g t\right)\mathrm{erfc}\left(\frac{q-im}{2R}\sqrt{D_g t}\right)\right) - \frac{1}{q+im}\left(1-\exp\left(\left(\frac{q+im}{2R}\right)^2 D_g t\right)\mathrm{erfc}\left(\frac{q+im}{2R}\sqrt{D_g t}\right)\right)\right]$$

The square brackets contain the difference between a complex number and its conjugate which is equal to twice the value of the conjugate, therefore,

$$T = \frac{3\,\epsilon_\lambda JR}{C_{vi}D_g m}\,\mathcal{I}m\,\frac{1}{q-mi}\left[1-\exp\left(\left(\frac{q-im}{2R}\right)^2 D_g t\right)\mathrm{erfc}\left(\frac{q-im}{2R}\sqrt{D_g t}\right)\right] \quad 7.13$$

To find an expression for the complex exponential exp(z) where

$$z = x + iy$$

The form of equation 7.13 is

$$\exp(z^2) = \exp(x^2 - y^2 + 2ixy)$$
$$= \exp(x^2 - y^2)(\cos 2xy + i\sin 2xy)$$

Let $\frac{3\epsilon\lambda JR}{C_{vi}D_g m} = A$, multiply top and bottom of equation 7.12 by q+im and apply the expression for $\exp(z^2)$

$$T = A\,\mathcal{I}m\,\frac{q+im}{q+m}\left[1-\exp\left(\frac{q^2-m^2}{4R^2}D_g t\right)\left(\cos\left(\frac{qm}{2R^2}D_g t\right)-i\sin\left(\frac{qm}{2R^2}D_g t\right)\right)\operatorname{erfc}\left(\frac{q-im}{2R}\sqrt{D_g t}\right)\right]$$

rearranging terms

$$\frac{T}{A} = \frac{m}{q^2 + m^2} - \mathcal{I}m\left[\exp\left(\frac{q^2-m^2}{4R^2}D_g t\right)\frac{q+im}{q^2+m^2}\left(\cos\left(\frac{qm}{2R^2}D_g t\right) - i\sin\left(\frac{qm}{2R^2}D_g t\right)\right)\operatorname{erfc}\left(\frac{q-im}{2R}\sqrt{D_g t}\right)\right] \qquad 7.14$$

The expression for erfc(z) = 1-erf(z) for a complex function z = x+iy is obtained from mathematical handbooks as

$$\operatorname{erfc}(z) = \operatorname{erfc}(x) - \frac{2}{\sqrt{\pi}}\exp(-x^2)\int_0^y \exp(\delta^2)\sin 2x\delta\, d\delta$$
$$-\frac{2}{\sqrt{\pi}}i\exp(-x^2)\int_0^y \exp(\delta^2)\cos 2x\delta\, d\delta$$

Using this relationship equation 7.14 becomes

$$\frac{T}{A} = \frac{m}{m^2+q^2} - \frac{\exp\left(\frac{q^2-m^2}{4R^2}D_g t\right)}{q^2 + m^2}\; m\cos\theta - q\sin\theta\left(\operatorname{erfc}\left(\frac{q\sqrt{D_g t}}{2R}\right) - \frac{2}{\pi}\exp\left(\frac{-q^2 D_g t}{4R^2}\right)\right.$$
$$\int_0^{-\frac{m\sqrt{D_g t}}{2R}} \exp(\delta^2)\sin\left(q\frac{\sqrt{D_g t}}{2R}\delta\, d\delta\right) + (q\cos\theta + m\sin\theta)$$
$$\left(\frac{-2}{\pi}\exp\left(-\frac{q^2 D_g t}{4R^2}\right)\int_0^{\frac{m\sqrt{D_g t}}{2R}} \exp(\delta^2)\cos\left(\frac{q\sqrt{D_g t}}{2R}\delta\, d\delta\right)\right. \qquad 7.15$$

where $\theta = \frac{qmD_g t}{2R}$. Let $\sin\alpha = \frac{m}{\sqrt{q^2+m^2}}$ and $\cos\alpha = \frac{q}{\sqrt{q^2+m^2}}$

equation 7.15 will simplify to

$$\frac{T}{A} = \frac{m}{q^2+m^2} + \frac{\exp(\frac{q^2-m^2}{2R^2} D_g t)}{\sqrt{q^2 + m^2}} \left[-\sin(\theta-\alpha)\operatorname{erfc}(\frac{q\sqrt{D_g t}}{2R}) - \frac{2}{\sqrt{\pi}} \exp(\frac{-q^2 D_g t}{4R^2}) \int_0^{\frac{m\sqrt{D_g t}}{2R}} \exp(\delta^2)\cos(\frac{q\sqrt{D_g t}}{R}\delta + \theta - \alpha)\, d\delta \right]$$

multiplying by A and substituting for θ,

$$T = \frac{3\,\epsilon_\lambda JR}{C_{vi} D_g m} \left[\frac{m}{q^2+m^2} + \frac{\exp(\frac{q^2-m^2}{4R^2} D_g t)}{\sqrt{q^2 + m^2}} \sin(\frac{qmD_g t}{2R^2} - \alpha)\operatorname{erfc}(\frac{qD_g t}{2R}) - \frac{2}{\sqrt{\pi(q^2+m^2)}} \exp(\frac{-m^2 D_g t}{4R^2}) \int_0^{\frac{m\sqrt{D_g t}}{2R}} \exp(\delta^2)\cos(\frac{q\sqrt{D_g t}}{R}\delta - \frac{qmD_g t}{2R^2} + \alpha)\, d\delta \right]$$

noting the values of $\sin\alpha$ and $\cos\alpha$ this equation becomes

$$T = \frac{3\,\lambda JR}{mC_{vi} D_g} \left[\frac{m}{q^2+m^2} + \frac{\exp(\frac{q^2-m^2}{4R^2} D_g t)}{\sqrt{q^2 + m^2}} (\sin(\frac{qmD_g t}{2R^2}) \frac{q}{q^2+m^2} - \cos(\frac{qmD_g t}{2R^2}) \frac{m}{\sqrt{q^2+m^2}}) \operatorname{erfc}(\frac{q\sqrt{D_g t}}{2R}) - \frac{2}{\sqrt{\pi(q^2+m^2)}} \exp(\frac{-m^2 D_g t}{4R^2}) \int_0^{\frac{m\sqrt{D_g t}}{2R}} \exp(\delta^2)\ \cos(\frac{q\sqrt{D_g t}}{R}\delta - \frac{qmD_g t}{2R^2}) \frac{q}{\sqrt{q^2+m^2}} - \sin(\frac{q\sqrt{D_g t}}{R}\delta - \frac{qmD_g t}{2R^2}) \frac{m}{\sqrt{q^2+m^2}})\, d\delta \right] \qquad 7.16$$

Equation 7.16 is the equation specifying the temperature of an inclusion with radius R and heat capacity C_{vi} within a host material of heat capacity C_{vg} and diffusivity D_g when exposed to radiation of J joules and pulse duration of t seconds.

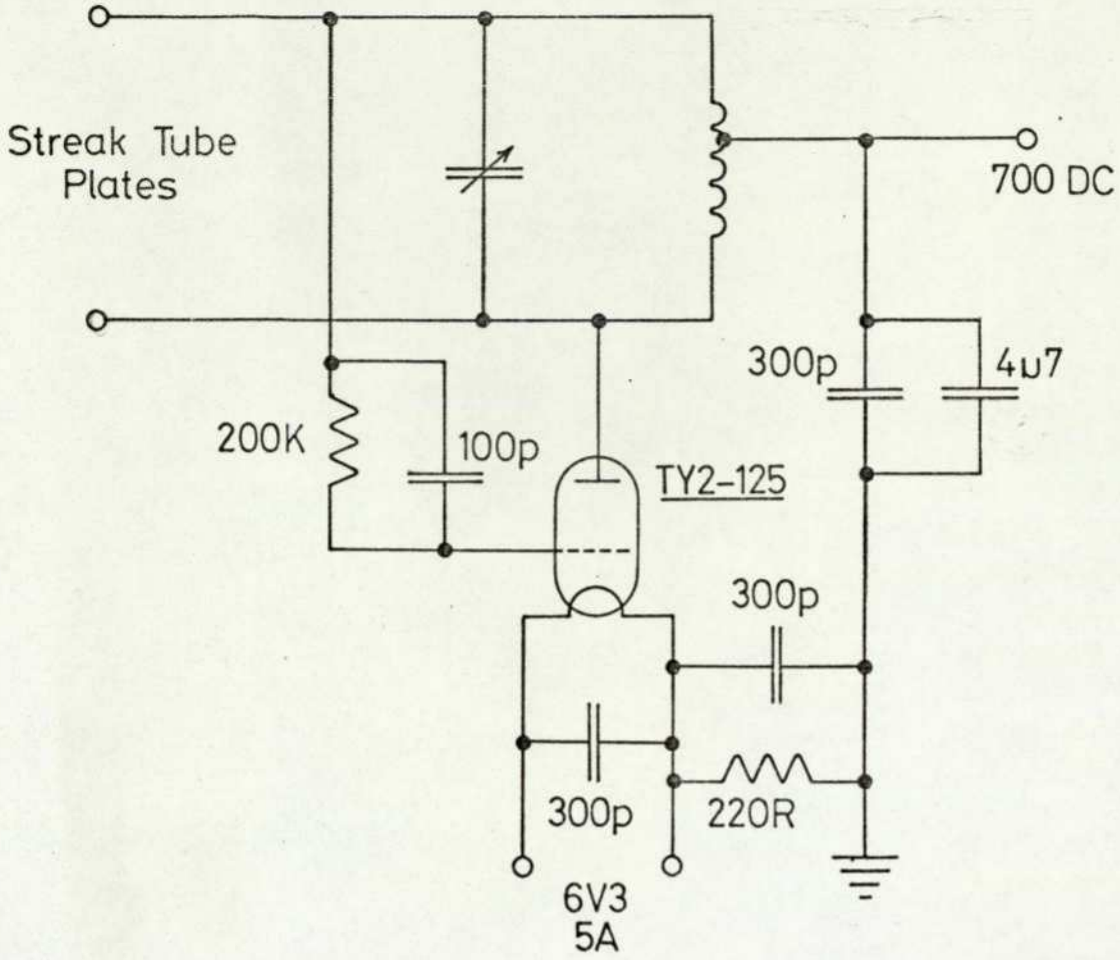

30MHz Streak Camera Oscillator

Appendix 2a

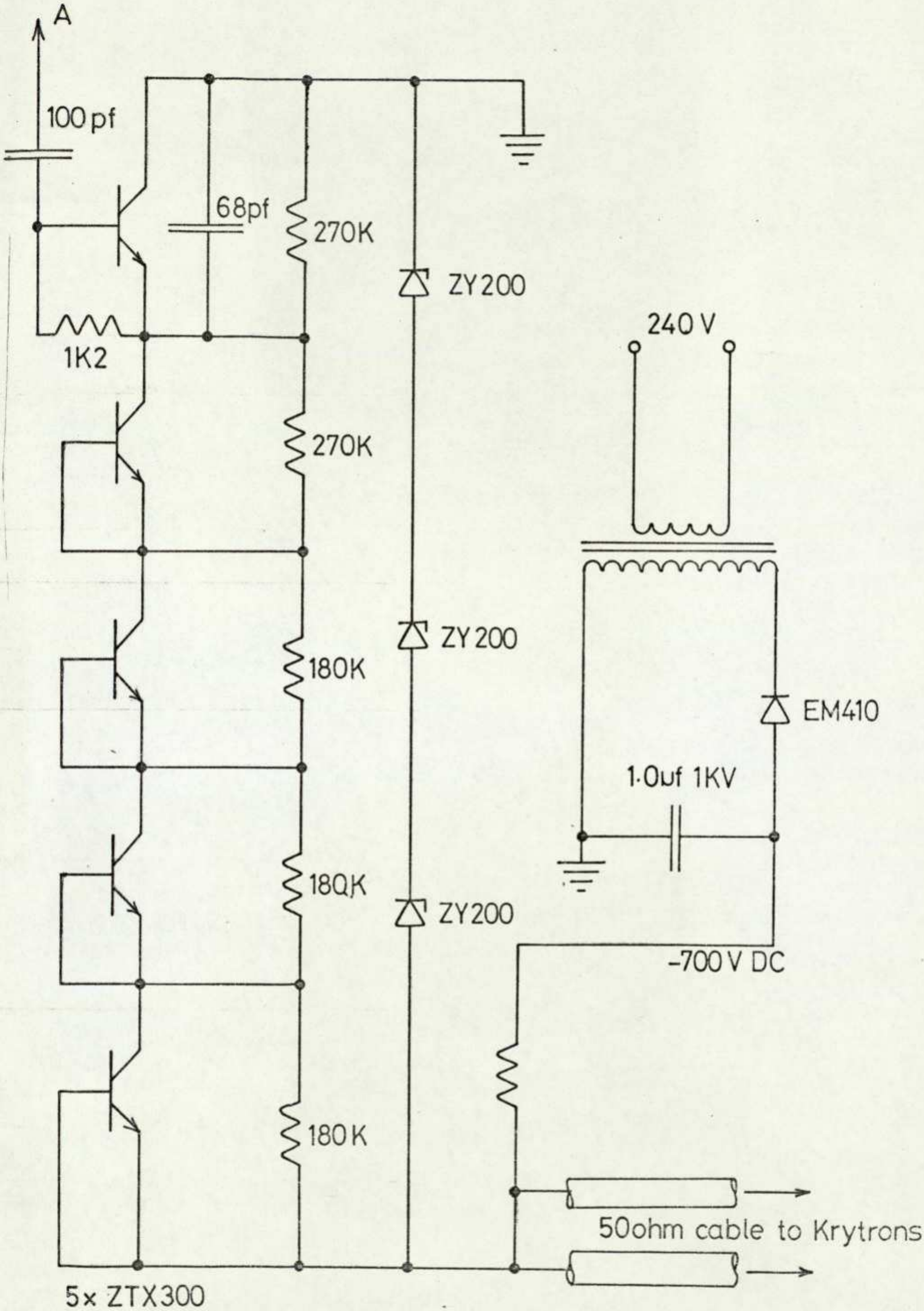

Appendix 2b 700 V Trigger Circuit

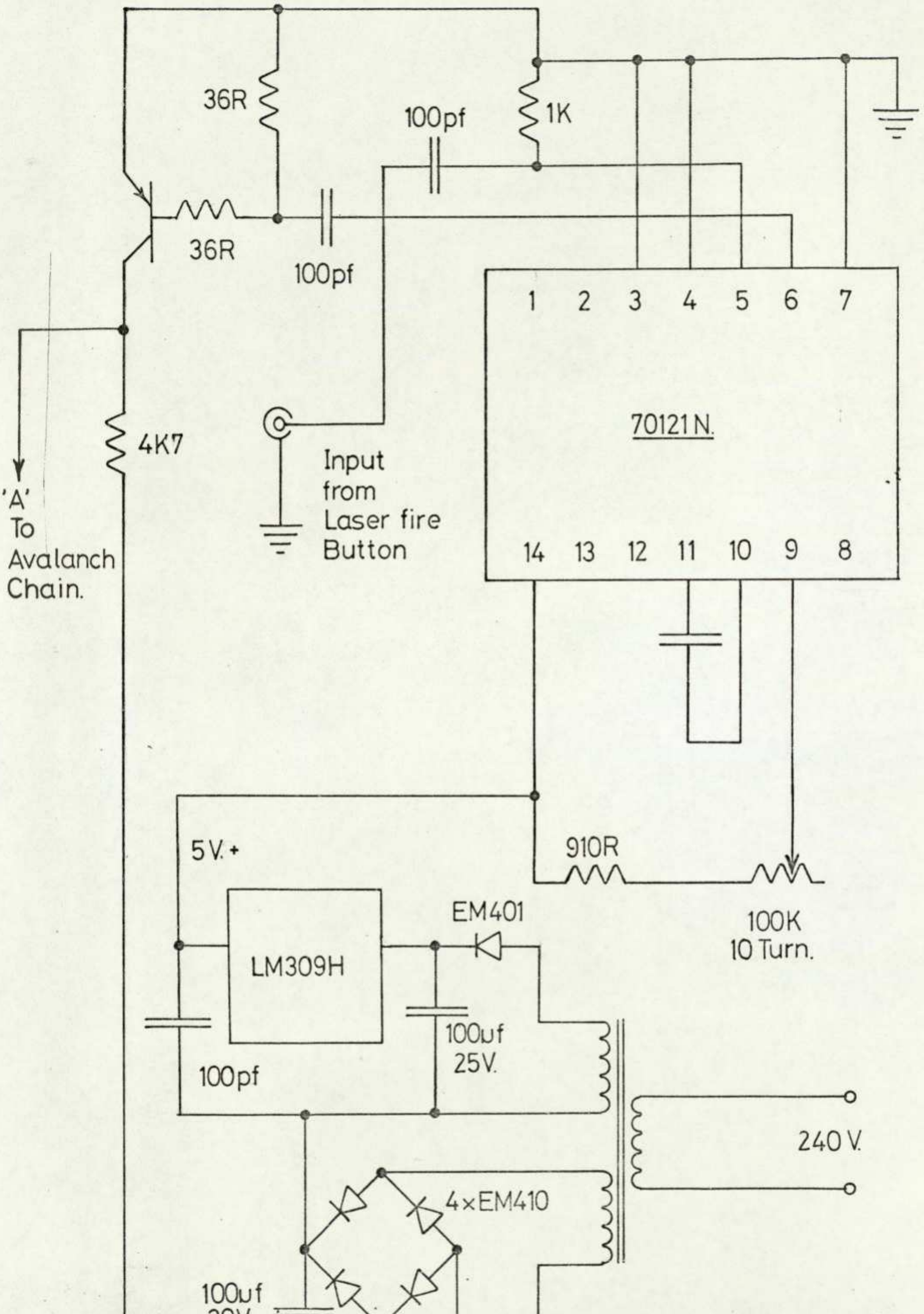

Appendix 2c 0-5mS Delay Circuit.

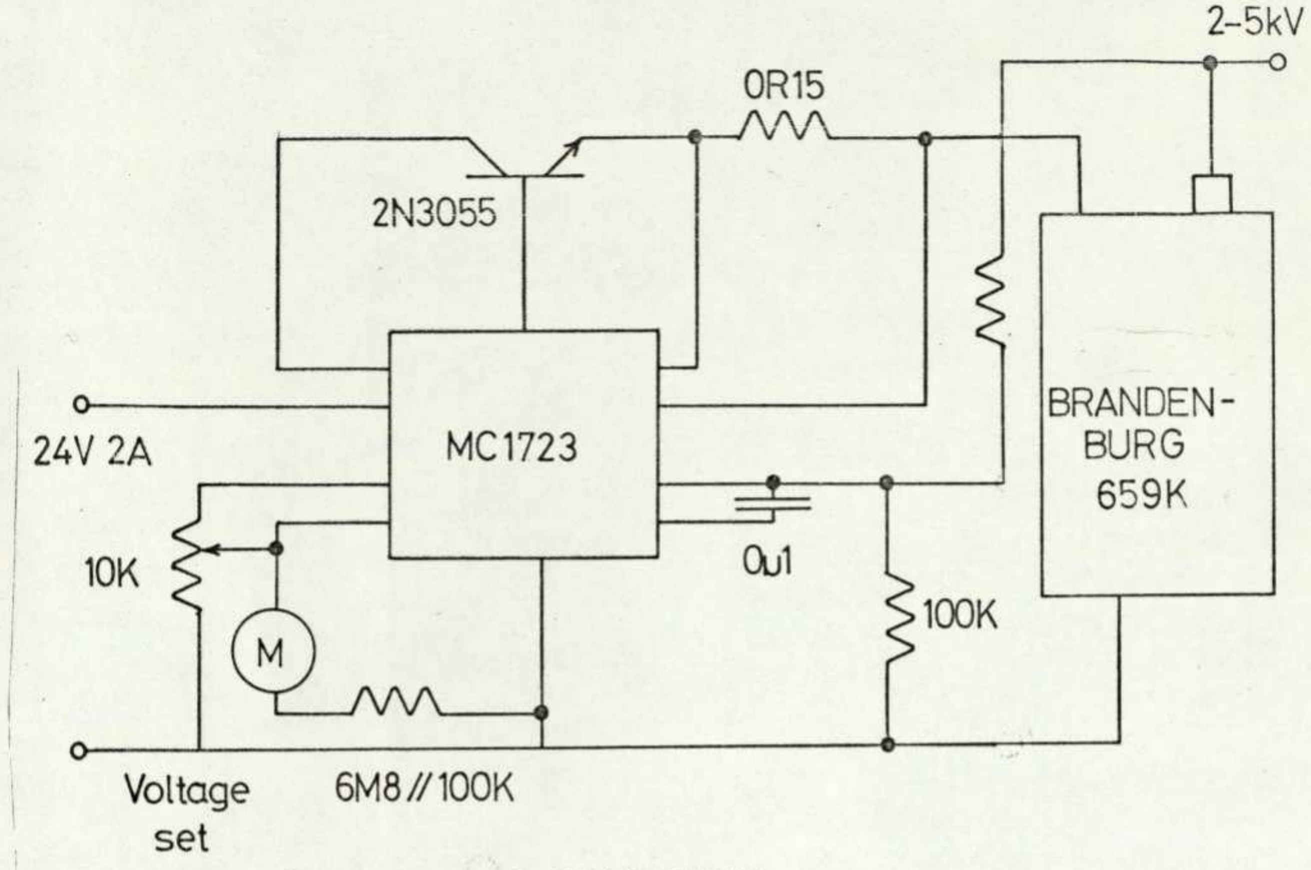

2-5kV SUPPLY

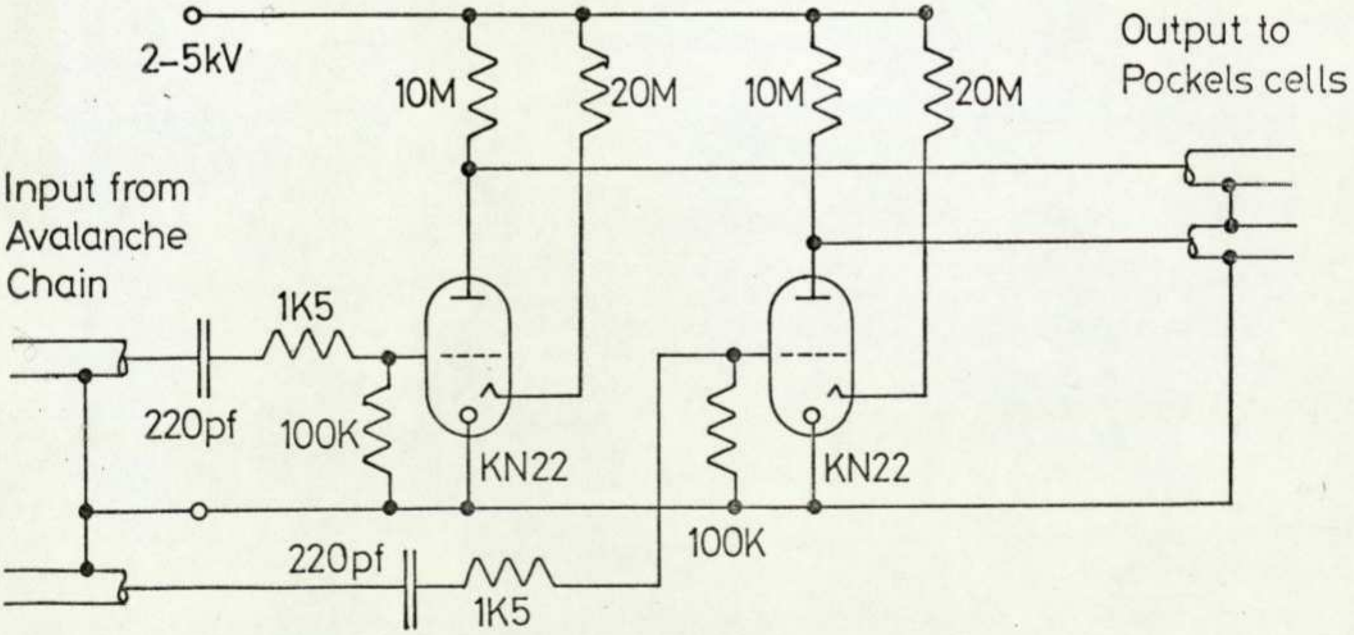

KRYTRON SWITCHES

Appendix 2d

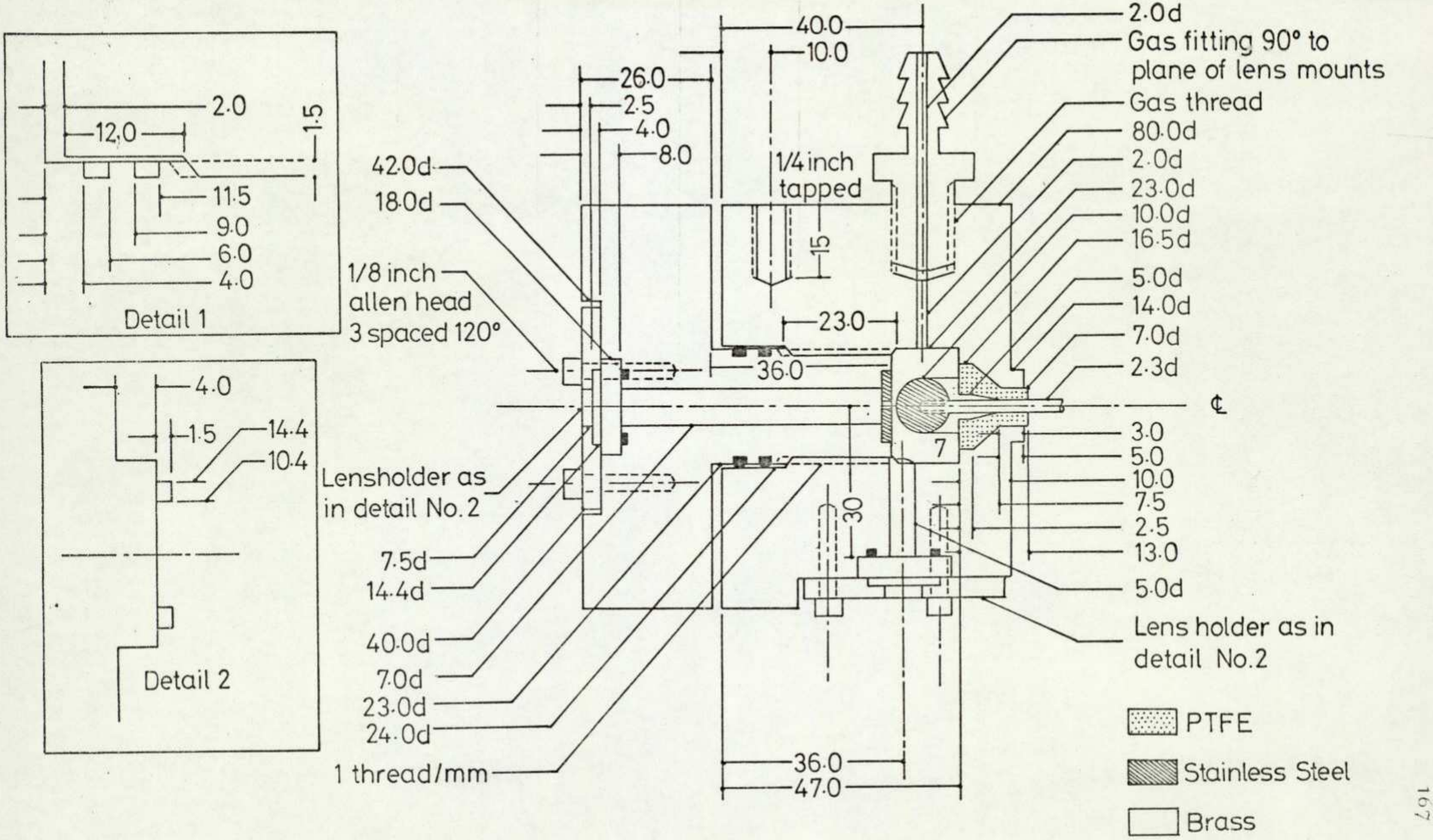

All measurements in mm

Appendix 3a. LTSG No1 SINGLE TERMINAL

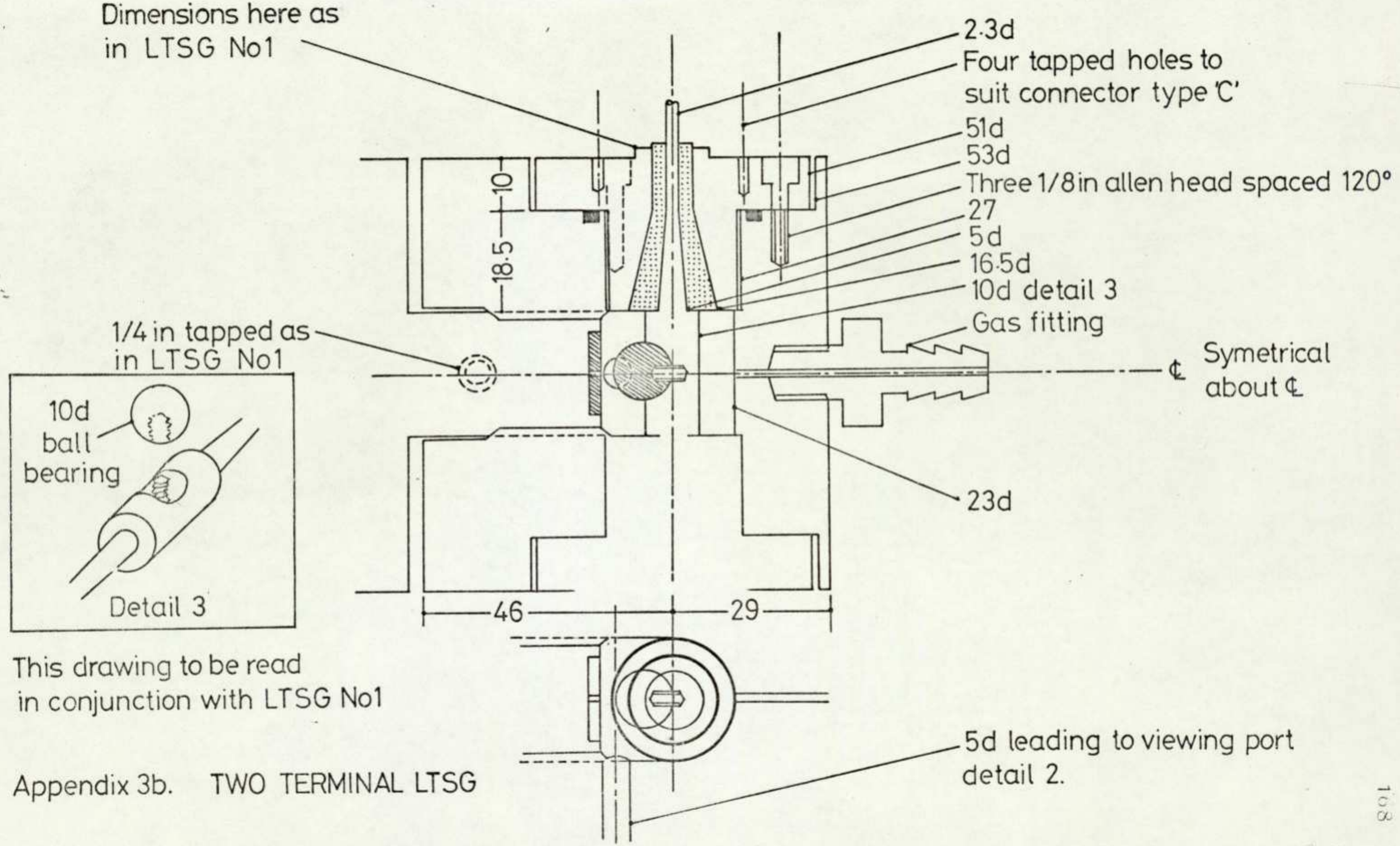

This drawing to be read in conjunction with LTSG No1

Appendix 3b. TWO TERMINAL LTSG

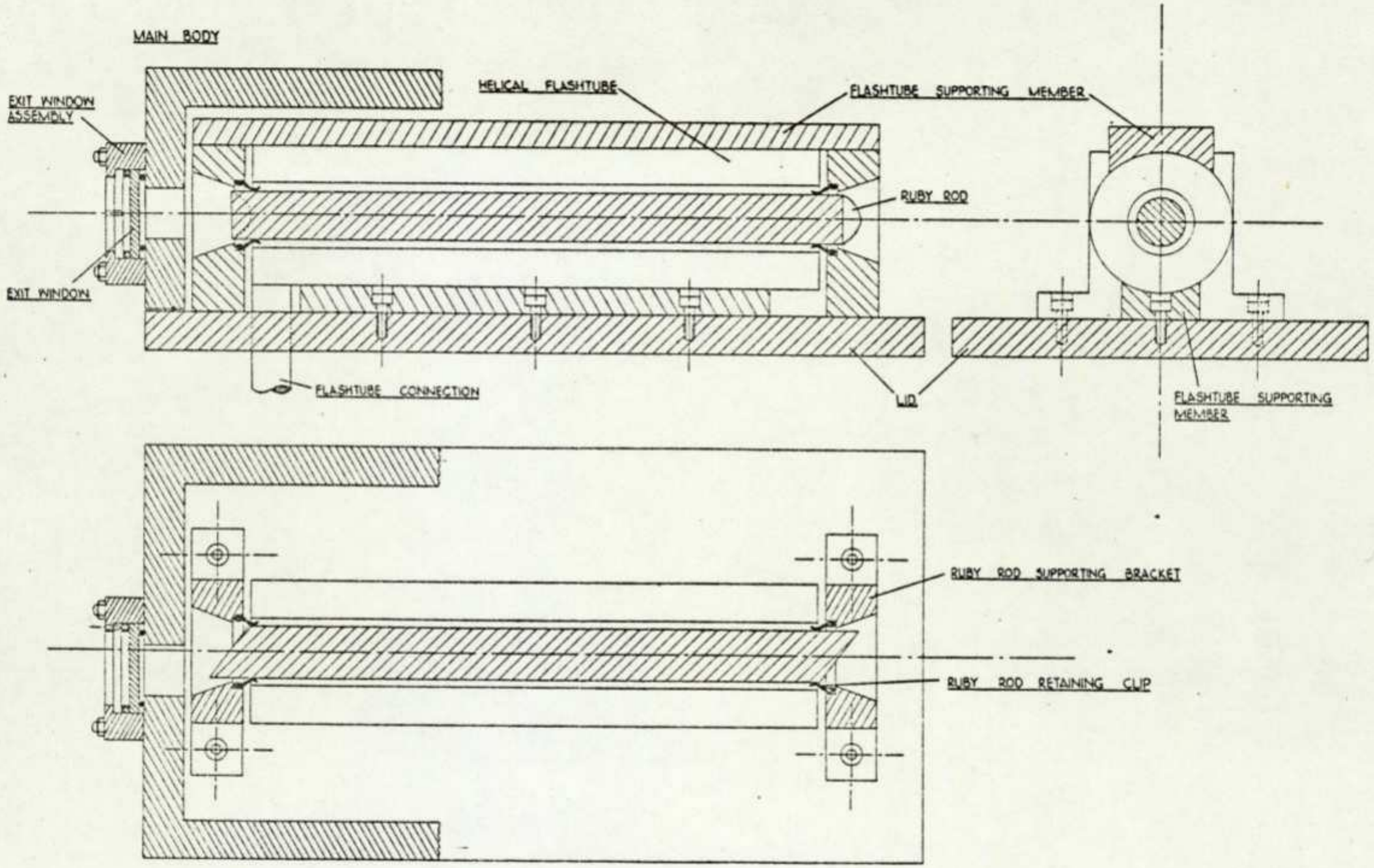

Appendix 3c Laser Amplifier

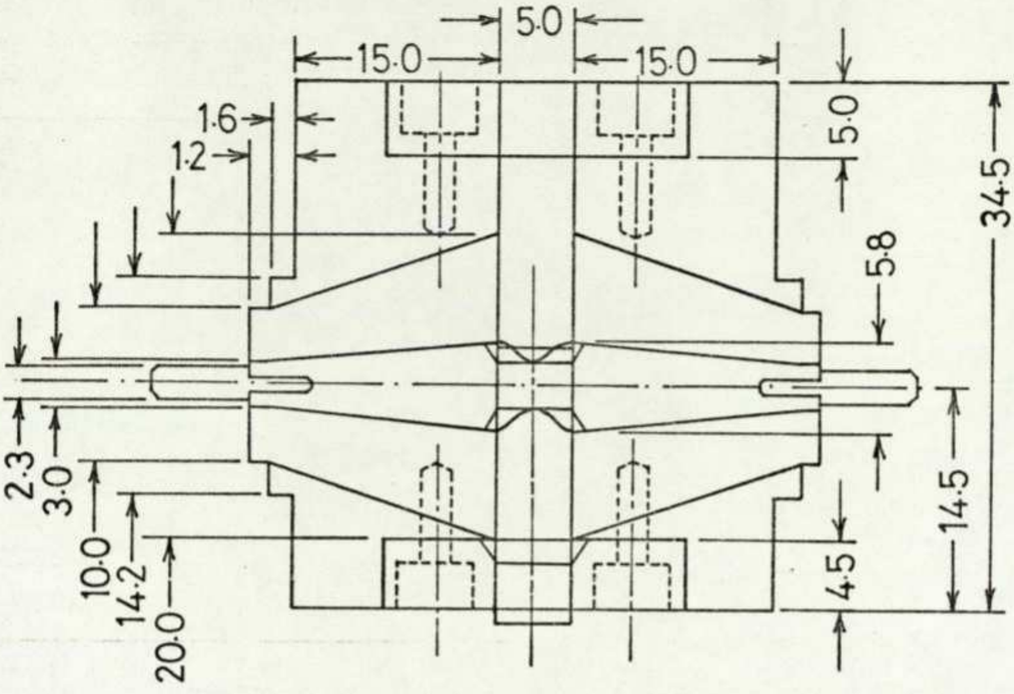

Section AA'

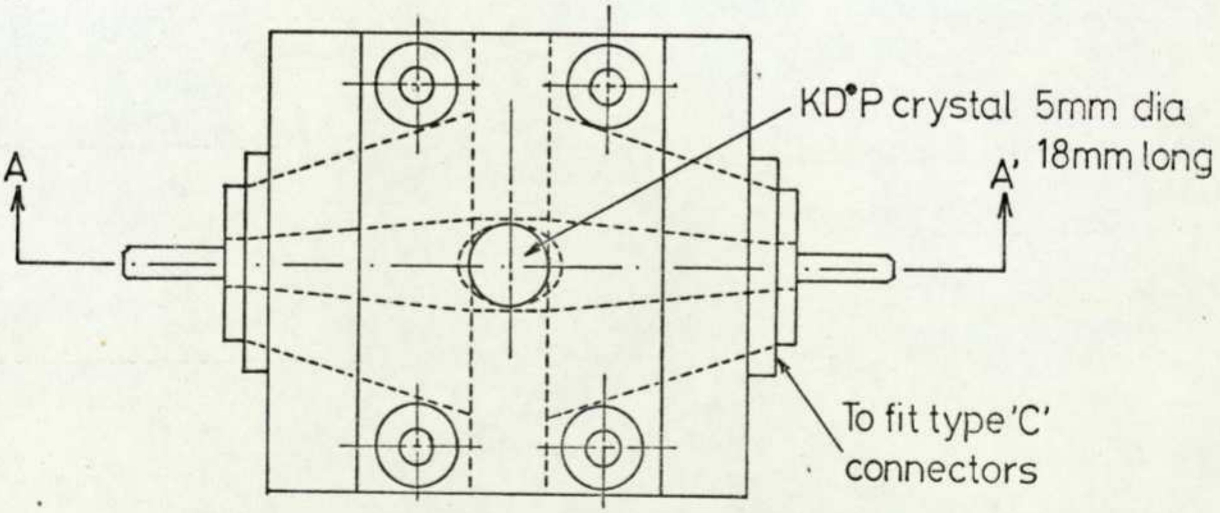

Plan

Appenix 3d. POCKELS CELL

Appendix 4.

Labels used in this program are as follows;

CVG :Volume heat capacity(host) D :Thermal diffusivity(host)
CVI :Volume heat capacity(inclusion) E :Emissivity(inclusion)
ENDES :Incident energy density T :Incident pulse length
EN :Incident power density(flux) R :Inclusion radius

```
      MASTER HEAT
C     PROGRAM TO CALCULATE TE TEMPERATURE OF A PARTICLE AFTER  BEING
C     ILLUMINATED WITH .6U RADIATION
C     FOR ADP WITH INCLUSIONS OF AL CU AND FE
      REAL NET,LIM
      ENDES=20.0
      CVG=0.315
      D=0.08
      E=0.3
      DO 9 I=1,3
      IF(I-1)10,0,10
      CVI=0.55
10    IF(I-2)11,0,11
      CVI=0.817
11    IF(I-3)12,0,12
      CVI=0.926
12    T=20.0E-9
      WRITE(2,13)CVI,E
13    FORMAT(1H1,12X,'TEMP FOR AN INCLUSION WITH HEAT CAPACITY OF ',E8.3
     1,' AND AN EMISITIVITY OF ',E8.3)
2     WRITE(2,4)T
4     FORMAT(///,12X,'THE TEMPERATURE OF THE PARTICLE FOR A PULSE LENGTH
     1 OF ',E8.3,' SECONDS'/,29X,'RADIUS CM',14X,'TEMP DEG')
      EN=ENDES/T
      R=10.0E-4
      EQ=3*CVG/CVI
      EM=(EQ*(4-EQ))**0.5
      Q=EQ**2+EM**2
1     A1=EQ*EM*D*T/(2*R**2)
      B=EQ*(D*T)**0.5/(R*2)
      LIM=EM*(D*T)**0.5/(R*2)
      SUM=0.0
      B2=EM/Q
      B3=((EQ**2-EM**2)/(4*R**2))*D*T
      B4=EXP(B3)/Q**0.5
      B5=((EQ/Q**0.5)*SIN(A1)-(EM/Q**0.5)*COS(A1))*S15ADF(B,0)
      B6=B2+B4*B5
      A2=(3*E*EN*R*0.22783)/(CVI*EM*D)
      C1=-(EM**2*D*T)/(4*R**2)
      C2=2*EXP(C1)/(3.1415*Q)**0.5
      ENC=LIM/10
      NET=ENC/2
8     D2=2*B*NET-A1
      X=NET**2
      IF(X-0.15E03)0,0,3
      D1=EXP(X)*(EQ/Q**0.5*COS(D2)-EM/Q**0.5*SIN(D2))
      D3=ABS(D1)
      S=D3*ENC
      SUM=SUM+S
      NET=NET+ENC
      IF(NET-LIM)8,0,0
      TEMP=A2*(B6-C2*SUM)
      WRITE(2,5)R,TEMP
5     FORMAT(29X,E8.3,10X,E8.3)
      IF(TEMP)3,3,0
      R=R/1.1
      IF(R-0.01E-4)0,1,1
3     T=T/(10.0**0.5)
      IF(T-0.2E-9)0,2,2
9     CONTINUE
      STOP
      END
```

Appendix 5 PUPLISHED WORK

Published papers removed for copyright reasons

Scott, J.C., Ley, J. and Palmer, A.W. (1976) 'A simple switching system for producing single and double variably spaced, variable length nanosecond light pulses', *Optical and Quantum Electronics*, 8, pp. 561–563.

Scott, J.C. and Palmer, A.W. (1978) 'Pressure dependence of the rise time of laser-triggered spark gaps', *J. Phys. E: Sci. Instrum.*, 11(5), p. 495-

Scott, J.C. and Palmer, A.W. (1978) 'The production of variable-length subnanosecond light pulses in a laser system', J. *Phys. E: Sci. Instrum.*, 11(9), p. 901-